Dissertations

Graduate College

12-2010

Dielectronic Recombination for Aluminum-Like Ions and Photoabsorption Cross Sections for Magnesium Ions at the K-Edge

Shahin Ahmed Abdel-Azim Abdel Naby
Western Michigan University

DIELECTRONIC RECOMBINATION FOR ALUMINUM-LIKE IONS AND
PHOTOABSORPTION CROSS SECTIONS FOR
MAGNESIUM IONS AT THE K-EDGE

by

Shahin Ahmed Abdel-Azim Abdel Naby

A Dissertation
Submitted to the
Faculty of The Graduate College
in partial fulfillment of the
requirements for the
Degree of Doctor of Philosophy
Department of Physics
Advisor: Thomas W. Gorczyca, Ph.D.

Western Michigan University
Kalamazoo, Michigan
December 2010

DIELECTRONIC RECOMBINATION FOR ALUMINUM-LIKE IONS AND
PHOTOABSORPTION CROSS SECTIONS FOR
MAGNESIUM IONS AT THE K-EDGE

Shahin Ahmed Abdel-Azim Abdel Naby, Ph.D.

Western Michigan University, 2010

Accurate and reliable recombination data are needed for modeling the ions in the finite-density plasmas that may take place in solar flares and in divertors of magnetically confined fusion devices such as the International Thermonuclear Experimental Reactor (ITER). Dielectronic recombination (DR) is the dominant recombination mechanism in photoionized and collisionally-ionized plasmas. DR rate coefficients for M-shell argon ions have been calculated using a configuration-average approach. DR rate coefficients for the aluminum-like isoelectronic sequence are instead calculated using the state-of-the-art multiconfiguration Breit-Pauli (MCBP) atomic structure and collision code AUTOSTRUCTURE. Good agreement is obtained with the measurements from the Heidelberg heavy-ion Test Storage Ring facility. The Maxwellian-averaged DR rate coefficients are fitted into a simple formula for efficient dissemination of data and ease of use in plasma modeling codes.

K-shell photoabsorption cross sections are required for determining the chemical abundances of the interstellar medium. As a secondary project, K-shell photoabsorption cross sections for magnesium ions have been calculated using the Belfast R-matrix computer package.

UMI Number: 3441006

UMI®

Dissertation Publishing

ProQuest®

ACKNOWLEDGMENTS

Acknowledgments-Continued

encouragement. I would like to acknowledge Prof. John Miller for accepting to serve on my committee, his valuable discussions, and reviewing my dissertation. I cannot ignore the support from the department of physics at WMU and from the chair, Prof. Paul Pancella, and the great help from Kerry Cochran, Lori Krum, Robert Scherzer, and Benjamin Gaudio. Special thanks go to my office mates Dr. Dragan Nikolić and Dr. Fatih Hasoglu for their fruitful discussions and interesting comments. I should thank my back home physics department for being patient during my study abroad, especially Prof. Fayez Shahin and Prof. Hany Hamdy. Their encouragement is totally appreciated. Finally, I would like to thank my whole family, parents, brothers, and sisters for their continuous support. No word can express my gratitude to my lovely wife, Nahla, and to my kids, Ahmed, Minnah, Mohamed, and the new baby Ali, for their patience, encouragements, and support. Without them I couldn't finish my degree.

<div align="right">Shahin Ahmed Abdel-Azim Abdel Naby</div>

TABLE OF CONTENTS

iv

Table of Contents – Continued

CHAPTER

Table of Contents – Continued

LIST OF TABLES

vii

List of Tables –Continued

CHAPTER I

INTRODUCTION

In astrophysical and laboratory plasmas, such as the International Thermonuclear Experimental Reactor (ITER), electrons, ions, and photons may interact with each other, transferring energy from one particle to another. These interactions result in many atomic processes such as excitation, ionization, de-excitation, and recombination. The photon-ion processes include resonant photoabsorption (PA) and photoionization (PI), with their inverse processes spontaneous decay and radiative recombination (RR), respectively. Let's assume that electrons are denoted by e^-, ions with initial charge q are denoted by A^{q+}, and photons are denoted by their energy $h\nu$ where $h = 6.626068 \times 10^{-34}$ J.s is Planck's constant and ν is the frequency of the photon in Hertz.

The resonant photoabsorption (PA) can be represented as

$$h\nu + A^{q+} \longrightarrow A^{(q+)*}, \tag{1.1}$$

where a photon with an energy $h\nu$ is absorbed by the ion A^{q+}. The ion is excited from a lower state into a higher excited state $A^{(q+)*}$ provided that the difference in energy between the initial and the excited states matches the incident photon energy. This process is the inverse of spontaneous decay.

Electron-ion interactions can be divided into direct and indirect processes. Direct processes include radiative recombination (RR), electron impact excitation (EIE), and electron impact ionization (EII), while the inverse of these direct processes are photoionization (PI),

electron impact de-excitation (EIDE), and the three-body recombination (TBR). Table 1.1 summarizes the direct processes accompanied by their inverse ones. Electrons with different energies are denoted by $e^{-\prime}$ or $e^{-\prime\prime}$.

Table 1.1   Direct electron-ion interaction processes and their inverse processes

Processes	Notation
Radiative Recombination (RR)	$e^- + A^{q+} \longrightarrow A^{(q-1)+} + h\nu$
Electron Impact Excitation (EIE)	$e^- + A^{q+} \longrightarrow A^{q+*} + e^{-\prime}$
Electron Impact Ionization (EII)	$e^- + A^{q+} \longrightarrow A^{(q+1)+} + e^{-\prime} + e^{-\prime\prime}$
Inverse processes	Notation
Photoionization (PI)	$h\nu + A^{(q-1)+} \longrightarrow A^{q+} + e^-$
Electron Impact De-excitation (EIDE)	$e^- + A^{q+*} \longrightarrow A^{q+} + e^{-\prime}$
Three Body Recombination (TBR)	$e^- + e^- + A^{(q+1)+} \longrightarrow A^{q+} + e^{-\prime}$

As a result of these collisions, electrons can be excited from the ground state, which has the lowest energy, to higher excited states (or to states with higher principal quantum number n, which we refer to as Rydberg states) leaving a hole (vacancy) behind. In the Al-like system, the ground state is $3s^2 3p [^2P]$, whereas the $3s3p^2 [^4D,\ ^2P,\ ^2D]$ states are examples of excited states. The neon core ($1s^2 2s^2 2p^6$) is omitted for simplicity. As a result of the EIE of the ground state of the Al-like ions, the $3s3p^2 n\ell$ state can be formed. This state is above the ionization limit of the Al-like ions, and we call it as Rydberg state. This state has two excited electrons, so we call it a doubly-excited state. Doubly-excited states are usually formed due to EIE, electron capture, photoexcitation, and electron-ion recombination. These doubly-excited states are unstable and there are two possible ways of stabilization, either by electron emission or by photon emission. The former is referred to as Auger emission (autoionization) and the latter is called radiative stabilization. In the case of Auger emission, the inner shell hole is filled with an outer shell electron and

2

the released energy causes another electron to be ejected. This increases the degree of ionization of the system by one. On the other hand, stabilization could happen by electron transitions from higher excited states to fill this vacancy with a photon being emitted. The rates for these two processes are denoted by A^a and A^r, respectively, and will be discussed in more detail in Sec. 2.5.

Electrons and ions may collide via an indirect (resonant) process called dielectronic recombination (DR), which plays an important role in plasma modeling and diagnostics of physical conditions. DR is a two step process in which a free electron, with kinetic energy E_k, collisionally excites the ion (with at least one electron) and is then captured into a Rydberg state, forming an intermediate doubly-excite state ($[A^{(q-1)+}]^{**}$). This doubly excited state is unstable and may autoionize or it can radiatively stabilize by emitting a photon. When stabilization happens via photon emission, the DR process is completed and it can be described as

$$e^- + A^q \rightleftharpoons [A^{(q-1)+}]^{**} \rightarrow A^{(q-1)+^*} + h\nu. \tag{1.2}$$
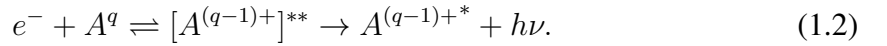
As a consequence of the DR process, the total energy of the recombined ion is reduced to below its ionization limit. Conservation of energy requires that $E_k = \Delta E - E_b$, where ΔE is the excitation energy of the initially bound electron and E_b is the binding energy.

In Fig. 1.1, the DR process for electron collision with S^{3+} is presented. Although many doubly-excited states can be formed during this collision, we present only the $3s3p^2[^2P]n\ell$ states for simplicity. These doubly-excited states can either autoionize or they can stabilize by emitting a photon which completes the DR process. Photon emission can be obtained via
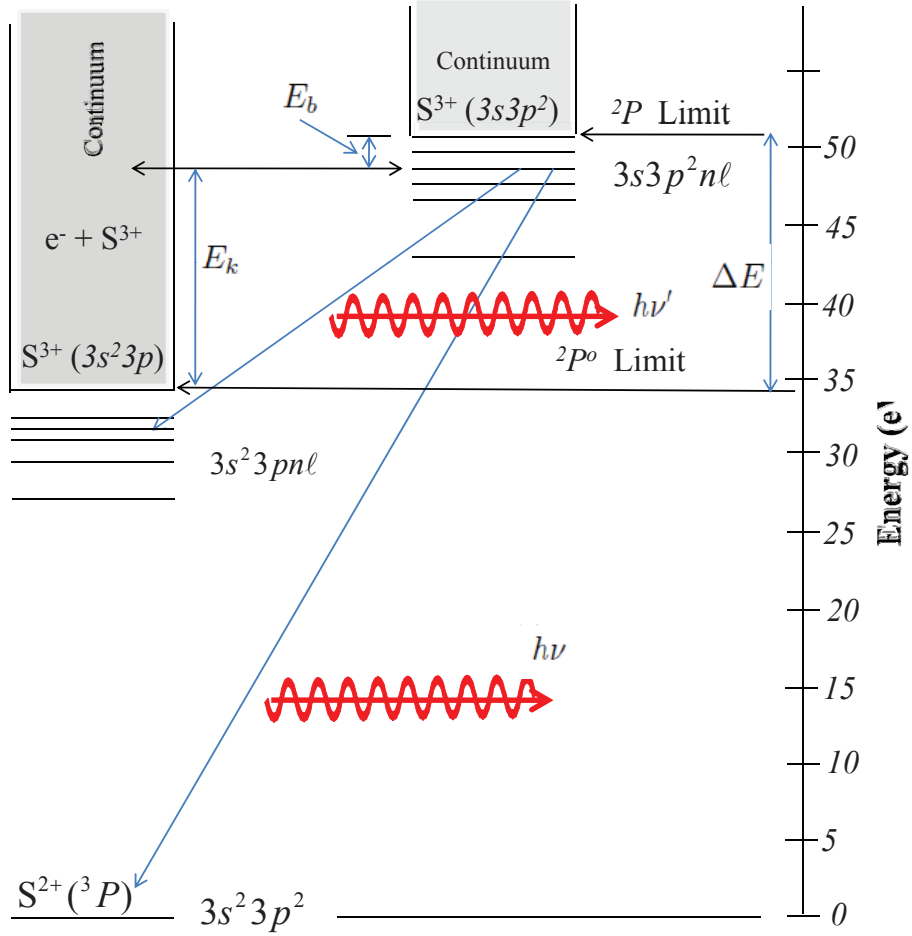
Figure 1.1 Schematic diagram of dielectronic recombination (DR) process. A free electron with kinetic energy E_k is captured by a target ion S^{3+} forming a doubly-excited state $[S^{2+}(3s3p^2 \, [^2P]n\ell)]^{**}$. The unstable doubly-excited state may decay either by autoionization or by emitting a photon. For the latter, the DR process is completed.

core decay ($3p \rightarrow 3s$), which gives $3s^2 3pn\ell$, or by the decay of the Rydberg electron ($n\ell$), which gives $3s^2 3p^2$ or $3s3p^2 n'\ell'$. A schematic representation for this decay is presented as

$$e^- + S^{3+}(3s^2 3p \, [^2P]) \rightleftharpoons [S^{2+}(3s3p^2 \, [^2P]n\ell)]^{**} \rightarrow S^{2+}(3s^2 3p^2) + h\nu$$

$$\rightarrow S^{2+}(3s^2 3pn\ell)^* + h\nu'$$

$$\rightarrow S^{2+}(3s3p^2 n'\ell')^* + h\nu''$$
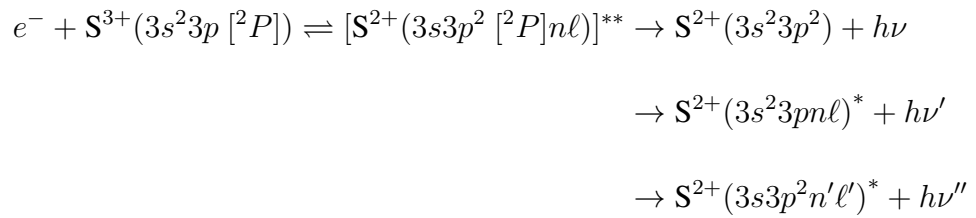
$$(1.3)$$

In the previous example, core excitations take place without changes in the principal quantum number (e.g., $3s \rightarrow 3p$), and this is what we call DR with $\Delta n_c = 0$ core excitation, where low-temperature DR occurs. On the other hand, high-temperature DR is obtained for $\Delta n_c \geq 1$. It is worth while to know that $\Delta E = E(3s3p^2\ [^2P]) - E(3s^23p\ [^2P])$ and $E_b = E(3s3p^2\ [^2P]) - E(3s3p^2\ [^2P]n\ell)$.

A history of the theoretical work on DR can be found in the review article by Seaton and Storey [1]. During the early study of the Earth's ionosphere, the disagreement between observations and theory based on RR alone led Sayers in 1939 (in a private communication to Seaton) to suggest that the inverse process of autoionization could be an additional mode of recombination and it might be important to the study of the ionosphere. This prompted Massey and Bates to introduce a new resonance mode of recombination and they called it dielectronic recombination (DR) [2]. However, these estimates of the rate coefficients of this process indicated that DR is not important for the ionosphere, where the temperatures are too low to excite the high energy Rydberg states.

In the study of ionization and recombination of the solar corona, the coronal temperatures deduced from collisional ionization equilibrium were significantly lower than the temperatures deduced from coronal gas density gradients and from the Doppler broadening of the spectral lines, implying that either the ionization rates were too large or the recombination rates were too low. In 1961, Unsöld sent a letter to Seaton suggesting that DR might account for this discrepancy in the solar corona. Seaton initially concluded that DR would not significantly increase the recombination in the solar corona. But this conclusion was incomplete because only the lower energy states were included, not the higher ones.

In 1964, Burgess showed that this discrepancy could be removed by including the higher Rydberg states [3], and since then the importance of the DR process has been recognized.

After the general formula of Burgess [3, 4], various formulas for calculating DR rate coefficients with many fitting parameters were introduced, mainly for H-like or He-like ions. In 1966, Tucker and Gould proposed a formula that depended on the energy difference between the states and some other fitting parameters [5]. However, their formula neglected the dependence of the Auger rates, A^a, on the angular momentum quantum number ℓ, so their work did not coincide with others. In 1968, Beĭgman *et al.* [6] introduced another formula by dividing the doubly-excited states into two groups for which either the radiative or the Auger rates (A^r, A^a) may be neglected. In 1970, the general formula was reproduced by Ansari *et al.* [7] in a simpler form depending on two parameters only and valid for low-lying states only. However, it soon became apparent that more sophisticated calculations for DR were required.

In 1969, Shore pointed out the importance of using accurate term energies rather than configuration-average energies in the calculations of DR rate coefficients [8]. However, he did not include the effect of channel coupling and exchange effects that may reduce the autoionization rates. In 1976, Burgess and Tworkowski [9] studied the effect of resonance overlap, exchange, and channel coupling, and obtained agreement to within 30% of the general formula for He-ions. In 1978, Gau and Hahn studied the dependence of the Auger and radiative transition probabilities of the high Rydberg states on their principal and orbital quantum numbers [10]. Also, Retter *et al.* showed that the dependence of Auger and radiative transition probabilities on the nuclear charge, Z, breaks down at high Z and a

polynomial expression in Z works better [11]. In 1980, Hahn calculated the DR rate co-efficients for the Be and Ne sequences, which led him to introduce a formula for the DR rate coefficient as a function of the number of electrons in the target ion and the nuclear charge [12]. In 1981, LaGattuta and Hahn studied the contributions from the high Rydberg states to the DR process [13]. Moreover, they pointed out the importance of cascades to all excited levels of Mo^{31+} [14]. In 1983, McLaughlin and Hahn estimated the DR cross section for O^{5+} and studied the dependence of the DR cross section on the effective charge [15]. In 1986, LaGattuta *et al.* discussed the effect of the electric field on the high Rydberg states in the DR for Mg^+ and Ca^+ target ions [16]. In 1987, Omar and Hahn calculated the DR cross sections for Ca^{10+}, Ca^{11+}, and Ca^{12+} ions with K-shell excitations [17], while DR cross sections for Mo^{30+}, Mo^{31+}, and Mo^{32+} with L-shell excitations were calculated by Hahn *et al.* [18]. In 1988, Moussa *et al.* calculated DR cross sections and rate coefficients for the Ne-like Mg^{2+}, P^{5+}, and Cl^{7+} ions with L-shell excitations [19]. In 1989, Ramadan and Hahan calculated the DR cross sections and rate coefficients for ions in the B-like isoelectronic sequence for the $2s \rightarrow 2p$ excitations [20]. DR cross sections and rate coefficients for the metastable states of O^{6+} and C^{4+} ions were studied by Hahn and Bellantone [21]. Also, the influence of metastable states and thermal equilibrium upon DR in low-density to moderate-density plasmas was studied by Roszman [22]. In 1993, Hahn introduced an improved rate formulas for DR by fitting all the existing DR data for ions with core charge $Z_C < 50$ and with number of electrons in the target $N < 13$ [23]. The review article by Dubau and Volonté discussed the importance of DR processes and its application in astronomy [24]. In 1997, the review article by Hahn summarized the improved

understanding of the basic physics involved in various recombination processes [25]. In 1995, Dasgupta calculated the DR rate coefficients for all fine structure levels of the $n = 3$ excited levels of Fe^{15+}- Fe^{18+} ions [26].

A state-of-the-art multiconfiguration Dirac-Fock (MCDF) method was used by Chen to calculate the DR rate coefficients for the He isoelectronic sequence with $6 \leq Z \leq 42$ for temperatures in the range $0.1 \leq T \leq 12$ keV [27]. He showed that the relativistic effects changed the allowed Auger and radiative rates by a factor of 3 and increased the transition energies for Mo^{40+} and this led to a reduction in the DR rate coefficient. In the case of *LS*-coupling calculations, the DR rate coefficient is dominated by only a few autoionizing states, while in the relativistic treatment the DR rate coefficient is redistributed among many states. Relativistic calculations of DR rate coefficients for the Ne isoelectronic sequence were carried out by Chen [28], while his DR calculations for F-like ions were limited to Se^{25+} [29]. The study by Chen of the effects of relativity and configuration interaction (CI) on DR rate coefficients of hydrogen-like ions showed that DR rate coefficients calculated in IC-coupling with CI may be sufficient for light ions. However, relativistic calculations in IC-coupling with CI are necessary for medium-heavy and heavy ions [30]. Total DR rate coefficients for the $^2P_{1/2}$ and $^2P_{3/2}$ states in B-like Ti^{17+}, Fe^{21+}, and Mo^{37+} ions were calculated by Chen *et al.* for the electron temperatures $0.1 \leq T \leq 10^4$ eV using the MCDF method in IC-coupling [31].

The importance of IC-coupling in the study of DR rate coefficients was discussed by Badnell in his calculations for the DR rate coefficients of Fe^{21+} and Fe^{22+} [32] using the state-of-the-art multi-configuration Breit-Pauli (MCBP) method. He used the same proce-

dure for calculating the DR rate coefficients for Be-like ions ranging from C^{2+} to Mo^{38+} [33]. In 1988, Badnell studied the influence of core fine structure interactions on DR at low temperatures for the B-like C, N, and O recombined ions, where he found stronger interactions were obtained for higher ionic charges [34]. DR rate coefficient calculations for the ground and metastable levels of carbon and oxygen ions in IC-coupling were studied by Badnell [35]. Badnell and Pindzola calculated $\Delta n_c = 0$ DR cross sections and rate coefficients for the B-like C^+, N^{2+}, O^{3+}, and F^{4+} ions in both *LS-* and IC-coupling approximations [36]. Also, they calculated the $\Delta n_c = 0$ DR cross sections and rate coefficients for O^{q+} ($q = 1 - 5$), in both *LS-* and IC-coupling approximations [37]. Moreover, they calculated DR cross sections and rate coefficients for the Ne-like P^{5+} and Cl^{7+} ions in configuration-average (CA), *LS-* and IC-coupling approximations [38].

DR cross sections for H-like ions were calculated by Pindzola *et al.* [39], where they studied the effect of fine structure and IC-coupling on the DR cross section of O^{7+}. Agreement with the Test Storage Ring (TSR) measurements in Heidelberg by Kilgus *et al.* [40] to better than 20% was obtained. The effect of the CI between resonances for DR and resonant transfer excitation (RTE) of Na-like ions were studied by Gorczyca and Badnell [41], where good agreement was obtained with the experimental measurements by Linkemann *et al.* [42].

Another-state-of-the-art method used for calculating the recombination rate is usually referred to as the unified method. In 1994, Nahar and Pradhan developed a method that combined both RR and DR into a unified rate coefficient for the electron-ion recombination [43]. It was used to calculate the electron-ion recombination rate coefficients for

silicon and sulfur ions by Nahar [44], but the effect of radiation damping was not considered. Thus the resonance widths included only the autoionization width Γ^a and missed the radiative width Γ^r, which is important for higher q (the residual charge). In 1995, Robicheaux et al. [45] included the effect of the radiation damping to their close-coupling approximation (radiation damped-R-matrix). DR cross section calculations for Ar^{15+} using radiation damped-R-matrix were carried out and compared to perturbative calculations [32] for the same ion by Gorczyca et al. [46]. Good agreement between the two results were obtained, which suggested that radiation-damped R-matrix can be used to investigate systems where interference between RR and DR is expected. The study of the photorecombination of Fe^{17+} by Gorczyca et al. [47] revealed the shortcomings of the R-matrix method for calculating DR cross sections. This method did not account accurately for the case of radiative decay followed by autoionization.

Many experimental techniques were used to study the DR process such as the Test Storage Ring (TSR) at Heidelberg University, the experimental Storage Ring (ESR) at GSI, the EN tandem accelerator in Aarhus, the electron-beam ion trap (EBIT) at Lawrence Livermore National Laboratory, the electron-beam ion source (EBIS) at Kansas State University, the Bevalac at Lawrence Berkeley Laboratory, and the CRYRING facility at Stockholm, Sweden. The TSR facility measures the resonance strengths and energies with higher accuracy and has the advantage of the negligible metastable content and low background. In 1978, Breton et al. [48] presented a new method for estimating DR rate coefficients for highly ionized ions of molybdenum from the effect of saw-tooth electron temperature relaxations in tokamak plasmas on the emission of impurity ions. In 1982, Isler et al. [49]

measured the concentrations of Fe^{14+}, Fe^{15+}, Fe^{17+}, and Fe^{18+} ions to determine the ratios of recombination and ionization rate coefficients. DR measurements using EBIS were performed by Briand *et al.* for Ar^{12+}-Ar^{15+}ions [50] and by Ali *et al.* for Ar^{16+} [51]. On the other hand, DR measurements using EBIT were studied by Knapp *et al.* [52] for Ni^{26+} and by Beiersdorfer *et al.* [53] for Fe^{24+}. Tanis *et al.* introduced a new process for the ion-atom collisions which is similar to DR in the electron-ion collisions and they called it resonant capture with excitation [54]. They measured the K-shell X-ray emission following the electron capture for the collision S^{q+} + Ar with $q = 13 - 16$. DR cross sections for C^+ were measured by Mitchell *et al.* [55] using a merged electron-ion beam apparatus. The first measurements of DR rate coefficients associated with the $2s \rightarrow 2p$ excitation in the B-like N^{2+}, O^{3+}, and F^{4+} ions were reported by Dittner *et al.* [56].

In 1995, DeWitt *et al.* [57] spectroscopically determined DR resonances for He^+ using a cooled ion beam in the CRYRING Storage Ring. In 1997, Savin *et al.* [58] measured DR rate coefficients for Fe^{17+} and showed the importance of the fine structure core excitations. Uwira *et al.* [59] studied the recombination of Au^{49+}-Au^{51+} ions at the TSR facility. Accurate measurements of $\Delta n_c = 0$ DR resonances with Ar^{15+} were performed at the CRYRING by Zong *et al.* [60]. In 1998, strong relativistic effects and natural line widths were observed in the DR spectrum of C^{3+} by Mannervik *et al.* [61]. In 1999, Savin *et al.* [62] measured the resonance strengthes and energies for $\Delta n_c = 0$ DR of Fe^{17+} and Fe^{18+}. DR measurements for F^{6+} were carried out by Glans *et al.* [63]. In 2001, the DR spectrum of N^{4+} was measured with high resolution and accuracy by Glans *et al.* [64]. The effect of crossed electric and magnetic fields on the DR of Ne^{7+} and O^{5+} was measured at the

CRYRING by Bohm *et al.* [65, 66]. In 2002, Savin *et al.* measured resonance strengths and energies of Fe^{18+} and Fe^{19+} [67, 68]. In 2003, DR rate coefficient measurements in addition to investigations of the effect of external electric fields on the DR of O^{5+} were carried out at the CRYRING by Bohm *et al.* [69]. DR resonance strengths and energies were measured by Savin *et al.* of Fe^{20+} and Fe^{21+} [70]. Absolute RR and DR rate coefficients for Ni^{17+} were measured at the CRYRING by Fogle *et al.* [71]. Experimental measurements for the electron-ion spectrum of Na^{8+} were carried out by Nikolić *et al.* [72]. A summary of the the measurements of the DR spectra in the CRYRING facility of Li-like, Na-like, and Cu-like ions were presented by Glans *et al.* [73]. Absolute total recombination rate coefficients for C^{2+}, N^{3+}, and O^{4+} were measured by Fogle *et al.* [74, 75]. DR rate coefficients for Fe^{13+}, Fe^{7+}, and Fe^{8+} were measured by Schmidt *et al.* [76, 77, 78]. Electron-ion recombination of Si^{3+} was measured at the TSR facility by Schmidt *et al.* [79]. Electron-ion recombination measurements for Fe^{9+} and Fe^{10+} using a merged beams apparatus at the TSR were carried out by Lestinsky *et al.* [80]. Recent review articles for DR processes include those by Hahn [81], Pindzola *et al.* [82], and Kallman and Palmeri [83].

Earlier DR calculations have been sufficiently summarized by Aldrovandi and Péquignot [84], Mewe *et al.* [85], Shull and Steenberg [86], and Arnaud and Raymond [87], along with extrapolations and interpolations by Landini and Fossi [88, 89], but these previous studies were performed using the single-configuration *LS*-coupling approximation or semi-empirical formulas or isoelectronic interpolations. Badnell and co-workers [90] recently began a program to compute accurate DR rate coefficients from both ground and metastable

initial states (hereafter referred to as the DR project). Following the initiation of this project, computations of DR cross sections and rate coefficients were completed for the hydrogen-like isoelectronic sequence by Badnell *et al.* [91], helium-like isoelectronic sequence by Bautista *et al.* [92], lithium-like isoelectronic sequence by Colgan *et al.* [93], beryllium-like isoelectronic sequence by Colgan *et al.* [94], boron-like isoelectronic sequence by Altun *et al.* [95], carbon-like isoelectronic sequence by Zatsarinny *et al.* [96], nitrogen-like isoelectronic sequence by Mitnik *et al.* [97], oxygen-like isoelectronic sequence by Zatsarinny *et al.* [98], fluorine-like isoelectronic sequence by Zatsarinny *et al.* [99], neon-like isoelectronic sequence by Zatsarinny *et al.* [100], sodium-like isoelectronic sequence by Altun *et al.* [101], magnesium-like isoelectronic sequence by Altun *et al.* [102], and argon-like isoelectronic sequence by Nikolić *et al.* [103]. Extended work for the more complicated, third row isoelectronic sequences has begun [104]. These data, along with the RR data [105], have been used to provide new ionization balance determinations for photoionized (lower electron temperatures) and collisionally-ionized (higher electron temperatures) plasmas of astrophysical and/or fusion-related interests. DR rate coefficients for all the previous isoelectronic sequences are benchmarked against CRYRING and TSR experiments [67, 68, 70, 106, 107, 108] with recent summarized DR measurements for iron ions [109]. DR rate coefficients for all isoelectronic sequences from H-like up to Mg-like can be accessed from the webpage of the University of Strathclyde Atomic Data and Analysis Structure (ADAS) database (http://amdpp.phys.strath.ac.uk/tamoc/DATA) or from the webpage for the Oak Ridge Controlled Fusion Atomic Data Center Data (http://www-cfadc.phy.ornl.gov).

13

Another theoretical state-of-the-art method is the one based on the flexible atomic code (FAC) [110]. This method was used to calculate DR rate coefficients for the H-like through Ne-like isoelectronic sequences of Mg, Si, S, Ar, Ca, Fe and Ni, which showed good agreements with the results of the DR projects.

Another method is the relativistic many-body perturbation theory (RMBPT), which gives reliable low-energy DR data, but can only be used for one electron outside a closed shell. e.g. Na-like silicon by Orban *et al.* [111].

In the reminder of this Chapter, three projects are introduced: 1) M-shell DR rate coefficient for argon ions; 2) DR rate coefficients for Al-like ions; 3) K-shell photoabsorption for magnesium ions.

1.1   M-Shell Dielectronic Recombination for Argon Ions

Inside the magnetically confined fusion devices, such as ITER, the temperature may reach 1.5×10^8 K such that fusion can take place. The key design issue in ITER is to avoid the plasma disruption and besides other cooling methods, the divertor is designed to extract heat and impurities from the plasma. Argon has been used in the diagnostics of the plasmas [112, 113] as well as for mitigating the plasmas disruption [114]. In response to these applications, calculations for the ionization balance of argon are needed and this require previous knowledge of both ionization and recombination rate coefficients for argon isonuclear sequence. Since DR rate coefficients for Ar^{6+}- Ar^{17+} are available from the DR project and there no state-of-the-art DR rate coefficient calculations for the rest of the argon isonuclear sequence. Calculations for M-shell DR cross sections and rate coefficients are

cumbersome and some approximations have to be done to make these calculations possible.

New DR calculations for Al-like argon up to Cl-like argon (Ar^{5+} - Ar^+) are presented in

Chapter III.

1.2 Dielectronic Recombination for Aluminum-Like Ions

Cosmic plasmas are divided into collisionally ionized and photoionized plasmas. The

former are found, for example, in the Sun and Stars, and the latter are found in plane-

tary nebulae and active galactic nuclei (AGN). In collisionally ionized plasmas, ionization

occurs due to electrons. Hence, in the case of ionization equilibrium, ions are formed

at temperatures of nearly half of their ionization potential and higher temperature DR is

the dominant electron-ion recombination process [115]. On the other hand, ionization is

caused by the radiation field in the photoionized plasmas, and ions are formed at lower tem-

perature [116, 117]. DR is the dominant electron-ion recombination process for most of

the ions in the low density photoionized and electron-ionized plasmas [87, 118, 119]. The

codes devoted to modeling pohtoionized plasmas include CLOUDY by Ferland *et al.* [116]

and XSTAR by Kallman and Bautista [117], whereas, CHIANTI by Landi *et al.* [120] is

used to model X-ray emission for collisionally ionized plasmas. All these codes depend on

the accuracy of the DR rate coefficients to calculate ionization balance, thermal structure,

and line emissions of cosmic plasmas. Recent calculations for the collisional ionization

equilibrium ionic fractions for iron ions by Dere *et al.* [121] based on the DR rate coeffi-

cients performed by Badnell [122] are found to be different than the calculations done by

Mazzotta *et al.* [123] and this strongly shows the need for accurate DR rate coefficients

15

using state-of-the-art MCBP results.

Some of the Al-like ions are abundant in the solar spectra. For example, Ca^{7+} lines were observed with high-resolution by the Solar and Heliospheric Observatory (SOHO) [124]. Si^+, Ar^{5+}, and Ca^{7+} were observed by the solar ultraviolet measurements of the emitted radiation spectrograph on SOHO [125, 126], and still other lines are unidentified. So it is obvious that M-shell DR rate coefficients are needed, and calculations for Al-like DR rate coefficients are the next step for the DR project.

Although there are some pre-existing DR rate coefficient calculations for the Al-like isoelectronic sequence (e.g., S^{3+}), they were performed within a nonrelativistic *LS*-coupling approximation and only for the high temperatures characteristic of electron-ionized gas [84, 127, 128, 129, 130]. No data exist for the low temperatures characteristic of photoion-ized gas. In Chapter IV, new DR rate coefficient calculations for the Al-like isoelectronic sequence will be presented for all ions starting from Si^+ up to Zn^{17+}.

Astrophysicists and plasma modelers use the recommended data of Mazzotta *et al.* [123] in their models. These fitting coefficients are sometimes based on extrapolations across or interpolations through isoelectronic sequences. For the Al-like isoelectronic se-quence, it is not clear from which source(s) Mazzotta *et al.* acquired their recommended data. So, through this work, these sources will be determined.

1.3   K-Shell Photoabsorption Cross Sections for Magnesium Ions

Accurate data for the inner shell processes are required for modeling astrophysical plas-mas, especially after the advances in the spectral resolutions of the launched X-ray tele-

scopes such as *Chandra* X-ray observatory (http://chandra.harvard.edu), XMM-Newton (http://xmm.vilspa.esa.es), and the future International X-ray observatory (IXO). Moreover, K-shell photoabsorption cross sections are important for interpreting the observed spectra from distant cosmic emitters and determining the elemental abundances of our Galaxy's interstellar medium (ISM).

The observed flux density, $I(\lambda)$, is related to the photoabsorption cross section $\sigma^{PA}(E)$ and the emission flux density $I_o(\lambda)$ by

$$I(\lambda) = I_o(\lambda) \exp\left[-\sigma^{\mathrm{PA}}(E)N\right], \qquad (1.4)$$

where $E = hc/\lambda$ is the photon energy, c is the speed of light in the vacuum, λ is the wavelength, and N is the number of absorbers per unit area along the line of sight, known as the column density.

In 1979, Reilman and Manson [131] studied photoabsorption of all ionization stages of all astrophysically important elements within the independent-particle (IP) model. But, their results lack the important resonance absorption features that are so helpful in identifying elemental abundances (see Fig. 1.2). Previous K-shell photoabsorption cross sections for neon [132, 133] and oxygen [134, 135] ions were computed at Western Michigan University (WMU) and compared to high-resolution X-ray spectroscopy of ISM gas clouds [132, 136] to determine the abundances of oxygen and neon ions. Later, I was involved in a similar calculations for carbon ions [137].

K-shell photoabsorption calculations for magnesium ions are performed using the-state-of-the-art R-matrix method (see Sec. 2.7). This technique has proved to be successful
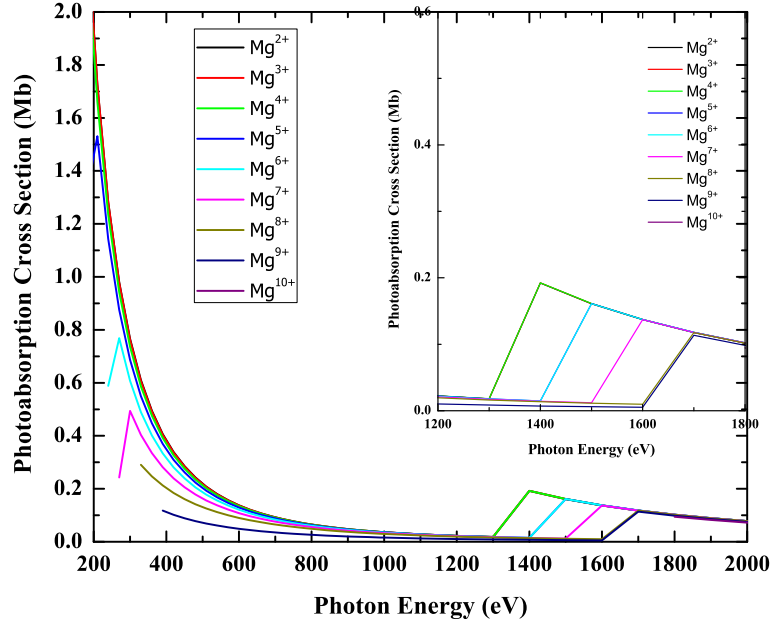
Figure 1.2 Photoabsorption cross section results for the magnesium isonuclear series showing that the IP model does not include the important K-shell resonances. In the X-ray energy region of interest, we see relatively featureless, step function behavior for these reported cross sections (1 Mb = 10^{-18} cm^2).

in describing both experimental synchrotron measurements [133, 138, 139] and *Chandra* high-resolution spectroscopic observations [132, 134, 136]. Comparisons with the results of Witthoeft *et al.* [140] obtained by using the Breit Pauli R-matrix method (BPRM) will be presented in Chapter V.

The rest of the dissertation is organized as follows. In Chapter II, the theoretical methodologies are presented. Chapter III discusses the M-shell DR rate coefficients results for Argon ions using a configuration-average approximation. In Chapter IV, the study of DR rate coefficients for the Al-like isoelectronic sequence is presented. Chapter V contains the results of K-shell photoabsorption for Mg-ions and I conclude with a summary in Chapter VI.

18

CHAPTER II

THEORETICAL METHODOLOGY

This Chapter deals with the theoretical methodology we have used in the calculations of DR cross sections and rate coefficients for the Al-like isoelectronic sequence and K-shell photoabsorption cross sections for Mg isonuclear sequence. Two approaches have been used through out this work. The first one is a pertubative technique, which we use for calculating DR cross sections using the-state-of-the-art multiconfiguration Breit-Pauli (MCBP) method. Particularly, the AUTOSTRUCTURE atomic structure package and collision code [32] (which incorporates the SUPERSTRUCTURE program [141]) is used for calculating energy levels and radiative and autoionization rates required in the DR cross sections and rate coefficients calculations. The second one is the-state-of-the-art R-matrix suit of codes, which is based on a close-coupling expansion [142, 143, 144]. This approach is used for the calculations of K-shell photoabsorption of Mg isonuclear ions. The R-matrix method is more accurate for describing the multichannel atomic problems [145, 146]. In particular, we have used the R-matrix codes [147] with some recent developments to take into account the elimination of the unphysical pseudoresonances [148] and spectator Auger decay broadening [138].

The rest of this Chapter is organized as follows. In Sec. 2.1, we describe the eigenvalue problem of an N-electron system in a non-relativistic framework followed by approximate wave functions for the N-electron system in Sec. 2.2. The relativistic corrections are discussed in Sec. 2.3, while the pertubative MCBP approximation is discussed in Sec. 2.4. In

Sec. 2.5, we present the radiative and Auger transition rates followed by a discussion of the DR cross section and rate coefficients in Sec. 2.6, and we conclude by introducing the R-matrix theory in Sec. 2.7.

2.1 Atoms With More Than One Electron

2.1.1 The Non-Relativistic Description

Armed with the study of the one-electron system [149, 150], we can proceed to deal with the N-electron systems ($N > 1$, and not necessarily equal to the atomic number Z). The time-independent Schrödinger equation for this system can be written as [151]

$$\mathcal{H}\,\psi(q_1, q_2, \cdots, q_N) = E\,\psi(q_1, q_2, \cdots, q_N), \tag{2.1}$$

where $\mathcal{H}$ is the Hamiltonian operator, ψ is the wave function, E is the total energy of the system, and q_i represents the spacial and spin coordinates of electron i. Our wave function, ψ, is continuous and represents the solution of the above eigenvalue problem in Eq. (2.1). For simplicity in notation and for convenience in numerical work, we shall now adopt *atomic units* (a.u.), i.e., we shall choose the basic units such that $\hbar$, m_e, e, and $4\pi\epsilon_o$ all become equal to one except where explicitly specified (see Appendix A).

In the absence of external fields, if we treat the nucleus as a point charge of infinite mass, and neglect relativistic effects (they will be included later), then we can write the non-relativistic Hamiltonian for an N-electron system, in a.u., as

$$\mathcal{H}_{nr} = \sum_{i=1}^{N} \left(-\frac{1}{2}\nabla_i^2 - \frac{Z}{r_i} \right) + \sum_{i<j}^{N} \frac{1}{r_{ij}}. \tag{2.2}$$

Here, the first two terms in the Hamiltonian are the sum of the kinetic and potential energies for the one-electron system, Z is the nuclear charge of the N-electron system, r_i is the

20

distance of electron i from the nucleus, the third term represents the Coulomb repulsion between electrons i and j, and r_{ij} is the relative distance between these two electrons. We avoided the double counting of the electron pairs by imposing the restriction $i < j$ on the second summation. This Hamiltonian is independent of the spin of the electrons and is invariant under an interchange of the coordinates of any two electrons [149]. Let us deal with the situation where the wave function has only spacial coordinates. As we may realize, the Shrödinger equation is not separable because of the term $\sum_{i<j}^{N} 1/r_{ij}$. Moreover, this term is too large to be treated by perturbation theory. Hartree and Slater introduced the *central field* approximation to deal with this problem which is based on the independent particle model. In this case, each electron moves independently in an effective potential due to the nucleus and the other $(N-1)$-electrons.

If we add and subtract $\sum_{i=1}^{N} V(r_i)$ to Eq. (2.2), then $\mathcal{H}_{nr}$ can be written as an unperturbed ($\mathcal{H}_c$) and a perturbed parts ($\mathcal{H}_1$) as follows [152]

$$\mathcal{H}_{nr} = \mathcal{H}_c + \mathcal{H}_1. \tag{2.3}$$

The unperturbed term $\mathcal{H}_c$ is the part due to the central field approximation $V(r_i)$ and is given by

$$
\begin{aligned}
\mathcal{H}_c &= \sum_{i=1}^{N} \left(-\frac{1}{2}\nabla_i^2 + V(r_i) \right) \\
&= \sum_{i=1}^{N} h_i, \qquad h_i = -\frac{1}{2}\nabla_i^2 + V(r_i),
\end{aligned}
\tag{2.4}
$$

and the remaining term of the Hamiltonian, $\mathcal{H}_1$ is given by

$$\mathcal{H}_1 = \sum_{i<j}^{N} \frac{1}{r_{ij}} - \sum_{i}^{N} \left(\frac{Z}{r_i} + V(r_i) \right). \tag{2.5}$$

21

The spacial part central field wave function ψ_c can be written as

$$\psi_c = \phi_{n_1 \ell_1 m_{\ell_1}}(\mathbf{r}_1)\, \phi_{n_2 \ell_2 m_{\ell_2}}(\mathbf{r}_2) \cdots \phi_{n_N \ell_N m_{\ell_N}}(\mathbf{r}_N). \tag{2.6}$$

Since, $V(r)$ is central and spherically symmetric, $\phi_{n\ell m_\ell}(\mathbf{r})$ can be written as the product of radial functions $R_{n\ell}(r)$ times spherical harmonics $Y_{\ell m_\ell}(\theta, \varphi)$, and the normalized spin orbitals $\phi_{n\ell m_\ell m_s}(q)$ can be written as

$$\phi_{n\ell m_\ell m_s}(q) = \phi_{n\ell m_\ell}(\mathbf{r})\, \chi_{1/2, m_s}$$

$$= R_{n\ell}(r) Y_{\ell m_\ell}(\theta, \varphi) \chi_{1/2, m_s}$$

$$= \frac{P_{n\ell}}{r} Y_{\ell m_\ell}(\theta, \varphi) \chi_{1/2, m_s}, \tag{2.7}$$

with n, ℓ, m_ℓ, and m_s are the principal, orbital, magnetic, and spin projection quantum numbers, respectively. The principal quantum number n takes values of $n = 1, 2, 3, \ldots$, the orbital quantum number ℓ takes values of $\ell = 0, 1, 2, 3, \ldots, n-1$, which correspond to the spectroscopic notations $s, p, d, f, \ldots$, respectively. The values for the magnetic quantum number m are $m_\ell = -\ell, -\ell + 1, \ldots, +\ell$ and m_s takes values of $m_s = \pm 1/2$ with the positive sign for spin up and negative one for spin down. We should note that $R_{n\ell}(r)$ is different than the radial (hydrogenic) functions for the one-electron system because of the form of the potential $V(r)$. The radial orbitals $P_{n\ell}(r)$ are solutions to radial equation

$$\left[\frac{d^2}{dr^2} - \frac{\ell(\ell+1)}{r^2} - 2V(r) + 2E \right] P_{n\ell}(r) = 0. \tag{2.8}$$

The total energy E_c, in the central field approximation, is the sum of the individual electron energies,

$$E_c = \sum_{i=1}^{N} E_{n_i \ell_i}. \tag{2.9}$$

We define the total spin and angular momentum operators as $\mathbf{S} = \sum\limits_{i=1}^{N} \hat{s}_i$ and $\mathbf{L} = \sum\limits_{i=1}^{N} \hat{\ell}_i$, respectively. When we couple $\mathbf{L}$ and $\mathbf{S}$, we get the total angular momentum, $\mathbf{J} = \mathbf{L} + \mathbf{S}$ and this is known as Russell-Saunders coupling, or *LS*-coupling. This coupling scheme is used when the electron-electron repulsion energy is greater than the spin-orbit interaction. So, the total spin and total orbital angular momenta are conserved separately. We may realize that both $\mathcal{H}_{nr}$ and $\mathcal{H}_c$ commute with the total momentum operators $\mathbf{L}$, $\mathbf{S}$, $\mathbf{L}_z$, and $\mathbf{S}_z$, where the last two operators are the orbital and spin angular momentum operators along the z-axis, respectively.

$$[\mathcal{H}_c, \mathbf{L}] = 0, \quad [\mathcal{H}_c, \mathbf{S}] = 0, \quad [\mathcal{H}_c, \mathbf{J}] = 0, \quad \text{and} \quad [\mathbf{L}, \mathbf{S}] = 0. \tag{2.10}$$

The commutation relations between the components of the spin and orbital angular momenta are given by

$$[\mathbf{L}_i, \mathbf{L}_j] = i\epsilon_{ijk}\,\mathbf{L}_k \qquad \text{and} \quad [\mathbf{S}_i, \mathbf{S}_j] = i\epsilon_{ijk}\,\mathbf{S}_k\,, \tag{2.11}$$

where ϵ_{ijk} is the Levi-Civita symbol [153]. Thus, it is possible to obtain eigenfunctions of $\mathcal{H}_c$ which are simultaneously eigenfunctions for the operators $\mathbf{L}^2$, $\mathbf{L}_z$, $\mathbf{S}^2$, and $\mathbf{S}_z$ with eigenvalues $L(L+1)$, M_L, $S(S+1)$, and M_S in a.u., respectively . When we deal with the situation where the spin-orbit interaction is greater than the electron repulsion, another type of coupling should be used. In this situation, $\mathcal{H}$ does not commute with the spin-orbit part of the Hamiltonian, so we use the jj-coupling scheme, where $\mathcal{H}$ commutes with the total angular momentum, $\mathbf{J}$

$$[\mathcal{H}, \mathbf{J}] = 0, \quad \mathbf{J} = \sum_i \mathbf{j}_i, \quad \text{and} \quad \mathbf{j}_i = \hat{\ell}_i + \hat{s}_i. \tag{2.12}$$

23

2.2 Approximate Wave Functions for N-Electron Systems
2.2.1 Antisymmetrization and Slater Determinants

The trouble with the product wave functions in Eq. (2.6) is that it does not reflect the indistinguishability of the electrons. As we know, our total wave function $\psi_c(q_1, q_2, \cdots, q_N)$, for the N-electron system, should be antisymmetric and should satisfy the Pauli exclusion principle, namely that *no two electrons in an atom can have the same set of four quantum numbers*. Thus, the best way to describe $\psi_c(q_1, q_2, \cdots, q_N)$ is to use a Slater determinant [152, 154, 155]. For simplicity we replace the quantum numbers by $\alpha, \beta, \ldots, \nu$, and ψ_c can be written as:

$$\psi_c(q_1, q_2, \cdots, q_N) = \frac{1}{\sqrt{N!}} \begin{vmatrix} \phi_\alpha(q_1) & \phi_\beta(q_1) & \cdots & \phi_\nu(q_1) \\ \phi_\alpha(q_2) & \phi_\beta(q_2) & \cdots & \phi_\nu(q_2) \\ \vdots & \vdots & \ddots & \vdots \\ \phi_\alpha(q_N) & \phi_\beta(q_N) & \cdots & \phi_\nu(q_N) \end{vmatrix}. \qquad (2.13)$$

The $\sqrt{N!}$ is the normalization factor, which comes from the fact that there are $N!$ permutations of the electron coordinates $q_1, q_2, \cdots$, and q_N. We can write the electron configuration of the N-electron system as follows

$$(n_1\ell_1)^{w_1}(n_2\ell_2)^{w_2}...(n_m\ell_m)^{w_m} , \qquad N = \sum_{i=1}^{m} w_i, \qquad (2.14)$$

where w_i denotes the total number of electrons occupying the spin-orbitals in the sub-shell $n_i\ell_i$. For example, our Al-like target has the configuration $1s^2 2s^2 2p^6 3s^2 3p$ for the ground state. When electrons occupy the same subshell we refer to them as *equivalent electrons* such as the two electron in the subshell $3s$. Another important quantum number is the the the

parity π, which can be used to describe the state and is defined as

$$\pi = (-1)^{w_1 \ell_1}(-1)^{w_2 \ell_2}...(-1)^{w_m \ell_m} = \pm 1, \tag{2.15}$$

where positive values correspond to an even parity and negative values correspond to an odd parity. The total wave function for this configuration is referred to as a configuration state function (CSF) and is denoted by $\psi_c(\gamma L M_L S M_s)$ or in the ket form as $|\gamma L M_L S M_s\rangle$, where γ is used to specify the electron configuration and any additional quantum numbers required to completely describe the state (such as π). The spectroscopic notation for the energy term in *LS*-coupling is denoted by $^{2S+1}L^\pi$, where $2S + 1$ is called the *spin multiplicity* of the term and L is the total angular momentum, which can take values of $0, 1, 2, 3, 4, 5, 6, \ldots$ referring to $S, P, D, F, G, H, I, \ldots$ states. So, the ground state of Al-like term energy can be written as $3s^2 3p \, [^2P^o]$ and the superscript o is used to distinguish the odd parity.

2.2.2 The Variational Principle

The best form of solutions for radial wave functions can be obtained by an optimization method which we call variational method. This method is usually referred to as an optimization problem under constraint. So, there is a Lagrange multiplier ε such that the functional [156]

$$\mathcal{F}[\psi] = E[\psi] + \varepsilon \langle \psi | \psi \rangle \tag{2.16}$$

is stationary to the first order with respect to all variations $|\delta \psi\rangle$ satisfying the boundary conditions [157]. $E[\psi]$ is the expectation value of the Hamiltonian $\mathcal{H}$ and is given by

$$\langle \mathcal{H} \rangle = \frac{\langle \psi | \mathcal{H} | \psi \rangle}{\langle \psi | \psi \rangle} \equiv E[\psi]. \tag{2.17}$$

The value of E varies with the form of the state $|\psi\rangle$. But we assume that we found $|\psi\rangle$ for which E is stationary. This means that $\delta E = 0$ when $|\psi\rangle$ is replaced by $|\psi + \delta\psi\rangle$ under an infinitesimal change $|\delta\psi\rangle$. The variation δE is defined as $E[\psi + \delta\psi] - E[\psi]$ and can be calculated to the first order in $|\delta\psi\rangle$ as

$$
\begin{aligned}
\delta E &= \frac{\langle \psi + \delta\psi | \mathcal{H} | \psi + \delta\psi \rangle}{\langle \psi + \delta\psi | \psi + \delta\psi \rangle} - E \\
&= \frac{\langle \delta\psi | \mathcal{H} - E | \psi \rangle + \langle \psi | \mathcal{H} - E | \delta\psi \rangle}{\langle \psi | \psi \rangle + \langle \delta\psi | \psi \rangle + \langle \psi | \delta\psi \rangle} = 0,
\end{aligned}
\tag{2.18}
$$

and this expression vanishes only if

$$
\langle \delta\psi | \mathcal{H} - E | \psi \rangle + \langle \psi | \mathcal{H} - E | \delta\psi \rangle = 0,
\tag{2.19}
$$

where we assumed that $\langle \delta\psi | \psi \rangle = 0$ and it follows that

$$
\begin{cases}
\langle \psi | \mathcal{H} - E | \delta\psi \rangle = 0, \\
\langle \delta\psi | \mathcal{H} - E | \psi \rangle = 0.
\end{cases}
\tag{2.20}
$$

A similar method can be used for continuum states [146, 158].

2.2.3 Hartree-Fock (HF) Approximation

In the Hartree-Fock (HF) method, the approximate wave function consists of only one configuration state function. The radial function of each spin-orbital is assumed to depend only on n and ℓ quantum numbers and can be determined by using the variational principle. This general method of solution is known as Hartree-Fock or self-consistent field method [156], where each electron moves in a potential due to the nucleus and the charge distribution of all other $(N-1)$-electrons. When we calculate the matrix elements of $\mathcal{H}_{nr}$,

numerous algebraic integrals are involved, and we have to simplify them as much as possible. In order to do so, we divide $\mathcal{H}_{nr}$ into one- and two-electron operators as follows [152, 154]:

$$\mathcal{H}_{nr} = \sum_i^N f_i + \sum_{i<j}^N g_{ij}. \tag{2.21}$$

These operators are given respectively as

$$f_i = f(r_i) = -\frac{1}{2}\left(\nabla_i^2 + \frac{2Z}{r_i}\right) \quad \text{and}$$

$$g_{ij} = g(r_i, r_j) = \frac{1}{r_{ij}}. \tag{2.22}$$

If we assume that E_0 is the ground state energy of the system, then according to the variational method (see Sec. 2.2.2) we have

$$E_0 \leq E[\psi] = \langle\psi|H|\psi\rangle, \tag{2.23}$$

where ψ is a trial function in a Slater determinant form as Eq. (2.13) with the normalization

$$\langle\psi|\psi\rangle = 1. \tag{2.24}$$

This requires that all spin-orbitals are orthonormalized as

$$\langle\phi_\alpha|\phi_\beta\rangle = \sum_{m_{s_\alpha},m_{s_\beta}} \int \phi_\alpha^\dagger(q)\phi_\beta(q)dq = \delta_{m_{s_\alpha},m_{s_\beta}}\delta_{\alpha\beta}. \tag{2.25}$$

The matrix elements of the one-electron symmetric operator are simplified using the orthonormality properties of the one-electron spin-orbitals ϕ_γ as

$$\langle\psi|\sum_{i=1}^N f_i|\psi\rangle = \sum_\gamma \langle\phi_\gamma(q_i)|f_i|\phi_\gamma(q_i)\rangle = \sum_\gamma I_\gamma, \quad \gamma = \alpha, \beta, ..., \nu,$$

$$\tag{2.26}$$

with I_γ is defined as

$$I_\gamma = \langle \phi_\gamma(q_i) | f_i | \phi_\gamma(q_i) \rangle. \tag{2.27}$$

The matrix elements of the two-electron operator can be represented as

$$\langle \psi | \sum_{i<j} g_{ij} | \psi \rangle = \sum_{\gamma,\mu} \{ \langle \phi_\gamma(q_i)\phi_\mu(q_j) | \frac{1}{r_{ij}} | \phi_\gamma(q_i)\phi_\mu(q_j) \rangle$$
$$- \langle \phi_\gamma(q_i)\phi_\mu(q_j) | \frac{1}{r_{ij}} | \phi_\mu(q_i)\phi_\gamma(q_j) \rangle \}. \tag{2.28}$$

The summation over γ and μ runs over the $N(N-1)/2$ pairs of orbitals and Eq. (2.28) can be written as

$$\langle \psi | \sum_{i<j} g_{ij} | \psi \rangle = \frac{1}{2} \sum_\gamma \sum_\mu \{ \langle \phi_\gamma(q_i)\phi_\mu(q_j) | \frac{1}{r_{ij}} | \phi_\gamma(q_i)\phi_\mu(q_j) \rangle$$
$$- \langle \phi_\gamma(q_i)\phi_\mu(q_j) | \frac{1}{r_{ij}} | \phi_\mu(q_i)\phi_\gamma(q_j) \rangle \}$$
$$= \frac{1}{2} \sum_\gamma \sum_\mu [J_{\gamma\mu} - K_{\gamma\mu}] \quad ; \gamma, \mu = \alpha, \beta, ...\nu. \tag{2.29}$$

As a result of using the antisymmetrized wave functions to reflect the indistinguishability of the electrons, we end up with two terms. The first one, $J_{\gamma\mu}$, is called the *direct* term and the second one, $K_{\gamma\mu}$, is called the *exchange* term. We may realize that both $J_{\gamma\mu}$ and $K_{\gamma\mu}$ are real and symmetric too ($J_{\gamma\mu} = J_{\mu\gamma}$ and $K_{\gamma\mu} = K_{\mu\gamma}$). Now the total energy is given by

$$E[\psi] = \sum_\gamma I_\gamma + \frac{1}{2} \sum_\gamma \sum_\mu [J_{\gamma\mu} - K_{\gamma\mu}] = \mathcal{F}, \tag{2.30}$$

where $\mathcal{F}$ is the Fock operator.

When we introduce N^2 Lagrange multipliers, $\varepsilon_{\gamma\mu}$, such that it keeps $E[\psi]$ stationary

with respect to variations in the spin-orbitals ϕ_γ, the variational equation becomes

$$\delta E - \sum_\gamma \sum_\mu \varepsilon_{\gamma\mu} \delta\langle \phi_\mu | \phi_\gamma \rangle = 0, \tag{2.31}$$

with $\varepsilon_{\gamma\mu} = \varepsilon_{\mu\gamma}^\dagger$, so $\varepsilon_{\gamma\mu}$ are elements of the Hermitian matrix ε. We make the unitary transformation on the spin-orbitals ϕ_γ as $\acute{\phi}_\gamma = \sum_\mu U_{\gamma\mu} \phi_\mu$, where $U_{\gamma\mu}$ are the elements of a $N \times N$ unitary matrix. Such a transformation does not alter the Slater determinantal wave functions because it is a unitary transformation. If we choose U such that $\varepsilon_{\gamma\mu}$ becomes a diagonal matrix with elements $E_\gamma \delta_{\gamma\mu}$, then Eq. (2.31) becomes

$$\delta E - \sum_\gamma E_\gamma \, \delta\langle \phi_\gamma | \phi_\gamma \rangle = 0. \tag{2.32}$$

If we vary with respect to the spin-orbital ϕ_γ, then the variational equations become

$$\mathcal{F} | \phi_\gamma \rangle = E_\gamma | \phi_\gamma \rangle, \tag{2.33}$$

which are called Hartree-Fock equations [152, 156, 159, 160, 161, 162, 163]. Numerical solution for these coupled nonlinear differential equation is done iteratively starting with hydrogenic wave functions.

2.2.4 Hartree-Slater Method for Bound Orbitals

Slater introduced an approximate analytic form for atomic wave functions, which we refer to as Slater-type orbitals (STO) [164]. This approach is similar to the method used by Zener for writing an analytic form for wave functions of atoms with variational parameters [165]. In this method, bound electrons are assumed to move in a screened potential generated by the nucleus of charge Z and the charge distribution of the other remaining $(N-1)$-electrons. Our Al-like radial orbitals $P_j(r)$ are determined using this method.

The STO $P_j(r)$ in the jth subshell $n_j \ell_j$ can be written as [166]

$$P_j(r) = c \left[\frac{2z_j \lambda_j r}{n_j} \right]^{n_j} \exp \left(-\frac{z_j \lambda_j r}{n_j} \right), \tag{2.34}$$

where c is a normalization constant, λ_j is an adjustable scaling parameter, and z is the *effective charge* seen by the electron in the j-shell, which is given by

$$z_j = Z - \frac{(w_j - 1)}{2} - \sum_{i<j} w_i, \tag{2.35}$$

with w_i represents the number of electrons in the ith shell and the second term represents the approximate screening of all other $(w_j - 1)$ equivalent electrons.

The potential seen by an electron in the ith subshell is given by [166]

$$V_i(r) = -\frac{Z}{r} + \sum_j \frac{(w_j - \delta_{ij})}{r} \left[1 - \frac{\exp(-\rho_j)}{2n_j} \sum_{m=0}^{2n_j - 1} \frac{(2n_j - m)}{m!} \rho_j^m \right], \tag{2.36}$$

where $\rho_j = 2z_j \lambda_j r / n_j$. The radial scaling parameters for the entire Al-like ions will be presented in Chapter IV.

2.2.5 Configuration Interaction

We improve the eigenfunctions and eigenvalues for the N-electron target system by describing the wave functions as a linear combination of Slater determinants of the single-configurations (SC) wave functions which is known as *configuration interaction* (CI). So, we write the N-electron wave functions Ψ in terms of the wave functions ψ_i from different configurations with the same final symmetry [154] as

$$\Psi = \sum_{i=1}^{M} c_i \psi_i \, ; \quad \sum_i^M c_i^2 = 1, \tag{2.37}$$

where $c_i = \langle \psi_i | \Psi \rangle$ are the mixing coefficients and ψ_i are the eigenfunctions of the Hamiltonian $\mathcal{H}$ and they are orthonormalized ($\langle \psi_i | \psi_j \rangle = \delta_{ij}$). These extra configurations are included for correlation effects.

2.2.6 Distorted Wave Approximation

For the scattering problems, continuum orbitals are determined using the disteorted wave approximation (DWA). It assumes that the coupling between the states of the N-electron target and the continuum electron are weak and the continuum electron is assumed to move in a spherically symmetric screened potential due to the target electrons and the nucleus which are chosen to be a STO-Hartree potential as given in Eq. (2.36).

The radial equation for the continuum electron with angular momentum ℓ_i and linear momentum k_i can be written [167, 168] as

$$\left[\frac{d^2}{dr^2} - \frac{\ell_i(\ell_i + 1)}{r^2} - 2V_i(r) + k_i^2 \right] F_{k_i \ell_i}(r) = 0, \tag{2.38}$$

where $V_i(r)$ is the local potential due to the nucleus and all N-target electrons.

The asymptotic solutions of these equations for $r \to 0$ and $r \to \infty$, respectively can be written as

$$F_{k_i \ell_i}(r) = A_i r^{\ell_i + 1}, \text{ and} \tag{2.39}$$

$$F_{k_i \ell_i}(r) = \frac{1}{\sqrt{k_i}} \sin \left\{ k_i r + \frac{q}{k_i} \ln(2k_i r) - \frac{\ell_i \pi}{2} + \arg \Gamma(\ell_i + 1 - \frac{iq}{k_i}) + \delta \right\},$$
$$\tag{2.40}$$

where q is the ionic charge defined as $q = Z - N$ and δ is the distorted-wave phase shift which is zero when $V_i(r) = q/r$.

31

The normalization of the continuum orbitals $F_{k\ell}(r)$ is given by

$$\int_0^\infty F_{k\ell}(r)\, F_{k'\ell}(r)\, dr = \pi\delta(k - k'), \tag{2.41}$$

where k is the linar momentum of the continuum electron.

Higher bound orbitals $P_{n\ell}(r)$ are determined using the following approximation [90]

$$\lim_{n\to\infty} P_{n\ell}(r) = \sqrt{\frac{2q}{\pi n^3}}\, F_{k\ell}|_{k=0}, \tag{2.42}$$

2.3 Relativistic Corrections

The ideal way to consider the relativistic effects is to solve Dirac equation [169], but this requires dealing with four radial functions for each subshell $n\ell$ instead of one and this is cumbersome and time consuming. Since we can not ignore these effects, especially the spin-orbit term, which scales as Z^4. This term, we found to have profound effect on our new DR cross sections and rate coefficients for Al-like isoelectronic sequence (see Chapter IV). For our calculations, which involve systems with $Z \leq 30$, it is safe to go beyond the non-relativistic approximation by including these extra effects to $\mathcal{H}_{nr}$, which arise from the expansion of Dirac equation in powers of αv, where $\alpha = 1/c$ is the fine structure constant, c is the speed of light in vacuum (see Appendix A), and v is the electron velocity, with the assumption $v \ll c$ and ignoring terms that include α^3 and higher orders. These extra terms are considered as perturbations and the resulting Hamiltonian is known as the Breit-Pauli Hamiltonian $\mathcal{H}_{BP}$ [141, 154, 152, 156] and can be written as

$$\mathcal{H}_{BP} = \mathcal{H}_{nr} + \mathcal{H}_{rel}, \tag{2.43}$$

where $\mathcal{H}_{nr}$ and $\mathcal{H}_{rel}$ are the non-relativistic and relativistic corrections, respectively. $\mathcal{H}_{rel}$ can be divided into nonfine structure (nfs) and fine structure (fs) terms as follows

$$\mathcal{H}_{rel} = \mathcal{H}_{nfs} + \mathcal{H}_{fs}. \tag{2.44}$$

The nonfine structure part can be written as

$$\mathcal{H}_{nfs} = \mathcal{H}_{mv} + \mathcal{H}_D + \mathcal{H}_{oo} + \mathcal{H}_{ssc}, \tag{2.45}$$

which shifts the nonrelativistic energy levels without splitting the levels. The mass-velocity term $\mathcal{H}_{mv}$ is given by

$$\mathcal{H}_{mv} = -\frac{\alpha^2}{8} \sum_{i=1}^{N} \nabla_i^4, \tag{2.46}$$

the one and two-body Darwin terms are

$$\mathcal{H}_D = -\frac{\alpha^2 Z}{8} \sum_{i=1}^{N} \nabla_i^2 \left(\frac{1}{r_i} \right) + \frac{\alpha^2}{4} \sum_{i<j}^{N} \nabla_i^2 \left(\frac{1}{r_{ij}} \right), \tag{2.47}$$

the spin-spin contact term, $\mathcal{H}_{ssc}$, which accounts for the spin magnetic moments of two electrons occupying the same space, is given by

$$\mathcal{H}_{ssc} = -\frac{8\pi\alpha^2}{3} \sum_{i<j}^{N} (\mathbf{s}_i.\mathbf{s}_j) \, \delta(\mathbf{r}_i.\mathbf{r}_j), \tag{2.48}$$

and the orbit-orbit term $\mathcal{H}_{oo}$, which accounts for two orbital moments, is given by

$$\mathcal{H}_{oo} = -\frac{\alpha^2}{2} \sum_{i<j}^{N} \left[\frac{\mathbf{p}_i.\mathbf{p}_j}{r_{ij}} + \frac{\mathbf{r}_{ij}(\mathbf{r}_{ij}.\mathbf{p}_i).\mathbf{p}_j}{r_{ij}^3} \right]. \tag{2.49}$$

The fine structure term, $\mathcal{H}_{fs}$, which splits the non-relativistic energy levels into a series of closely-spaced fine structure levels, is given by

$$\mathcal{H}_{fs} = \mathcal{H}_{so} + \mathcal{H}_{soo} + \mathcal{H}_{ss}, \tag{2.50}$$

where $\mathcal{H}_{so}$ is the spin-orbit interaction, which represents the interaction of the spin and angular momentum of the electrons in the field of the nucleus and is given by

$$\mathcal{H}_{so} = \frac{\alpha^2 Z}{2} \sum_{i=1}^{N} \frac{1}{r_i} \frac{dV}{dr_i} \ell_i . \mathbf{s}_i . \tag{2.51}$$

The spin-other-orbit $\mathcal{H}_{soo}$ is given by

$$\mathcal{H}_{soo} = -\frac{\alpha^2}{2} \sum_{i<j}^{N} \frac{\mathbf{r}_{ij} \times \mathbf{p}_i}{r_{ij}^3} . (\mathbf{s}_i + 2\mathbf{s}_j), \tag{2.52}$$

and the spin-spin $\mathcal{H}_{ss}$ interaction is given by

$$\mathcal{H}_{ss} = \alpha^2 \sum_{i<j}^{N} \frac{1}{r_{ij}^3} \left[\mathbf{s}_i . \mathbf{s}_j - \frac{3}{r_{ij}^2} (\mathbf{s}_i . \mathbf{r}_{ij})(\mathbf{s}_j . \mathbf{r}_{ij}) \right] . \tag{2.53}$$

It is worth to mention that $\mathcal{H}_{BP}$ commutes with the total angular momentum of the system ($[\mathcal{H}_{BP}, \mathbf{J}] = 0$), so eigenfunctions for $\mathcal{H}_{BP}$ are eigenfunctions for both $\mathbf{J}^2$ and $\mathbf{J}$. These eigenfunctions can be obtained by the intermediate coupling [154, 155], in which we coupling the total angular $\mathbf{L}$ and the total spin $\mathbf{S}$ momenta as follows

$$|JM_J\rangle = \sum_{M_L M_S} C_{M_L M_S M_J}^{L S J} |LSM_LM_S\rangle, \tag{2.54}$$

where $C_{M_L M_S M_J}^{L S J}$ are known as Clebsch-Gordan coefficients.

2.4 MultiConfiguration Breit-Pauli Method

In the multiconfiguration Breit-Pauli method (MCBP), target wave functions are described as a CI expansion as discussed in Sec. 2.2.5 and using the Breit-Pauli Hamiltonian $\mathcal{H}_{BP}$, which is given in Eq. (2.43). These wave functions can be written in both LS and IC-coupling schemes, respectively as

$$\Psi(\gamma LS) = \sum_{i=1}^{M} c_i \psi_i(\gamma LS), \quad \text{and} \tag{2.55}$$

34

$$\Psi(\gamma J M_J) = \sum_{i=1}^{M} c_i \psi_i(\gamma J M_J), \tag{2.56}$$

with $\psi(\gamma J M_J)$ is obtained using the coupling described in Eq. (2.54). This requires previous determination of ψ_i either from HF or HS methods, then we seek solutions for the expansion coefficients by minimizing the energy, which leads to the following linear equations

$$\sum_{i=1}^{M}(H_{ij} - E\delta_{ij})c_i = 0, \tag{2.57}$$

where the matrix elements H_{ij} are given by $H_{ij} = \langle \psi_i | \mathcal{H}_{BP} | \psi_j \rangle$ and the energies E can be determined from the secular determinant

$$|H_{ij} - E\delta_{ij}| = 0, \tag{2.58}$$

then E is used back in Eq. (2.57) to solve for the mixing coefficients c_i.

Despite the accurate description of this method, the convergence is usually slow and the numerical work increases rapidly as the number of configurations is increased. Thus, we usually include only those configurations whose energies are close to each other and therefore interact more strongly. We use the AUTOSTRUCTURE atomic structure package and collision code [32] for calculating energy levels or term energies in the case of LS-coupling. The beauty of this cod is that you can use orthogonal bases, non-orthogonal sets of orbitals, one set for each configuration to account for the relaxation effects due to different screening in the initial and final states, and you can use your own orbitals obtained from multiconfiguration Hartree-Foch MCHF code [160].

2.5 Transition Rates

After finding the approximate solutions for our wave functions and calculating their energy levels, the first application is to calculate the DR and photoabsorption cross sections. These calculations depend on calculating transition rates in advance. In this section we give a brief summary for radiative and Auger transition rates. These rates are mainly calculated from the famous quantum mechanics expression which is called " Fermi's Golden Rule" [149, 154, 155, 170]. This rule is derived in the study of the time-dependent perturbation theory, where we assume that the Hamiltonian has a small time-dependent perturbation $\mathcal{H}' = -i\mathbf{A}.\nabla$, where $\mathbf{A}$ is the vector potential. Following Dirac's method of variation of constants, the transition probability per unit time (transition rate), in first order perturbation theory from an initial state $|a\rangle$ to a final state $|b\rangle$, is given in a.u. by

$$W_{a \to b} = 2\pi |\langle b|\mathcal{H}'|a\rangle|^2 \rho_b(E), \tag{2.59}$$

where $\rho_b(E)$ is the density of final states (the number of states per unit energy).

2.5.1 Radiative Transition Rates

In the DR process, radiative transitions usually occur between resonant doubly-excited state $|\Psi_d\rangle$ to a final bound state $|\Psi_f\rangle$ with photon emission. Applying the dipole approximation ($e^{i\mathbf{k}.\mathbf{r}} = 1 + i\mathbf{k}.\mathbf{r} + \dots\dots = 1$) to the Hamiltonian, and neglecting $\mathbf{A}^2$, the spontaneous radiative transition rate [154, 155, 170] is given by

$$A^r(d \to f) = \frac{4}{3}\alpha^3 w^3 \left|\langle \Psi_f|\mathcal{D}|\Psi_d\rangle\right|^2, \tag{2.60}$$

where α is the fine structure constant, $w = w_f - w_d$ is the photon energy, and $\mathcal{D} = \sum_{i=1}^{N} \mathbf{r}_i$ is the electric dipole operator. The matrix elements follow selection rules arising from carrying the integrations or applying Wigner-Eckart theorem, where we write $\mathbf{r}$ in a tensor form of rank one. The *dipole selection rules* for the $A^r(d \rightarrow f)$ are, for *LS*-coupling, $\Delta S = 0, \Delta M_S = 0, \Delta \pi = \pm 1, \Delta L = 0, \pm 1$, and $\Delta M_L = 0, \pm 1$. For IC-coupling, the selection rules are $\Delta \pi = \pm 1, \Delta J = 0, \pm 1$, and $\Delta M_J = 0, \pm 1$ [149, 154, 155, 170].

In a non-relativistic, *LS* approximation, the dipole matrix element, $\mathcal{D}_{df} = \langle \Psi_f | \mathbf{r} | \Psi_d \rangle$, can be written in length and velocity forms as [171]

$$\mathcal{D}_{df} = \begin{cases} \langle \Psi_f | \sum_{i=1}^{N} \mathbf{r}_i | \Psi_d \rangle & \text{Length Form} \\ -\frac{1}{w} \langle \Psi_f | \sum_{i=1}^{N} \nabla_i | \Psi_d \rangle & \text{Velocity Form.} \end{cases} \tag{2.61}$$

In our calculations, we compare results obtained in these forms for the seek of completeness of the wave function [154, 170]. Generally, doubly-excited states may radiatively decay to many final states and we add these final states to get the total radiative width Γ^r as follows

$$\Gamma^r = \sum_f A^r(d \rightarrow f) \tag{2.62}$$

2.5.2 Auger Transition Rates

When we study electron-ion recombination, specially the DR process, we deal with infinite number of doubly-excited states. These doubly-excited states can decay back to their initial states or to an excited state of the N-electron ion (Al-like system in our case) and the emitted electrons are referred to as Auger electrons. Auger transitions occur due to the electron-electron interaction term in the Hamiltonian. For example, the doubly-excited state $3s^2 3d[^2D_{3/2}]n\ell$ of Si-like ions, which can be formed by EIE from the ground state

$3s^2 3p[^2P_{1/2}]$ of Al-like ions, can Autoionize to the ground state of Al-like or to its first excited state $(3s^2 3p[^2P_{3/2}] + e^-)$.

The partial autoionization transition rate $A^a(d \rightarrow c)$ from a doubly-excited state $|\Psi_d\rangle$ to a continuum state $|\Psi_c\rangle$ can be calculated using Fermi's Golden Rule [149, 152, 154] as follows

$$A^a(d \rightarrow c) = 2\pi \left| \left\langle \Psi_c \left| \sum_s^{N+1} \frac{1}{|\mathbf{r}_s - \mathbf{r}_{N+1}|} \right| \Psi_d \right\rangle \right|^2. \qquad (2.63)$$

In conclusion, Auger transitions may occur when a doubly-excited state is located above the ionization limit with a vacancy exists below at least two active electrons. The energy lost when an electron fills this vacancy is enough to liberate the other electron to the continuum state of the same parity $(\Delta\pi = 0)$.

The total Auger width Γ^a is given by

$$\Gamma^a = \sum_{\ell_c} A^a(d \rightarrow i) + \sum_{m, \ell'_c} A^a(d \rightarrow m), \qquad (2.64)$$

where the first term gives Auger rates for the decay to the initial ground state i with different continua ℓ_c and the the second term represents the sum over all other possible autoionizaing states.

2.6 Electron-Ion Recombination

As mentioned in Chapter I, electron-ion collisions include direct and indirect (resonant) processes. The former is referred to as radiative recombination (RR) and the latter is called dielectronic recombination (DR). When a free electron e^- collisionally collide with an ion

A with a charge q, both processes can be schematically represented as

$$e^- + A_i^{q+} \rightarrow A_f^{(q-1)+} + \omega \quad \text{(RR)}, \quad \text{and} \tag{2.65}$$

$$e^- + A_i^{q+} \rightleftharpoons [A_f^{(q-1)+}]^{**} \rightarrow A_f^{(q-1)+} + \omega \quad \text{(DR)}, \tag{2.66}$$

where $[A_f^{(q-1)+}]^{**}$ is a doubly-excited state and ω is the photon energy. We use the independent processes approximation, in which interference between RR and DR is very small even for ions with small degree of ionization q [98, 172]. So, we neglect the interference between RR and DR processes and treat them separately. The second approximation is to consider first order perturbation theory to calculate their cross sections.

2.6.1 Cross Sections

The RR cross section for an initial state $|\Psi_i\rangle$ of a target ion plus continuum electron with linear momentum k_i to a final bound state $|\Psi_f\rangle$ is given by

$$\sigma^{RR} = \frac{16\pi\omega^3\alpha^3}{3k_i^3} \left| \langle \Psi_f | \sum_{s=1}^{N+1} \mathbf{r}_s | \Psi_i \rangle \right|^2. \tag{2.67}$$

The partial DR cross section, as a function of center of mass energy E from an initial metastable state i through a doubly-excited state d to a final state f is given by

$$\sigma_{fi}^{DR} = S^d(i \rightarrow f)L^d(E), \tag{2.68}$$

where $L^d(E)$ is the Lorentzian line-shape of the resonance with an energy E_d and width Γ^d and is given by

$$L^d(E) = \frac{\Gamma^d}{2\pi} \frac{1}{(\Gamma^d/2)^2 + (E - E_d)^2}, \tag{2.69}$$

39

and $S^d(i \to f)$ is the partial integrated DR cross section, which is proportional to the capture rate times the radiative branching ratio and is given by

$$S^d(i \to f) = \frac{(2\pi a_0 I_H)^2}{E} \frac{G_d}{2G_i} \tau_0 \sum_\ell A^a(d \to i, E\ell) B^r(d \to f), \qquad (2.70)$$

$$B^r(d \to f) = \frac{A^r(d \to f)}{\sum_{m,\ell} A^a(d \to m, E\ell) + \sum_{f'} A^r(d \to f')}, \qquad (2.71)$$

where $(2\pi a_0)^2 \tau_0 = 2.6741 \times 10^{-32}$ cm^2.s, I_H is the ionization potential energy of the hydrogen atom, G_d is the statistical weight of the $(N+1)$-electron doubly-excited resonance state d, G_i is the statistical weight of the N-electron target state (Al-like ion), and $B^r(d \to f)$ is the radiative branching ratio. The ionization potential of hydrogen I_H, the energy E, and the total width Γ^d are calculated in the same units of energy, the radiative and Auger rates (A^r, A^a) are calculated in inverse second. We may realize that the summations over m and f' include all possible autoionization and radiative states from a given resonant state d. Thus, the sum over m accounts for excitations which lead to the total autoionization rate Γ^a and the sum over f' includes all bound and other states that may radiatively decay by cascade to other autoionizing states, giving the total radiative rate Γ^r.

If we assume that there is no overlap between RR and DR resonances (i.e. isolated resonance approximation), the partial energy-averaged DR cross section $\bar{\sigma}^{DR}$ is given by

$$
\begin{aligned}
\bar{\sigma}^{DR}_{fi} &= \frac{1}{\Delta E} \int_{E_c - \Delta E_c/2}^{E_c + \Delta E_c/2} \sigma^{DR}_{fi}(E') dE' \\
&= \frac{1}{\Delta E} \sigma^{DR}_{fi}(E_c),
\end{aligned}
\qquad (2.72)
$$

where the energy bin width ΔE is chosen to be larger than the largest resonance width and small compared to the experimental width and E_c is continuum energy.

40

The total DR cross section is then obtained by summing over all possible doubly-excited states d and final bound states f below the ionization limit and is given by

$$\sigma^{DR} = \sum_{f,d} \bar{\sigma}_{fi}^{DR}. \tag{2.73}$$

2.6.2 Maxwellian Rate Coefficients

The Maxwellian-averaged rate coefficient $\alpha(T)$ can be calculated by convolving the cross section with the Maxwell-Boltzmann distribution function as follows

$$\alpha(T) = \langle v\sigma \rangle = \int_0^\infty v\, \sigma(E)\, f_{MB}(E, k_B T)\, dE, \tag{2.74}$$

where $f_{MB}(E, k_B T)$ is the Maxwell-Boltzmann distribution which can be written in velocity and energy forms, respectively as

$$f_v(v)dv = \left(\frac{m_e}{2\pi T}\right)^{3/2} 4\pi v^2 \exp\left(-\frac{mv^2}{2T}\right) dv,$$

$$f_E(E)dE = 2\sqrt{\frac{E}{\pi}} \frac{1}{(k_B T)^{3/2}} \exp\left(-\frac{E}{k_B T}\right) dE. \tag{2.75}$$

In our DR calculations, we assume that $L^d(E)$ can be represented as Dirac delta function

$$L^d(E) = \delta(E - E_c) \tag{2.76}$$

then, $\alpha^{DR}(T)$ can be given by

$$\alpha^{DR}(T) = \int_0^\infty v \sum_{f,d} S^d(i \to f)\, \delta(E - E_c)\, f_E(E)dE,$$

$$= \sum_{f,d} S^d(i \to f) v(E_c)\, f_E(E_c). \tag{2.77}$$

Instead of extrapolating the rates by $1/n^3$ method, we follow a more accurate technique, in which bound orbitals are approximated by a normalized zero-energy continuum

orbital for $n > 15 + \ell^2/4$ using a quantum defect approximation as in Eq. (2.41). For each $n\ell$, diagonalizations for N and $N + 1$ electron-Hamiltonians are performed and followed by calculations for autoionization and radaitive rates A^a and A^r, respectively. Rate coefficients are then calculated by using a post-processor ADASDR, in which radiative transition between highly excited Rydberg states are computed hydrogenically.

The theoretical rate coefficient, $\alpha^{DR}(\upsilon_0)$, can be convolved in another form for comparison with the merged beam experimental results as follows

$$\alpha^{DR}(\upsilon_0) = <\upsilon\sigma> = \int \sigma(\upsilon)\upsilon f(\upsilon_0, \mathbf{v}) d\mathbf{v}, \tag{2.78}$$

where $f(\upsilon_0, \mathbf{v})$ is the merged-beams electron velocity distribution in the center of mass frame of the ions and $\upsilon_0 = \sqrt{2E_0/m_e}$. The experimental velocity distribution, $f(\upsilon_0, \mathbf{v})$, is a flattened Maxwellian [173] which is characterized by its parallel and perpendicular temperatures $T_\parallel$ and $T_\perp$ respectively, with $T_\parallel \ll T_\perp$:

$$f(\upsilon_0, \mathbf{v}) = \sqrt{\frac{m_e}{2\pi k T_\parallel}} \exp\left[\frac{-m_e(\upsilon_\parallel - \upsilon_0)^2}{2kT_\parallel}\right] \frac{m_e}{2\pi T_\perp} \exp\left(\frac{-m_e\upsilon_\perp^2}{2kT_\perp}\right). \tag{2.79}$$

In traveling from the electron cooler to the detector, recombined ions with higher n-values may re-ionized by the motional electric field induced in various magnetic elements in the ring. This leads to an-n_{cut} (cutoff) above which all the recombined states will be ionized. This hard cut-off at n_{cut} is given by the hydrogenic expression [171].

$$n_{cut} = \left(6.2 \times 10^8 \frac{q^3}{F}\right)^{1/4}, \tag{2.80}$$

where q is the ionic charge and F is the electric field strength in V cm^{-1}. However, during the time of flight T_f from the cooler to the analyzer, recombined ions with $n > n_{cut}$ may

radiatively decay to $n < n_{cut}$, thus they can survive and be counted by the analyzer. This was modeled theoretically [174, 175] by the survival probability as

$$\mathcal{P}_{n\ell} = 1 - \frac{T_{n\ell}}{T_L} \exp\left(\frac{-T_f}{T_{n\ell}}\right) \left[\exp\left(\frac{T_L}{2T_{n\ell}}\right) - \exp\left(\frac{-T_L}{2T_{n\ell}}\right)\right], \qquad (2.81)$$

where $T_{n\ell}$ and T_L are the lifetime of the Rydberg series (usually hydrogenic) and the time of flight through the merged-beams section of the cooler, respectively.

The Maxwellian-averaged DR rate coefficients $\alpha^{DR}(T)$ are fit to the following formula

$$\alpha^{DR}(T) = T^{-3/2} \sum_i c_i \, \exp\left(-\frac{E_i}{T}\right). \qquad (2.82)$$

where, E_i is in units of the temperature T (eV or K) and c_i has units of $\mathrm{cm^3\,s^{-1}[eV\ or\ K]^{3/2}}$.

2.7   Non-Relativistic R-Matrix Method

Wigner first introduced the R-matrix method to study the resonance reactions in nuclear physics [142, 143]. Then the theory was developed and applied more generally for nuclear physics [144] and followed by applications to atomic physics by Burke and coworkers [145, 146, 147, 176, 177, 178]. The theory starts by dividing the configuration space into two regions by a sphere of radius $r = a$ centered on the target nucleus (N-electron syatem) where r is the coordinate of the scattered electron relative to the target nucleus (see Fig. 2.1). The R-matrix boundary, $r = a$, is chosen such that all electron orbital amplitudes in the target are negligible beyond the boundary $r > a$. In the internal region $r \leq a$, electron exchange and correlation between the scattered electron and the N-electron target are important and the $(N + 1)$-electron system behaves in a similar way to a bound state. So, a configuration interaction (CI) expansion of this complex is applied. In the external region,

$r > a$, electron exchange between the scattered electron and the target can be neglected, so the scattered electron moves in the long-range multipole potential of the target. This potential is local and the solution in this region can be obtained using an asymptotic expansion or by using perturbation theory. The wave functions are solved in both regions, and inverse logarithmic boundary conditions are used to match the inner and outer solutions.
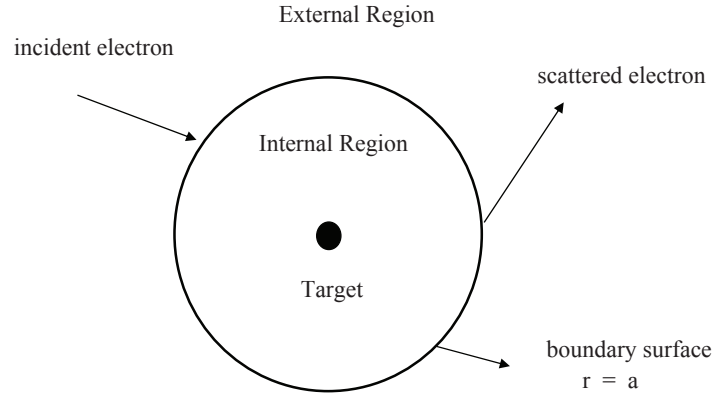
Figure 2.1   Schematic diagram for the configuration space in the R-matrix theory.

The wave function Ψ for the $(N+1)$-electron system is a variational approximation to the time independent Schrödinger equation

$$\mathcal{H}_{N+1}\,\Psi = E\,\Psi, \tag{2.83}$$

where E is the total energy and $\mathcal{H}_{N+1}$ is the $(N+1)$-electron Hamiltonian. For light atoms and ions, we can neglect the relativistic effects, and this Hamiltonian can be described as

$$\mathcal{H}_{N+1} = \sum_{i=1}^{N+1}\left(-\frac{1}{2}\nabla_i^2 - \frac{Z}{r_i}\right) + \sum_{i>j=1}^{N+1}\frac{1}{r_{ij}}. \tag{2.84}$$

The solutions Ψ of Eq. (2.83) are constructed as products of one-electron functions in spherical polar coordinates. Thus, configuration mixing is required. We introduce a set of target states and pseudo-states Φ_i, and their corresponding energies E_i^N by the equation

$$\langle \Phi_i | \mathcal{H}_N | \Phi_j \rangle = E_i^N \delta_{ij}, \tag{2.85}$$

where $\mathcal{H}_N$ is the target Hamiltonian given by Eq. (2.84) with $N + 1$ is replaced by N. These states are written as a CI expansion in terms of basis configurations ϕ_j by

$$\Phi_i = \sum_j b_{ij} \, \phi_j. \tag{2.86}$$

Here, ϕ_j are the SC electron wave functions of Slater determinant form as discussed in Sec. 2.2.1.

The solution to Eq. (2.83), in the internal region, is obtained by introducing the Bloch operator B_{N+1} [144, 179] which is given by

$$B_{N+1} = \sum_{i=1}^{N+1} \frac{1}{2} \delta(r_i - a) \left(\frac{d}{dr_i} - \frac{b-1}{r_i} \right), \tag{2.87}$$

where b is an arbitrary constant and this guaranties that $\mathcal{H}_{N+1} + B_{N+1}$ is a Hermitian operator. Now the solution for Eq. (2.83) is given by

$$\Psi = (\mathcal{H}_{N+1} + B_{N+1} - E)^{-1} B_{N+1} \Psi. \tag{2.88}$$

In order to solve this equation, we look for solutions ψ_k that can be written as,

$$\psi_k = \mathcal{A} \sum_{ij} c_{ijk} \bar{\Phi}_i \frac{1}{r_{N+1}} u_{ij}(r_{N+1}) + \sum_j d_{jk} \Upsilon_j, \tag{2.89}$$

where $\mathcal{A}$ is the anti-symmetrization operator. $\bar{\Phi}_i$ is obtained by coupling the target wave functions Φ_i with the angular and spin functions of the scattered electron. Υ_j is constructed

from the bound orbitals, $P_{n\ell}(r)$, and is included for the completeness of the total wave function. The continuum orbitals $u_{ij}(r)$ for each angular momentum ℓ_i are obtained by solving the following equation

$$\left(\frac{d^2}{dr^2} - \frac{\ell_i(\ell_i + 1)}{r^2} + V_0(r) + k_{ij}^2 \right) u_{ij}(r) = \sum_n \varepsilon_{ijn} P_{n\ell_i}(r) \qquad (2.90)$$

which satisfies the boundary conditions,

$$u_{ij}(0) = 0, \qquad \frac{a}{u_{ij}(a)} \left[\frac{du_{ij}(r)}{dr} \right]_{r=a} = b. \qquad (2.91)$$

Here ε_{ijn} are Lagrange multipliers which are used to satisfy the orthogonality condition $\langle u_{i\ell}|P_{n\ell}\rangle = 0$, b is an arbitrary constant and is normally set to zero, c_{ijk} and d_{ik} are the expansion coefficients.

Now, the wave function in the internal region is defined as

$$\Psi_{in} = \sum_k A_{Ek} \psi_k, \qquad (2.92)$$

with A_{Ek} is the expansion coefficient. The elements of the R-matrix [145] can be given by

$$R_{ij}(E) = \frac{1}{2a} \sum_k \frac{w_{ik}(a)w_{kj}(a)}{E_k - E}, \qquad (2.93)$$

where w_{ik} is the surface amplitude which is defined as $w_{ik} = a\langle \bar{\Phi}|\psi_k\rangle_{r=a}$, where Wigner's one channel case [142] is generalized to M channels [144].

In the outer region, anti-symmetrization is not required and the total wave function can be written as

$$\Psi_{out} = \sum_i \bar{\Phi}_i \frac{1}{r_{N+1}} F_i(r_{N+1}). \qquad (2.94)$$

46

Substituting Ψ_{out} into Eq. (2.83), we can determine the radial wave functions $F_i(r)$ for each channel i:

$$\left(\frac{d^2}{dr^2} - \frac{\ell_i(\ell_i + 1)}{r^2} + \frac{2Z}{r} + k_i^2 \right) F_i(r) = 2 \sum_{j=1}^{M} V_{ij}(r) F_{ij}(r). \qquad (2.95)$$

Here ℓ_i and k_i^2 are the channel angular momenta and energies $\{k_i^2 = 2(E - E_i^N)\}$. V_{ij} is the potential matrix which is given by

$$V_{ij}(r) = \langle \bar{\Phi}_i | \sum_{m=1}^{N} \frac{1}{r_{m,N+1}} | \bar{\Phi}_j \rangle. \qquad (2.96)$$

The external radial wave functions $F_{ij}(r)$ has the following asymptotic solutions at $r \to \infty$

$$F_{ij}(r) \underset{r \to \infty}{\sim} \begin{cases} \frac{1}{\sqrt{k_i}} (\sin \theta_i \, \delta_{ij} + \cos \theta_i \, K_{ij}), & k_i^2 > 0 \quad \text{open channel} \\ e^{-\phi_i} \delta_{ij}, & k_i^2 < 0 \quad \text{closed channel} \end{cases} . \qquad (2.97)$$

The second index j on F_{ij} denotes the linearly independent solutions, $\mathbf{K}$ is the reactance matrix, θ_i and ϕ_i are defined as

$$\theta_i = k_i r - \frac{\ell_i \pi}{2} + \frac{q}{k_i} \ln 2k_i r + \arg \Gamma(\ell_i + 1 - i \frac{q}{k_i})$$
$$\phi_i = |k_i| r - \frac{q}{|k_i|} \ln(2|k_i|r), \qquad (2.98)$$

where q is the residual target charge $q = Z - N$.

Since the R-matrix must match smoothly between the inner and outer region solutions at the boundary $r = a$, we have

$$\mathbf{R}_{in}(E, r = a) \left[a \Psi'_{out}(E, a) \right] = \Psi_{out}(E, a) . \qquad (2.99)$$

This boundary condition gives us the solution for the reactance matrix $\mathbf{K}$, from which the scattering matrix is determined as

$$\mathbf{S} = \frac{\mathbf{I} + i\mathbf{K}}{\mathbf{I} - i\mathbf{K}} . \qquad (2.100)$$

47

Knowledge of **S**-matrix-normalization of the continuum states Ψ_f allows the photoioniza-tion cross section [180] to be computed from an initial state Ψ_i as

$$\sigma^{\mathrm{PI}}(E) = \frac{4\pi^2 w}{3c} \, |\langle \Psi_f | \mathcal{D} | \Psi_i \rangle|^2 \ .$$ (2.101)

For $E < 0$, on the other hand, we get an eigenvalue equation for the binding energy and the wave function Ψ_i of the initial state.

2.7.1 Auger Width Using Smith Time-Delay Method

Usually, we use AUTOSTRUCTURE code [32] to determine Auger width for decaying resonant states as described in Sec. 2.5. Another alternative method that can be used in the R-matrix calculations is based on the the Smith time-delay method [181]. As pointed out by Smith, the scattering matrix **S** and the life time matrix **Q** are related by the following relation

$$\mathbf{Q} = -i\mathbf{S}^\dagger \frac{d\mathbf{S}}{dE}.$$ (2.102)

The scattering matrix **S** is determined from the reactance matrix **K** as in Eq. (2.100). The trace of **Q**, which is the sum of the diagonal elements $\mathbf{Q}_{ii}$ has an analytic form near the resonance as a Lorentzian profile and is given by

$$\mathbf{Q}_{ii}(E) = \frac{\Gamma^a}{(E - E_r)^2 + (\Gamma^a/2)^2}$$ (2.103)

where Γ^a is the Auger width of the decaying resonance and E_r is the resonance position.

CHAPTER III

M-SHELL DIELECTRONIC RECOMBINATION FOR ARGON IONS

3.1 Introduction

Argon is a valuable diagnostic element for magnetically controlled fusion plasmas [112, 113]. High-pressure gas-jet injection of argon and other rare gases has been found to mitigate the tokamak plasma disruptions [114]. One important factor in designing the future operation of the International Tokamak Experimental Reactor (ITER) is to avoid the disruption of plasmas. Line ratios from argon ions have been shown to be accurate electron density and temperature diagnostics [182]. Abdallah and Clark [183] investigated the density effect on the populations of all ion stages of argon. The atomic collision processes needed for tokamak transport modeling involve mainly electron-ion collisions and include excitation, ionization, and recombination. Accurate ionization and recombination rate coefficients for low ion stages of argon are needed. In particular, using level-resolved distorted-wave methods to calculate dielectronic recombination for M-shell ions leads to prohibitively large calculations.

In this chapter, electron-impact DR cross sections and rate coefficients, for $\Delta n_c = 0$ core excitations are calculated in a configuration-average distorted-wave approximation for $Ar^+ - Ar^{7+}$. We start by introducing calculations for Ar^{7+} and Ar^{6+} and compare our results with the available recent level-resolved distorted-wave calculations [101, 102] which can provide a check on our method. As we move along the M-shell ions, the open-shell nature of the atomic structure has made level-resolved distorted-wave calculations

difficult for recombination cross sections and rate coefficients for $Ar^+ - Ar^{5+}$. We note that storage-ring experimental measurements of recombination cross sections for all the M-shell ions from $Ar^+ - Ar^{7+}$ are still in the planning stages. The DR data produced here were then used in determining the fractional abundance for Argon.

In Sec. 3.2, we present a brief review of the configuration-average distorted wave theory. In Sec. 3.3, DR rate coefficients for $Ar^+ - Ar^{7+}$ are presented and compared with available level-resolved distorted-wave calculations [101, 102].

3.2 Methodology

In the independent processes approximation, the total recombination cross section is given by

$$\sigma^{Rec} = \sigma^{RR} + \sum_j \sigma^j_{cap} B^r_j, \tag{3.1}$$

where σ^{RR} is the direct (radiative) recombination cross section and σ^j_{cap} is the resonant capture cross section to an autoionizing configuration j. The branching ratio for radiative stabilization is given by

$$B^r_j = \frac{\sum_m A^r(j \to m)}{\sum_m A^r(j \to m) + \sum_n A^a(j \to n)}, \tag{3.2}$$

where A^r is a radiative rate and A^a is an autoionization rate.

The configuration average expressions for the above rates and cross sections have been derived in [184] for direct (radiative) recombination. A general transition between configurations has the form

$$(n\ell)^{q-1} k_i \ell_i \to (n\ell)^q, \tag{3.3}$$

50

and the recombination cross section is given by

$$\sigma^{RR} = \frac{16\pi^2\omega^3}{3k_i^3c^3}(4\ell + 3 - q)\frac{2\ell_>}{(4\ell + 2)(4\ell_i + 2)}|D(k_i\ell_i \rightarrow n\ell)|^2, \tag{3.4}$$

where $\omega = \frac{1}{2}k_i^2 - \epsilon_{n\ell}$, c is the speed of light in vacuum, and $\ell_>$ is the greater value between ℓ and ℓ_i. The radial dipole integral, D, can be calculated as

$$D(k_i\ell_i \rightarrow n\ell) = \int_0^\infty P_{n_i\ell_i}(r)rP_{n\ell}(r)dr. \tag{3.5}$$

For electron-impact capture to autoionizing configurations, a general transition between configurations may have the form

$$(n_1\ell_1)^{q_1+1}(n_2\ell_2)^{q_2-1}(n_3\ell_3)^{q_3-1}k_i\ell_i \rightarrow (n_1\ell_1)^{q_1}(n_2\ell_2)^{q_2}(n_3\ell_3)^{q_3}, \tag{3.6}$$

and the resonant capture cross section is given by

$$\sigma_{cap} = \frac{2\pi^2}{k_i^3c^3\Delta\epsilon}(q_1 + 1)(4\ell_2 + 3 - q_2)(4\ell_3 + 3 - q_3)$$

$$\times \sum_{\ell_i}(2\ell_i + 1)|M(n_1\ell_1, k_i\ell_i \rightarrow n_2\ell_2, n_3\ell_3)|^2. \tag{3.7}$$

In the capture cross section expressions, $n_1\ell_1$, $n_2\ell_2$, and $n_3\ell_3$ are quantum numbers of the bound electrons, $k_i\ell_i$ are quantum numbers for the initial continuum electrons, $\Delta\epsilon$ is an energy width larger than the largest resonance width, which provides a width that is used to bin the cross section results, and $M(n_1\ell_1, k_i\ell_i \rightarrow n_2\ell_2, n_3\ell_3)$ is the scattering matrix, which is a sum over products of standard angular factors and radial direct and exchange electrostatic integrals. For the generation of Maxwellian rate coefficients, the width of the Maxwellian distribution is much greater than the resonance width; thus, it is sufficient to

51

choose a $\Delta\epsilon$ that is larger than the largest resonance width. For the calculations shown here a $\Delta\epsilon$ of 0.005 eV was used.

The energies and bound orbitals needed to evaluate all the configuration-average cross sections and rates appearing in Eqs. (3.1, and 3.2) are calculated in the Hartree-Fock relativistic (HFR) approximation [154], which includes the mass-velocity and Darwin corrections with modified HF differential equations. The continuum radial orbitals, with normalization chosen as one times a sine function as $r \to \infty$, are obtained by solving a single-channel radial Schrödinger equation, which also includes the mass-velocity and Darwin corrections, where the distorting potential is constructed from HFR bound orbitals.

The Maxwellian-averaged DR rate coefficient, $\alpha^{DR}(T)$, can be calculated as follows

$$\alpha^{DR}(T) = \langle v\sigma^{DR} \rangle = \int_0^\infty v(E)\, \sigma^{DR}(E)\, f_{MB}(E, k_B T)\, dE, \qquad (3.8)$$

with $f_{MB}(E, k_B T)$ as the Maxwell-Boltzmann distribution is given in Eq. (2.74).

3.3   Dielectronic Recombination for M-Shell Ions
3.3.1   Dielectronic Recombination for Ar^{7+}

The DR process for $\Delta n_c = 0$ core excitations of Na-like Ar^{7+} occurs via the intermediate autoionizing configurations

$$Ar^{7+}(3s) + e^- \to Ar^{6+}(3pn\ell)$$
$$\to Ar^{6+}(3dn\ell), \qquad (3.9)$$
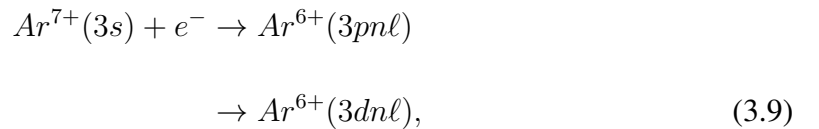
where n and ℓ are included explicitly up to $n = 10$ and $\ell = 7$, and extrapolations are used to include contributions up to $n = 1000$ and $\ell = 12$.

52
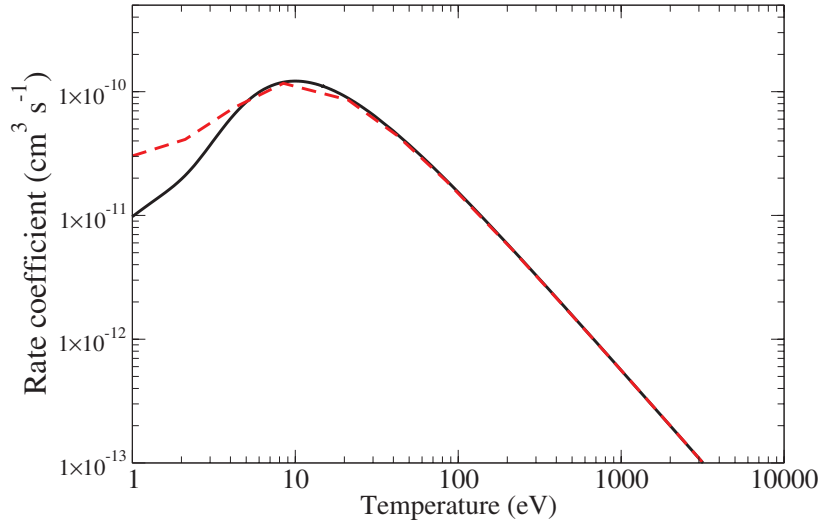
Figure 3.1 Dielectronic recombination rate coefficients for Ar^{7+}: black solid curve, our configuration-average distorted-wave results; red dashed curve, level-resolved distorted-wave [101].

We compare our configuration-average distorted-wave rate coefficients with level-resolved distorted-wave calculations [101] in Fig. 3.1. At low temperatures, there is a large disagreement between the configuration-average and level-resolved distorted-wave calculations. This is due to the fact that the average energy for the $3d4f$ configuration is bound in the configuration-average case, whereas some of the energy levels of this configuration are actually autoionizing. A few levels just above the ionization limit can have a large effect on the recombination rate for low temperatures. On the other hand, there is very good agreement between the configuration-average and level-resolved distorted-wave calculations at high temperatures. For plasmas dominated by electron ionization, the Ar^{7+} ion stage balance is mainly determined by the values of the recombination rate coefficients above 20 eV (see Fig. 3.4). The comparison between our configuration-average distorted-wave results and the level-resolved distorted-wave results gives us increased confidence in the configuration average results for the lower ionization stages. The results for the lower ionization

53

stages also provide an indication of the most important recombining channels, to guide future level-resolved calculations.

3.3.2 Dielectronic Recombination for Ar^{6+}
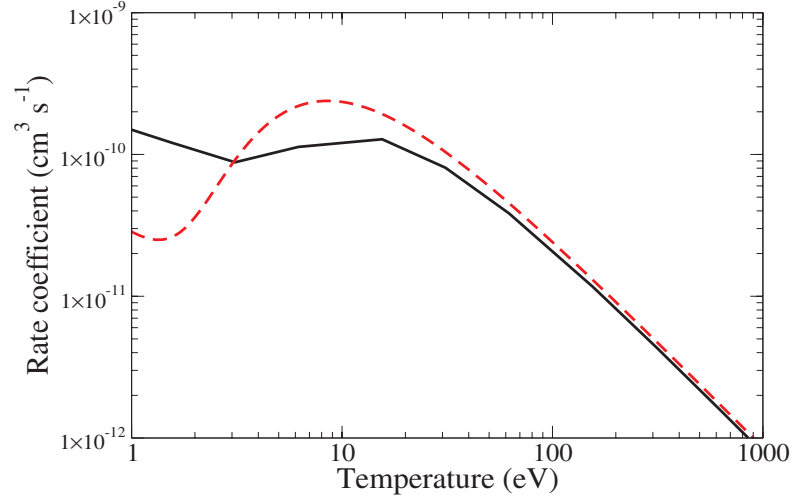
Figure 3.2 Dielectronic recombination rate coefficients for Ar^{6+}: black solid curve, our configuration-average distorted-wave results; red dashed curve, level-resolved distorted-wave [102].

The DR process for $\Delta n_c = 0$ core excitations of Mg-like Ar^{6+} occurs via the intermediate autoionizing configurations

$$Ar^{6+}(3s^2) + e^- \to Ar^{5+}(3s3pn\ell)$$

$$\to Ar^{5+}(3s3dn\ell), \tag{3.10}$$
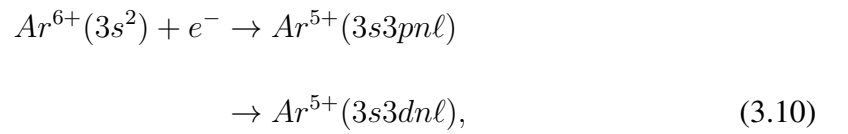
where we have used the same values for n and ℓ as we did in the Ar^{7+} cases. We compare our configuration-average distorted-wave rate coefficient with level-resolved distorted-wave results [102] in Fig. 3.2. The large differences at low temperatures are due to differences in the near threshold resonances in the two calculations. The small differences

at high temperatures are due to term splitting of the core-excited energies of the $3s3p$ and $3s3d$ excited configurations, which are not accounted for in the configuration-average calculations. Plasmas dominated by electron collisions for the Ar^{6+} ion stage balance are mainly determined by the values of the recombination rate coefficients above 10 eV (see Fig. 3.4).

3.3.3 Dielectronic Recombination for $Ar^+ - Ar^{5+}$

The DR process, for $\Delta n_c = 0$ core excitations, of $Ar^+ - Ar^{5+}$ occurs via the intermediate autoionizing configurations:

$$Ar^{(6-m)+}(3s^2 3p^m) + e^- \rightarrow Ar^{(5-m)+}(3s^2 3p^{m-1} 3dn\ell)$$

$$\rightarrow Ar^{(5-m)+}(3s3p^{m+1} n\ell)$$

$$\rightarrow Ar^{(5-m)+}(3s3p^m 3dn\ell), \qquad (3.11)$$

where $1 \leq m \leq 5$ and we have used the same values for n and ℓ as we did in the Ar^{7+} and Ar^{6+} cases. The magnitudes of the $3s \rightarrow 3d$ excitations were found to be much smaller than the $3p \rightarrow 3d$ excitations at the temperatures relevant for plasmas dominated by electron collisions and, therefore, were not included in our total recombination rate coefficients. Higher $\Delta n_c = 1$ excitations were not considered, since they were also found to be very small compared to $\Delta n_c = 0$ excitations in recent level-resolved distorted-wave calculations for Al-like Fe^{13+} [104]. We present our configuration-average distorted-wave rate coefficients for Ar^+ - Ar^{5+} in Fig. 3.3. There are no quantum mechanically derived rate coefficients to compare with for these ion stages. Hence, we extended our configuration-average distorted-wave calculations to Ar^{6+} and Ar^{7+} to provide a comparison of our method with previously

published level-resolved distorted-wave calculations.
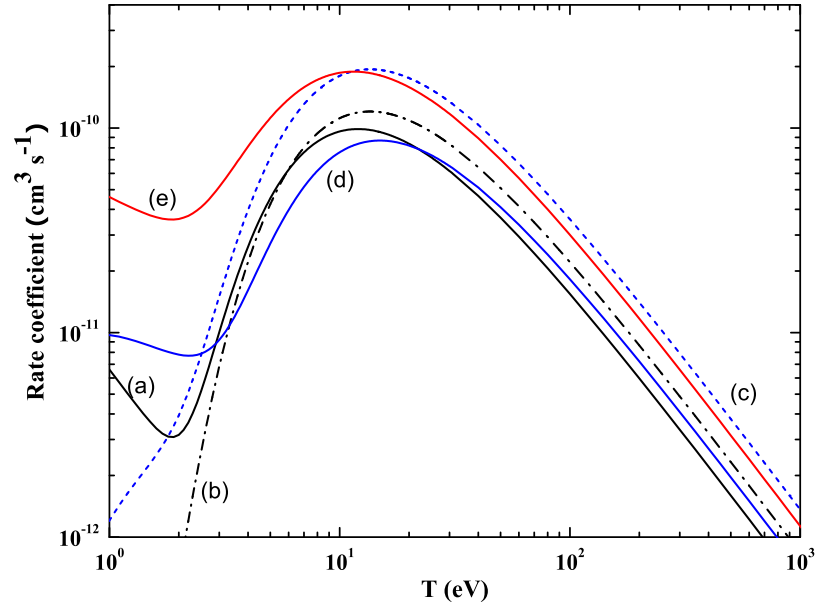
Figure 3.3   Dielectronic recombination rate coefficients for M-shell argon ions (Ar^+ - Ar^{5+}): (a) black solid curve, DR data for Ar^+; (b) black dash-dotted curve, for Ar^{2+}; (c) blue dashed curve, for Ar^{3+}; (d) blue solid curve, for Ar^{4+}; and (e) red solid curve, Ar^{5+}.
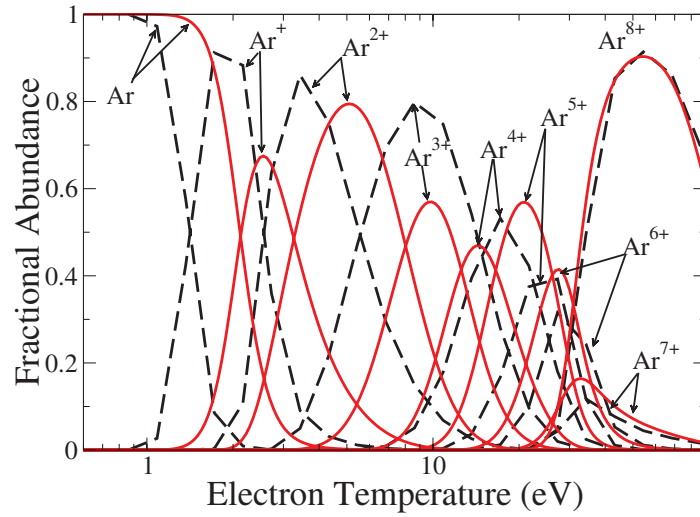
Figure 3.4   Equilibrium ion-stage balance for Ar- Ar^{8+}: red solid curves, our configuration-average distorted-wave atomic data; dashed line curves, older atomic data of Mazzotta *et al.* [123].

Our new DR rate coefficients data for the M-shell argon ions were used in a study to determine the fractional abundances of Argon in a study by Loch *et al.* [185]. The ionization balance equations based on the available electron impact ionization and our recombination data were solved in the case of equilibrium balance and taking into account ionization from metastable and excited states. The fractional abundances for Ar - Ar^{8+} as a function of electron temperatures are shown in Fig. 3.4. A comparison with the tabulated fractional abundances of Mazzotta *et al.* [123] is seen. Although both data show similar results for Ar^{8+}, the position and height are shifted for the rest of the argon ions. The difference in the fractional abundances for Ar^{2+} - Ar^{5+} are due to the DR data of Mazzotta *et al.* [123] being taken from different sources, including the general formula of Burgess [4]. The fractional abundances for Ar - Ar^{8+} from Byrans *et al.* [115] are similar to the results of Mazzotta *et al.* [123], because they used the same data for these ions.

In summary, Electron impact DR rate coefficients for Ar^{+}- Ar^{7+} were calculated using a configuration-average distorted-wave approximation. Good agreements have been obtained with the level-resolved distorted-wave rate coefficients for Ar^{6+} and Ar^{7+} for electron temperatures above 10 eV, where these ions are abundant. The difference in the fractional abundances for argon ions at the lower ion stages can be attributed to the difference in the DR rate coefficients data.

CHAPTER IV

DIELECTRONIC RECOMBINATION FOR ALUMINUM-LIKE IONS

4.1 Introduction

There has been little theoretical DR work performed in the past for M-shell systems with open p- and d-shells, thus systematic calculations for these systems are required to remove the uncertainty in ionization balance predictions, which comes from the poor DR data used. Here, we focus on study of the Al-like isoelectronic sequence. The available DR data for Al-like ions [84, 123, 127, 128, 129, 130] are either semi-empirical fits or from calculations performed within a non-relativistic *LS*-coupling approximation. These data are appropriate for the high temperatures characteristic of electron-ionized gas, but not for the low temperatures characteristic of photoionized gas. I have carried out semi-relativistic calculations for DR cross sections and rate coefficients of the Al-like isoelectronic sequence using the level-resolved distorted-wave AUTOSTRUCTURE program [32, 186]. The results for Fe^{13+} are tested against the available measurements from the Heidelberg heavy-ion Test Storage Ring facility [76]. My calculations include final-state-resolved partial DR and RR rate coefficients from the initial ground and metastable levels spanning a temperature range of $q^2(10 - 10^7)$K, where q is the initial ionic charge. Finally, I have fitted my computed Maxwellian-averaged DR rate coefficients with a simple formula for efficient dissemination of data and ease of use in plasma modeling codes.

The rest of this Chapter is organized as follows. In Sec. 4.2, a summary of available RR and DR formulas and fitting data for Al-like ions is presented. In 4.3, the methodology is

presented and the results for the entire Al-like isoelectronic sequence are discussed in Sec. 4.4.

4.2 Available Fitting Formulas for DR and RR Rate Coefficients

Most of the available DR data for the Al-like sequence are from compilations obtained using fitting formulas. In 1965, Burgess introduced a fitting formula [4], which is given by

$$\alpha^{DR} = \frac{3.0 \times 10^{-12} B(q)}{t^{3/2}} \sum_j f(j,i) \, A(x) \, \exp\left(-\frac{E}{k_B T}\right), \tag{4.1}$$

where $f(j,i)$ is the oscillator strength of the recombining ion from state i to state j, t is the electron temperature in units of 10^6 K, q is the charge of the recombining ion, $A(x)$ and $B(q)$ are given by

$$A(x) = \frac{\sqrt{x}}{(1 + 0.105x + 0.015x^2)}, \quad x > 0.05, \quad x = \frac{q+1}{\epsilon_{ij}}$$

$$B(q) = \sqrt{\frac{q(q+1)}{q^2 + 13.4}} \, (q+1)^2, \quad q \leq 20,$$

$$\frac{E}{k_B T} = \frac{0.158(q+1)^2 \epsilon_{ij}}{at}, \quad \epsilon_{ij} = \frac{1}{\nu_i^2} - \frac{1}{\nu_j^2}$$

$$a = 1 + \frac{0.015q^3}{(q+1)^2}, \quad \frac{E}{k_B T} \leq 5.0, \tag{4.2}$$

with ν_i and ν_j are the effective quantum numbers of state i and j, respectively.

In 1973, Aldrovandi and Péquignot introduced a two-parameter fitting formula for calculating RR rate coefficients and a four-parameter fitting formula for calculating DR rate coefficients for the recombined ion ($N + 1$-electron system) [84]. They used hydrogenic approximations for all excited states in the recombined ion in their radiative calculations

59

[187]. Their fitting formulas are given by

$$\alpha^{RR}(T) = A_{rad}\left(\frac{T}{10^4}\right)^{-\eta},$$

$$\alpha^{DR}(T) = \frac{A_{di}}{T^{3/2}}\exp\left(-\frac{T_0}{T}\right)\left[1 + B_{di}\exp\left(-\frac{T_1}{T}\right)\right], \qquad (4.3)$$

where T is in Kelvin and the rates are in cm^3 s^{-1}.

In 1980, Mewe *et al.* introduced an empirical formulas for calculating RR and DR rate coefficients [85]. Their formulas are given in Eq. (4.4) and their fitting coefficients are presented in Table 4.1.

$$\alpha^{RR} = \frac{\alpha\,q^{2\eta+1-\Delta}}{10^{10}\,T^\eta},$$

$$\alpha^{DR} = \frac{\sum_{i=1}^{2}\alpha_i\,q^{\beta_i}}{10^3\,T^{3/2}\,\sqrt{q^2 + 13.4}}\,\exp\left(-\frac{10^4\gamma_i q^{\delta_i}}{T}\right), \qquad (4.4)$$

where q is the initial charge of the target ions.

Table 4.1 RR and DR fitting coefficients for the Al-like isoelectronic sequence given by Mewe *et al.* [85].

	RR			DR							
$Z-q$	α	η	Δ	α_1	β_1	γ_1	δ_1	α_2	β_2	γ_2	δ_2
13	1.67	0.75	0.0	0.07	4.05	$1.6(z+1)^2$	-0.14	6.1	2.45	4.8	0.86

In 1982, Shull and Steenberg presented calculations for ionization equilibrium of 11 abundant elements (C, N, O, Ne, Mg, Si, S, Ar, Ca, Fe, and Ni) [86]. Their fitting coefficients for RR and DR rate coefficients for the Al-like ions are given in Table 4.2 for the recombining ion (N-electron system). They took their RR fitting coefficients (A_{rad} and η) from the tabulations of Aldrovandi and Péquignot [84] for Si and S and from Woods *et al.* [188] for Fe. The values for Ar, Ca, and Ni were obtained by interpolation along

60

Table 4.2 Available RR and DR fitting coefficients for the Al-like isoelectronic sequence. Numbers in parentheses are powers of 10.

ion	A_{rad} cm^3 s^{-1}	η	A_{di} cm^3 s^{-1} $K^{3/2}$	B_{di}	T_0 K	T_1 K	Ref.
Si^+	5.900(-13)	6.010(-1)	6.200(-3)	0	1.100(5)	0	a
	5.900(-13)	6.010(-1)	1.100(-3)	0	7.700(4)	0	b
P^{2+}	1.294(-12)	6.766(-1)	7.641(-3)	6.005(-2)	1.284(5)	1.109(5)	c
S^{3+}	2.700(-12)	7.450(-1)	9.100(-3)	6.000	1.300(5)	1.500(5)	a
	2.700(-12)	7.450(-1)	3.350(-2)	6.590(-2)	1.890(5)	1.590(5)	b
Cl^{4+}	5.165(-12)	7.893(-1)	6.844(-2)	7.232(-2)	2.275(5)	2.280(5)	c
Ar^{5+}	9.120(-12)	8.110(-1)	9.000(-2)	7.690(-2)	2.500(5)	3.300(5)	b
K^{6+}	1.513(-11)	8.186(-1)	1.126(-1)	7.902(-2)	2.830(5)	4.832(5)	c
Ca^{7+}	2.400(-11)	8.200(-1)	1.390(-1)	8.780(-2)	3.220(5)	6.990(5)	b
Ti^{9+}	5.518(-11)	8.245(-1)	1.818(-1)	1.777(-1)	3.679(5)	1.282(6)	c
Cr^{11+}	1.123(-10)	8.313(-1)	2.130(-1)	4.267(-1)	3.846(5)	1.816(6)	c
Mn^{12+}	1.525(-10)	8.342(-1)	2.320(-1)	5.655(-1)	3.967(5)	1.908(6)	c
Fe^{13+}	2.000(-10)	8.360(-1)	2.600(-1)	6.000(-1)	4.210(5)	1.820(6)	b
Co^{14+}	2.537(-10)	8.364(-1)	3.036(-1)	4.860(-1)	4.644(5)	1.574(6)	c
Ni^{15+}	3.160(-10)	8.360(-1)	3.630(-1)	3.370(-1)	5.240(5)	1.290(6)	b

a Aldrovandi and Péquignot [84].

b Shull and Steenberg [86].

c Landini and Fossi [89].

the sequence. Their DR fitting coefficients (A_{di}, B_{di}, T_0, and T_1) were determined by a least-squares procedure from the rates of Refs. [127, 189, 190] for Si, S, Ca, and Ni. The DR fitting coefficients for Fe were taken from Woods *et al.* [188] that were fits to the calculations of Ref. [191]. DR rates for Ar were interpolated between S and Ca [127, 190]. One can obtain their RR and DR rate coefficients for the Al-like ions using their fitting coefficients from Table 4.2 and using Eq. (4.3).

In 1990, Landini and Fossi [88] calculated the ionization balance for the ions H, He, C, O, N, Ne, Na, Mg, Al, Si, S, Ar, Ca, Fe, and Ni for temperatures ranging from 10^4 to 10^8 K based on the fitting coefficients for RR and DR rates given by Shull and Steenberg [86]. They also computed the ionization equilibrium for some cosmically less abundant elements (F, P, Cl, K, Ti, Cr, Mn, and Co), where they extrapolated the data given by Shull and Steenberg [86] to obtain the RR and DR rate coefficients for these ions and presented their fitting coefficients in Ref. [89].

In 1998, Mazzotta *et al.* [123] calculated the ionization equilibrium for all the elements from H to Ni where they took the available ionization, RR, and DR rate coefficients in the literature. We have to emphasize that they did not perform any DR calculations for these ions, but they provided DR fitting coefficients based on the available DR calculations for some of these ions or from the Burgess general formula [4]. Moreover, for the Al-like isoelectronic, it is not clear from which source Mazzotta *et al.* obtained their DR data or how these rates were determined. The Al-like DR rate coefficients of Mazzotta *et al.* [123] can be reproduced by using their fitting coefficients from Table 4.3 and using Eq. (4.5)

$$\alpha^{DR}(T) = \frac{1}{T^{3/2}} \sum_j c_j \exp\left(-\frac{E_j}{T}\right),$$ (4.5)

where T and E_i are given in eV, c_i in cm^3 s^{-1} eV$^{3/2}$, and $\alpha^{DR}(T)$ in cm^3 s^{-1}.

In 2002, Mazzitelli and Mattioli [192] calculated the ionization equilibria for Cu, Zn, Ga and Ge ions where the Burgess general formula [4] was used to calculate the DR rate coefficients and summed over $\Delta n_c = 0$ and $\Delta n_c = 1$ transitions in the target. Since there are no DR data available beyond Ni ions, for each sequence they produced their data by

extrapolation. In Table 4.3, their RR and DR fitting coefficients are presented. Their RR rate coefficients can be reproduced by using the first equation in Eq. (4.3) whereas their DR rate coefficients can be reproduced by using Eq. (4.5).

Table 4.3   RR and DR fitting coefficients for the Al-like ions. A_{rad} (cm^3 s^{-1}), c_i (cm^3 s^{-1} eV$^{3/2}$), and E_i (eV). Numbers in parentheses are powers of 10.

Ion	A_{rad}	η	c_1	c_2	c_3	E_1	E_2	E_3	Ref.
Si$^+$	$\cdots$	$\cdots$	0.4898(-11)	0.6080(-9)	$\cdots$	2.050	9.680	$\cdots$	a
P^{2+}	$\cdots$	$\cdots$	0.6359(-8)	$\cdots$	$\cdots$	11.200	$\cdots$	$\cdots$	a
S^{3+}	$\cdots$	$\cdots$	0.1817(-7)	0.5920(-10)	$\cdots$	16.620	2.400	$\cdots$	a
Cl^{4+}	$\cdots$	$\cdots$	0.5708(-7)	$\cdots$	$\cdots$	19.890	$\cdots$	$\cdots$	a
Ar^{5+}	$\cdots$	$\cdots$	0.7557(-7)	$\cdots$	$\cdots$	22.020	$\cdots$	$\cdots$	a
K^{6+}	$\cdots$	$\cdots$	0.9296(-7)	$\cdots$	$\cdots$	24.730	$\cdots$	$\cdots$	a
Ca^{7+}	$\cdots$	$\cdots$	0.1149(-6)	$\cdots$	$\cdots$	28.160	$\cdots$	$\cdots$	a
Sc^{8+}	$\cdots$	$\cdots$	0.1247(-6)	$\cdots$	$\cdots$	27.700	$\cdots$	$\cdots$	a
Ti^{9+}	$\cdots$	$\cdots$	0.2584(-7)	0.1454(-6)	$\cdots$	142.170	31.700	$\cdots$	a
V^{10+}	$\cdots$	$\cdots$	0.1687(-6)	$\cdots$	$\cdots$	32.990	$\cdots$	$\cdots$	a
Cr^{11+}	$\cdots$	$\cdots$	0.7270(-7)	0.1704(-6)	$\cdots$	189.630	33.140	$\cdots$	a
Mn^{12+}	$\cdots$	$\cdots$	0.1049(-6)	0.1856(-6)	$\cdots$	198.600	34.180	$\cdots$	a
Fe^{13+}	$\cdots$	$\cdots$	0.2081(-6)	0.1281(-6)	$\cdots$	36.300	193.000	$\cdots$	a
Co^{14+}	$\cdots$	$\cdots$	0.2429(-6)	0.1180(-6)	$\cdots$	40.020	175.650	$\cdots$	a
Ni^{15+}	$\cdots$	$\cdots$	0.9885(-7)	0.2904(-6)	$\cdots$	156.310	45.150	$\cdots$	a
Cu^{16+}	3.780(-10)	0.833	1.560(-7)	1.660(-7)	0.877(-7)	42.880	56.080	247.400	b
Zn^{17+}	4.410(-10)	0.835	1.710(-7)	1.690(-7)	1.020(-7)	44.808	58.658	260.700	b

a Mazzotta *et al.* [123].

b Mazzitelli and Mattioli [192].

4.3   Methodology

We use the-state-of-the-art AUTOSTRUCTURE [32, 186] to carry out a series of multi-configuration Breit-Pauli (MCBP) calculations for DR cross sections and rate coefficients for the Al-like isoelectronic sequence in the independent-processes, isolated-resonances distorted-wave (IPIRDW) approach. Interference between RR and DR is very small even

for ions with small degree of ionization q [98, 172]. So, it can be neglected and treat RR and DR processes separately. AUTOSTRUCTURE is based on lowest-order perturbation theory, where electron-electron and electron-photon interactions are treated to the first order. Nonorthogognal radial functions are determined using the STO model potential [166] as described in Sec. 2.2.4. The radial scaling parameters $\lambda_{3\ell}$ for $(3s, 3p, \text{and } 3d)$ are determined by minimizing the equally weighted sum of energies of the lowest energy levels, with a closed neon core. Configuration mixing is taken into account for describing target wave functions as discussed in Sec. 2.2.5. Instead of extrapolating the rates by $1/n^3$ method, we follow a more accurate technique, in which bound orbitals are approximated by a normalized zero-energy continuum orbital for $n > 15 + \ell^2/4$ using a quantum defect approximation as in Eq. (2.41). For each $n\ell$, diagonalizations for N and $(N + 1)$-electron-Hamiltonians are performed and followed by calculations for autoionization and radaitive rates A^a and A^r, respectively as discussed in Sec. 2.5. Rate coefficients are then calculated by using a post-processor ADASDR, in which radiative transition between highly excited Rydberg states are computed hydrogenically.

Finally, DR rate coefficients are fitted using the form:

$$\alpha^{DR}(T) = T^{-3/2} \sum_i c_i \, \exp\left(-\frac{E_i}{T}\right), \tag{4.6}$$

where E_i are in units of temperature T (eV or K), and the units of c_i are then cm^3 s^{-1}[eV or K]$^{3/2}$.

The RR rate coefficients are fitted using the formula of Verner and Ferland [193]

$$\alpha^{RR}(T) = \frac{A\sqrt{T_0/T}}{[1 + \sqrt{T/T_0}]^{1-B} \, [1 + \sqrt{T/T_1}]^{1+B}}, \tag{4.7}$$

where A has units of cm^3 s^{-1}, T_0 and T_1 are in units of temperature (eV or K). The fitting coefficient B is unitless. A more accurate representation, especially for low-charge ions, replaces B as [110]

$$B \longrightarrow B + C \, \exp\left(-\frac{T_2}{T}\right). \tag{4.8}$$

4.4   DR for the Aluminum-Like Isoelectronic Sequence
4.4.1   Aluminum-Like Sulfur

In 1979, Jacobs *et al.* calculated total DR rate coefficients for sulfur ions with application to a magnetic fusion plasma [127]. They assumed that the recombination could take place through a limited number of electron transitions with an electron density of 10^{10} cm^{-3}. Moreover, they neglected the non-dipole autoionizing transitions and used a single-configuration approximation to evaluate energies and transition rates. Such approximations are not valid for low charged ions. In 1991, Badnell [128] calculated total DR rate coefficients for S^{q+} ($q = 1 - 5$) ions in the low-density limit, but these calculations were performed within *LS*-coupling and were limited to the temperature range $T = 3 \times 10^4 - 10^6$K as an application to the Io plasma torus. In 1992, Al-Mulhem and Nasser presented DR cross sections and rate coefficients for S^{3+} [129]. Their calculations were also done in *LS*-coupling and only considered $3s \rightarrow 3p$ excitation using single-configuration and relativistic Hartree-Fock wave functions. The disadvantage of their calculation is that they didn't include the other important $3p \rightarrow 3d$ and $3s \rightarrow 3d$ excitations and the subsequent Auger channels that can contribute to the DR cross sections and rate coefficients. In 1995,

65

Nahar and Pradhan [44] presented total rate coefficients for silicon and sulfur ions (RR + DR) applying a new unified treatment they developed for electron-ion recombination based on the close coupling R-matrix method. In the same year, Nahar published the data for S^{3+} along with other ions [194]. In 1996, a correction was made due to a numerical error in the step size of the integration that affected the total rate coefficient in the low-temperature region [195]. In 2000, Nahar calculated the total rate coefficients and photoionization cross sections for the Al-like isoelectronic sequence for the astrophysically abundant elements Si^+, S^{3+}, Ar^{5+}, Ca^{7+}, and Fe^{13+} [130]. All these calculations were performed in the *LS*-coupling approximation. We have to keep in mind that they are studying the photorecombination process and their target is the $(N + 1)$-electron system which is the the opposite of the DR process (our target is the recombining ion and has N electrons).

Given the available earlier results, calculations of DR cross sections and rate coefficients for S^{3+} are a good starting point for the Al-like sequence. The goal is to perform these calculations not only in *LS*-coupling but also in IC-coupling scheme and to study the low-energy DR rate coefficients. Two separate calculations were done for both cross sections and rate coefficients for S^{3+}. In the first calculation, I used the same target basis (N-electrons) as Badnell did [128], which I call basis A. In the second calculation, a larger basis B was used to describe the target since this basis was used in the study for Fe^{13+} [104]. Both bases are described in Table 4.4.

Note that configurations 1, 2, 3, and 5 form the minimal set which allows for all ($\Delta n_c = 0$) one-electron promotions during the DR capture process. Basis A gives rise to 30 target terms (68 levels) while basis B gives rise to 56 target terms (129 levels). The radial wave

Table 4.4   Bases used to calculate Al-like DR cross sections and rate coefficients. A neon core was assumed for all these configurations and omitted for simplicity.

Basis	Configuration					
A	1- $3s^23p$,	2- $3s3p^2$,	3- $3s^23d$,	4- $3p^3$,	5- $3s3p3d$,	and 6- $3p^23d$
B	Basis A,	7- $3s3d^2$,	and 8- $3p3d^2$			

functions were obtained by using the STO model potential [166] as decribed in Sec. 2.2.4.

The $3s$, $3p$, and $3d$ radial scaling parameters, $\lambda_{n\ell}$, were determined by minimizing the

equally-weighted-sum of energies of the lowest 18 levels. The radial scaling parameters

for basis A are $\lambda_{3s} = 1.18199$, $\lambda_{3p} = 1.25917$, and $\lambda_{3d} = 0.98662$, and $\lambda_{3s} = 1.18372$,

$\lambda_{3p} = 1.24942$, and $\lambda_{3d} = 0.98197$ for basis B.

In Table 4.5, a comparison of the lowest calculated 10 energy levels (in Rydbergs) with

other available data is presented. We see that the energy levels for basis B are closer to

the observed values [196, 197] or the recent MCHF calculations by Froese-Fischer *et al.*

[198]. The data given by Bhatia *et al.* [199], using the SUPERSTRUCTURE program by

Eissner *et al.* [141], do not describe the target very well because they used only $3s^23p$,

$3s3p^2$, and $3s^23d$ configurations. An extensive structure calculation including more target

bases with correlations up to $n = 6$ was carried out by Tayal [200], where he used the

CIV3 program by Hibbert [203]. Data by Gupta and Msezane were obtained by including

correlations up to $n = 5$ [201]. Hibbert *et al.* included up to $n = 7$ in their target bases

and used both MCHF and CIV3 program packages to calculate the energy levels and the

$3s^23p - 3s3p^2$ transitions for S^{3+} [202]. The biggest energy difference found between my

calculated energy levels using basis B and the observed low-lying level energies was 0.11

Ryd. Resonances attached to the target states were shifted to match the observed energies

Table 4.5   Lowest energy levels (in Rydbergs) for S^{3+} for $\Delta n_c = 0$. A neon core is assumed in all cases and omitted for simplicity.

m	config.	$^{2S+1}L_J^{\pi}$	Basis A[a]	Basis B[b]	NIST[c]	MCHF[d]
1	$3s^23p$	$^2P_{1/2}^o$	0.00000	0.00000	0.00000	0.00000
2		$^2P_{3/2}^o$	0.00712	0.00720	0.00867	0.00773
3	$3s3p^2$	$^4P_{1/2}$	0.63309	0.62918	0.64869	0.63695
4		$^4P_{3/2}$	0.63559	0.63171	0.65181	0.63976
5		$^4P_{5/2}$	0.63964	0.63578	0.65679	0.64418
6		$^2D_{3/2}$	0.85195	0.85341	0.85753	0.85060
7		$^2D_{5/2}$	0.85214	0.85360	0.85796	0.85097
8		$^2S_{1/2}$	1.13910	1.09009	1.12550	1.12630
9		$^2P_{1/2}$	1.17306	1.17880	1.21763	1.23232
10		$^2P_{3/2}$	1.17745	1.18352	1.22333	1.23747

m	config.	$^{2S+1}L_J^{\pi}$	Bhatia et al.[e]	Tayal[f]	Gupta[g]	Hibbert et al. [h]
1	$3s^23p$	$^2P_{1/2}^o$	0.00000	0.00000	0.00000	0.00000
2		$^2P_{3/2}^o$	0.00785	0.00740	0.00086	0.00879
3	$3s3p^2$	$^4P_{1/2}$	0.54500	0.64760	0.65006	0.64479
4		$^4P_{3/2}$	0.54761	0.65180	0.65320	0.64809
5		$^4P_{5/2}$	0.55184	0.65680	0.65816	0.65312
6		$^2D_{3/2}$	0.83056	0.85940	0.85308	0.85900
7		$^2D_{5/2}$	0.83074	0.85780	0.85347	0.85960
8		$^2S_{1/2}$	1.10566	1.12540	1.12798	1.12577
9		$^2P_{1/2}$	1.26981	1.21760	1.22082	1.22673
10		$^2P_{3/2}$	1.27484	1.22340	1.22648	1.23244

[a] present work: Basis A MCBP calculations.

[b] present work: Basis B MCBP calculations.

[c] NIST experimental data by Joelsson *et al.* [196] compiled by Martin *et al.* [197].

[d] MCHF theory calculations of Froese-Fischer *et al.* [198].

[e] results by Bhatia *et al.* [199].

[f] results by Tayal [200].

[g] results by Gupta and Msezane [201].

[h] results by Hibbert *et al.* [202].

to align the Rydberg series correctly.

The $(N+1)$-electron wave functions were described by coupling a continuum or bound

orbital to the target configurations (N-electron system). Then all possible Auger and radiative rates were computed from these configurations and used to determine partial and total DR cross sections. Eq. (4.9) describes the $\Delta n_c = 0$ ($3s \rightarrow 3p, 3s \rightarrow 3d$, and $3p \rightarrow 3d$) DR process for the Al-like isoelectronic sequence.

$$
\begin{array}{c}
e^- + 3s^2 3p[^2P_{1/2}] \rightleftharpoons \\
e^- + 3s^x 3p^y 3d^z \overset{A_a}{\longleftarrow}
\end{array}
\left[\begin{pmatrix} \text{Basis A} \\ \text{Basis B} \end{pmatrix} n\ell \right]^{**} \overset{A_r}{\rightarrow} 3s^a 3p^b 3d^c + h\nu, \tag{4.9}
$$

where $x + y + z = 3$ and $a + b + c = 4$. The doubly excited states formed by capturing the incident electron can either autoionize or radiatively decay to final states to complete the DR process. For the recombined S^{2+} ion, only the $3s^2 3p^2$, $3s3p^3$, $3s^2 3p3d$, and $3p^4$ configurations are completely bound, while some of the levels for the $3s3p^2 3d$ configuration are autoionizing and all other possible configurations in the form $3s^a 3p^b 3d^c$ are autoionizing.

I started by performing DR rate coefficient calculations using both basis A, the one that Badnell used in his study of S^{3+} [128], and the bigger basis B in both *LS* and IC-coupling schemes. Fig. 4.1 shows a comparison between my present *LS* results using both bases A and B and the *LS* results of Badnell. All rate coefficients peak at the same electron temperature of 10.858 eV with values of 16.2×10^{-11}, 15.5×10^{-11}, and 15.5×10^{-11} cm^3 s^{-1} for the Badnell data, basis A results, and basis B results, respectively. As seen from Fig. 4.1, the DR rate coefficients for basis A and basis B are the same except at electron temperatures below 1.0 eV, where the DR rate coefficients of basis A is higher, but both results are 4% lower than those of Badnell using earlier AUTOSTRUCTURE implementations [128] at their peaks. From now on, I will use basis B in the rest of my calculations.
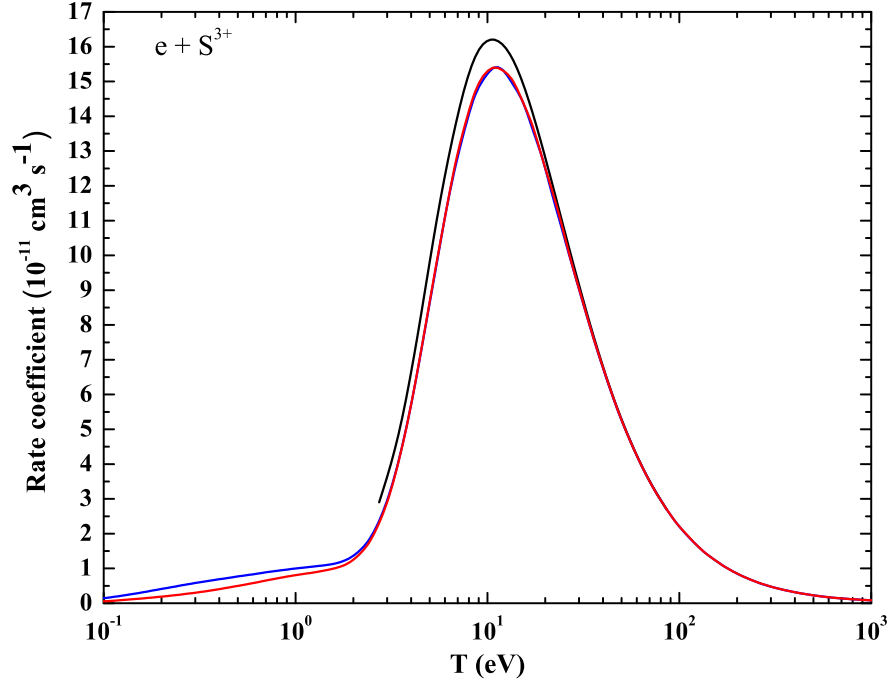
Figure 4.1   Comparison of DR rate coefficients for S^{3+} in *LS*-coupling scheme: black solid curve, DR data of Badnell [128]; blue solid curve, DR rate coefficient using basis A; and red solid curve, DR rate coefficient using basis B.

Next, a comparison between the DR rate coefficients performed in *LS*- and IC-coupling approximations is shown in Fig. 4.2 using basis B. DR rate coefficient in IC-coupling is higher than the one performed in *LS*-coupling at low-electron temperatures below 2.0 eV, due to the doubly excited $3s^23p[^2P_{3/2}]n\ell$ states that can autoionize to the ground state $3s^23p[^2P_{1/2}]$ of S^{3+} [$3s^23p(^2P_{3/2})n\ell \rightarrow 3s^23p(^2P_{1/2}) + e^-$] which does not exist in a non-relativistic *LS* treatment. On the other hand, the DR rate coefficient in IC-coupling is lower at higher electron temperatures ($T > 4.0$ eV). Here, the collisionally ionized zone is as recommended by Bryans *et al.* [204] and the photoionized zones is taken as a private communications from Korista [205].

In order to understand this behavior, we focus on the DR cross section for S^{3+}. In

70
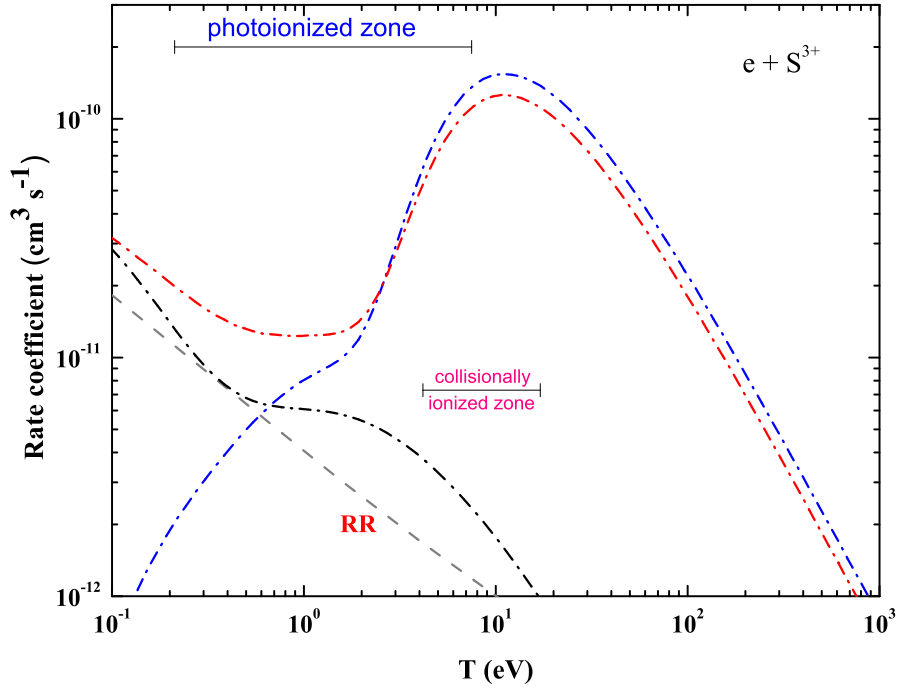
Figure 4.2 Rate coefficients for S^{3+} in both *LS*- and IC-coupling schemes using basis B: blue dash-dotted curve, DR rate coefficient in *LS*-coupling; red dash-dotted curve, DR rate coefficient in IC-coupling; black dash-dotted curve, contribution from $3s^23pn\ell$ series which is forbidden in *LS*-coupling; gray dashed curve, RR rate coefficient. The collisionally ionized zone is as recommended by Bryans *et al.* [204]. The photoionized zone is taken from Ref. [205].

Fig. 4.3, the DR cross section results, in both *LS*- and IC-coupling approximations are shown. These cross sections are convolved with a full width at half maximum (FWHM) Gaussian of 0.1 eV. The DR cross section calculated in IC-coupling at the low-energy region below 0.5 eV is higher than the one calculated in *LS*-coupling. Part of this resonance peaks around 0.054 eV, which is mainly due to the $3s^23p[^2P_{3/2}]n\ell$ resonances which do not exist in an *LS*-coupling scheme and the rest is due to the contribution from the $3s3p^2n\ell$ series (which is allowed in *LS*-coupling). The $3s \rightarrow 3p$ core excitation forms the series $3s3p^2[^4P_J, \,^2D_J, \,^2S_J, \,^2P_J]n\ell$. The series limit of $3s3p^2[^2D_{3/2}]n\ell$ is located at 11.667 eV, while the $3s3p^2[^2P_{1/2}]n\ell$ and $3s3p^2[^2P_{3/2}]n\ell$ series have limits of 16.567 eV

71
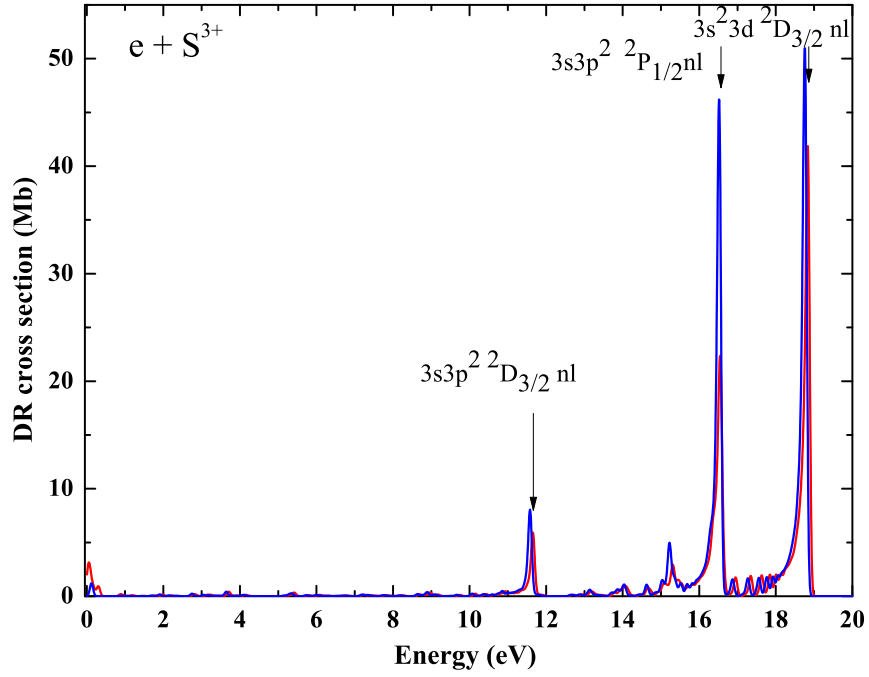
Figure 4.3   DR cross sections for S^{3+} in *LS*- and IC-coupling: blue solid curve, DR cross section in *LS*-coupling; red solid curve, DR cross section in IC-coupling. Both calculations are convolved with FWHM of 0.1 eV using basis B.

and 16.644 eV, respectively. The $3p \rightarrow 3d$ core excitation forms the series $3s^2 3d[^2D_{3/2}]n\ell$ and $3s^2 3d[^2D_{5/2}]n\ell$ with limits of 18.862 and 18.864 eV, respectively. At higher energies, the DR cross section in *LS*-coupling is higher than the cross section in IC-coupling for both $3s \rightarrow 3p$ and $3p \rightarrow 3d$ excitations. In this case, the ground state has a fine structure splitting $[3s^2 3p(^2P_{1/2,\,3/2})]$ of 0.118 eV. Moreover, the DR cross section for $3p \rightarrow 3d$ is higher than the DR cross section for $3s \rightarrow 3p$, which is reflected in the DR rate coefficient.

In an attempt to understand the suppression of the DR cross section in IC-coupling, we focus on the the DR cross section for the $3s \rightarrow 3p$ core excitation in both *LS*- and IC-coupling $[e^- + 3s^2 3p(^2P_{1/2}) \rightleftharpoons 3s 3p^2(^2P_{1/2,\,3/2})n\ell]$. The results for this study are shown in Fig 4.4. All DR cross sections are convolved with a full width at half maximum

72
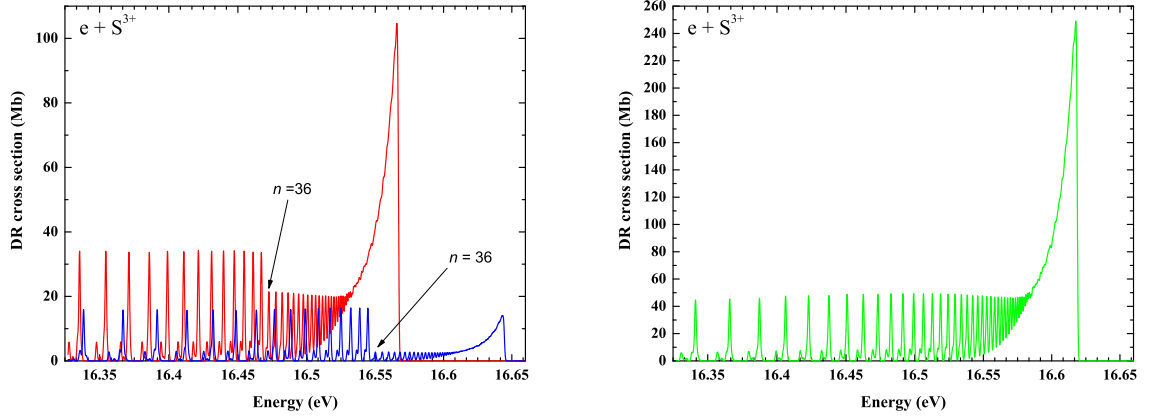
Figure 4.4   DR cross section of S^{3+} for the collision $e^- + 3s^23p(^2P_{1/2}) \rightarrow 3s3p^2(^2P_{1/2,\,3/2})n\ell$ in both *LS*- and IC-coupling schemes: Left panel (IC): DR cross section in IC-coupling, red solid curve, DR cross section for the series $3s3p^2[^2P_{1/2}]n\ell$ and blue solid curve, DR cross section for the series $3s3p^2[^2P_{3/2}]n\ell$. Right panel (LS): same as left panel with green solid curve is the same calculation but in *LS*-coupling approximation. All series are convolved by a FWHM Gaussian of 1.2 meV.

(FWHM) Gaussian of 1.2 meV. As seen, both $3s3p^2[^2P_{1/2,\,3/2}]n\ell$ series exhibit a sudden

drop in the DR cross section at a principal quantum number $n = 36$. Such a reduction does

not exist in the *LS* results. This reduction can be explained as follows. For the $3s \rightarrow 3p$ core

excitation, the doubly excited state $3s3p^2n\ell$ can radiatively decay either to $3s^23p[^2P_{1/2}]n\ell$,

which completes the DR process, or it can radiatively decay to $3s^23p[^2P_{3/2}]n\ell$, which in

turn can autoionize for $n \geq 36$. This reduction in the DR cross section can be represented

as such:

$$e^- + 3s^23p[^2P_{1/2}] \rightleftharpoons 3s3p^2n\ell \rightarrow 3s^23p[^2P_{1/2}]n\ell + h\nu \quad \text{(DR)}$$

$$\downarrow$$

$$3s^23p[^2P_{3/2}]n\ell + h\nu'$$

$$\downarrow$$

$$3s^23p[^2P_{1/2}] + e^- \ (n \geq 36). \tag{4.10}$$

73
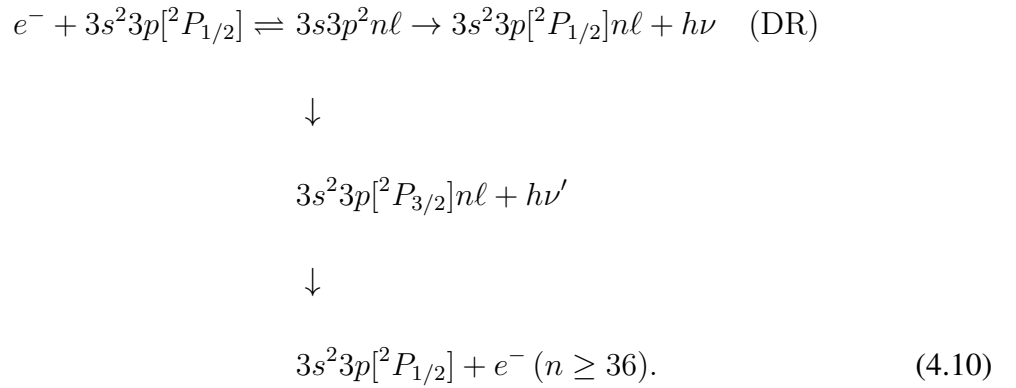
The contribution from the fine structure $3s^2 3p[^2P_{3/2}]n\ell$ series for the collision $[e^- +$ $3s^2 3p(^2P_{1/2}) \rightleftharpoons 3s^2 3p(^2P_{3/2})n\ell]$ for S^{3+} to the DR cross section is presented in Fig. 4.5. All Rydberg states associated with $n < 36$ are bound, while higher Rydberg states are autoionizing. The DR cross section for this collision decreases rapidly with n since the radiative stabilization occurs between two outer electron transitions $n \to n'$ with $n' < 36$.
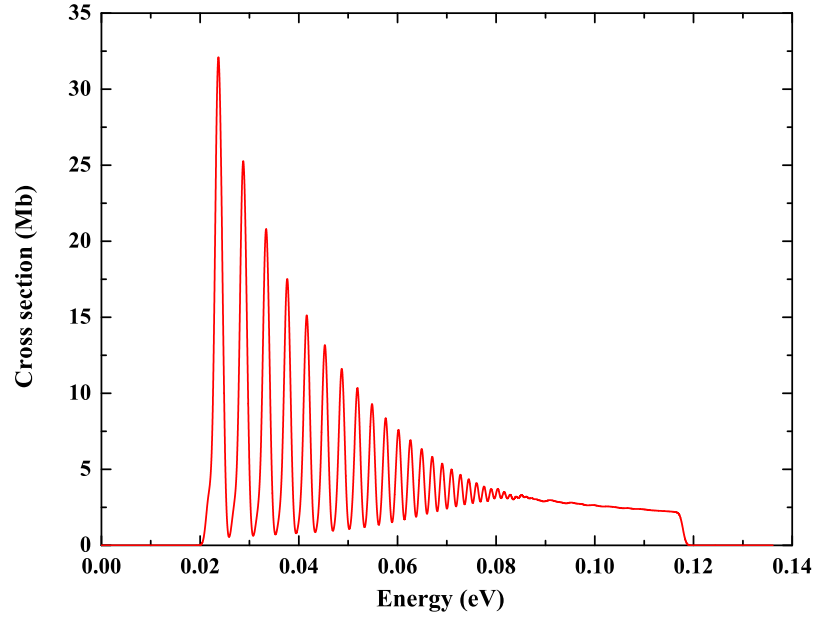
Figure 4.5   DR cross section for the series $3s^2 3p$ $(^2P_{3/2})n\ell$ of S^{3+} in the IC-coupling scheme convolved with FWHM of 1.2 meV.

In the study of the DR cross section for the $3p \to 3d$ core excitation, a similar drop in the DR cross section for both series $3s^2 3d[^2D_{3/2, 5/2}]n\ell$ occurs right at $n = 36$. Fig. 4.6 shows the results for the collision $e^- + 3s^2 3p[^2P_{1/2}] \rightleftharpoons 3s^2 3d[^2D_{3/2}]n\ell$ and this reduction is due to the doubly-excited $3s^2 3dn\ell$ state that can radiatively decay either to $3s^2 3p[^2P_{1/2}]n\ell$, which completes the DR process, or to $3s^2 3p[^2P_{3/2}]n\ell$, which in turn can autoionize for
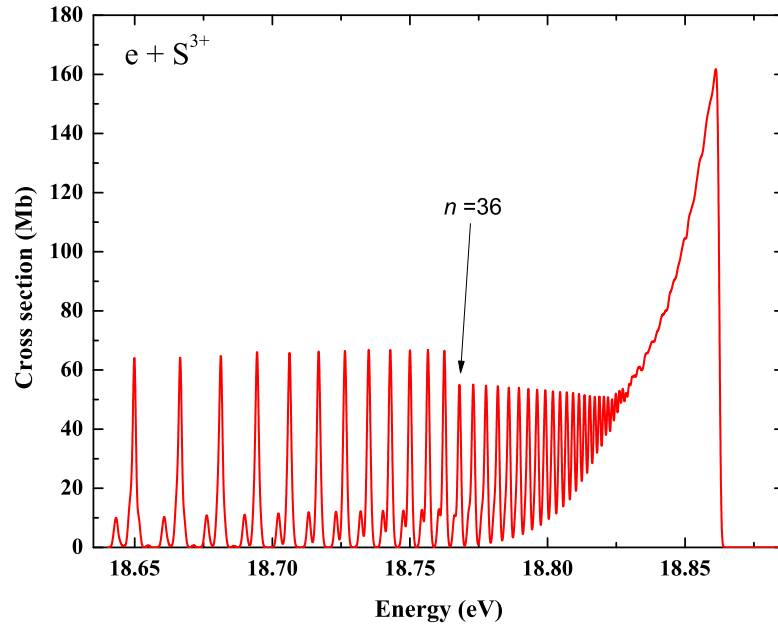
Figure 4.6 DR rate coefficients for S^{3+} for the collision $e^- + 3s^2 3p\ (^2P_{1/2}) \rightarrow 3s^2 3d\ (^2D_{3/2})n\ell$ in IC-coupling convolved with a Gaussian with FWHM of 1.2 meV.

$n \geq 36$. This reduction in the DR cross section can be represented as such:

$$e^- + 3s^2 3p[^2P_{1/2}] \rightleftharpoons 3s^2 3d[^2D_{3/2}]n\ell \rightarrow 3s^2 3p[^2P_{1/2}]n\ell + h\nu \quad (\text{DR})$$

$$\downarrow$$

$$3s^2 3p[^2P_{3/2}]n\ell + h\nu'$$

$$\downarrow$$

$$3s^2 3p[^2P_{1/2}] + e^- (n \geq 36). \tag{4.11}$$

In Fig. 4.7, a schematic diagram for the N- and $(N+1)$-electron systems is shown, which shows the energy levels for each series and how the fine structure series causes the reduction in the DR cross section in IC-coupling.

Since the $3p \rightarrow 3d$ core excitation is the strongest, we choose the $3s^2 3dn\ell$ series to
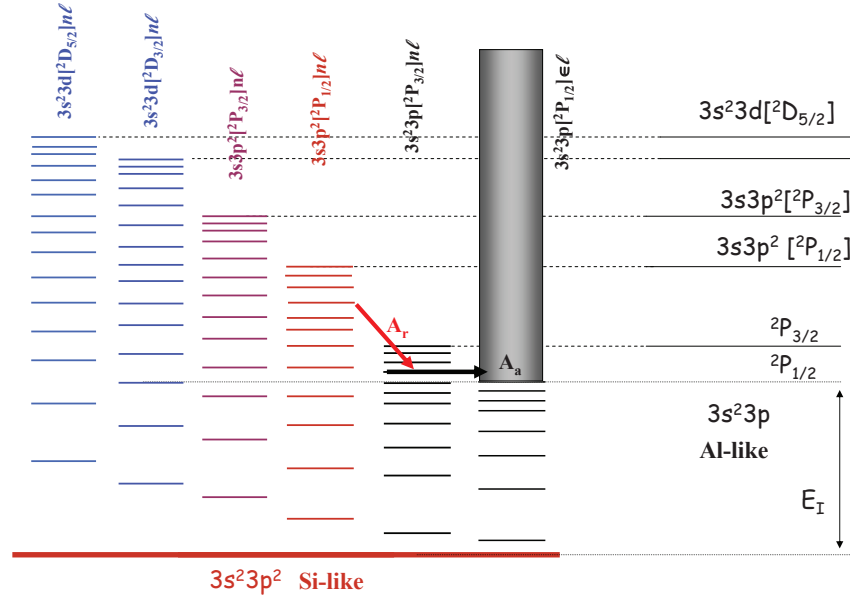
Figure 4.7 Schematic diagram for N-and $(N + 1)$-electron systems with a continuum $\epsilon\ell$ or valance $n\ell$ orbital coupled to Al-like ionic states.

check on the convergence of these calculations for both the angular momentum quantum number ℓ and the principal quantum number n. The convergence for ℓ is shown in Fig. 4.8, where the DR rate coefficient for this series starts to converge at $\ell = 7$. On the other hand, the convergence for n is obtained at $n \geq 200$ (see Fig. 4.9).

Fig. 4.10 shows a comparison of my calculated DR rate coefficients, in both *LS*- and IC-coupling, with other available data of Aldrovandi and Péquignot [84], Mewe *et al* [85], Shull and Steenberg [86], Mazzotta *et al.* [123], Jacobs *et al.* [127], Badnell [128], Al-Mulhem and Nasser [129], and Nahar [130]. As seen, both results of Aldrovandi and Péquignot [84] and Mewe *et al.* [85] differ markedly from the other results. The first one peaks at an electron temperature of 13.0 eV, with a peak 37% higher than my *LS*-coupling results, while the second peaks at 7.0 eV and is 19% higher than my *LS*-coupling results.

76
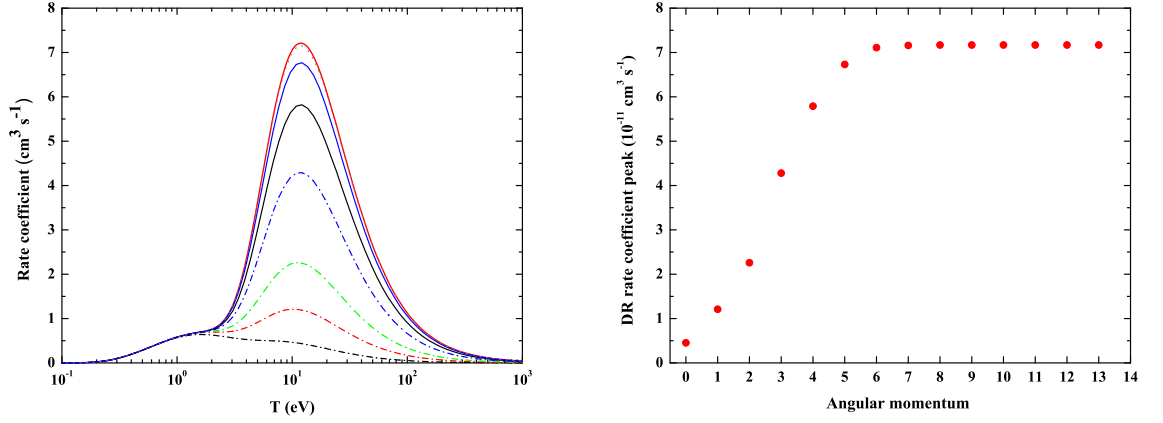
Figure 4.8   Study of the convergence of the angular momentum quantum number ℓ for the atomic collision $e^- + 3s^23p\,(^2P_{1/2}) \to 3s^23d\,(^2D_{3/2,\,5/2})n\ell$ in IC-coupling: left panel, the rate coefficient at different values of ℓ. black dash-dotted curve is for $\ell = 0$; red dash-dotted curve, for $\ell = 1$; green dash-dotted curve, for $\ell = 2$; blue dash-dotted curve, for $\ell = 3$; black solid curve, for $\ell = 4$; blue solid curve, for $\ell = 5$; gray dotted curve, $\ell = 6$; and red solid curve, for $\ell \leq 13$. Right panel, the variation of the DR rate coefficient peak with ℓ. Convergence occurs at $\ell \geq 7$.
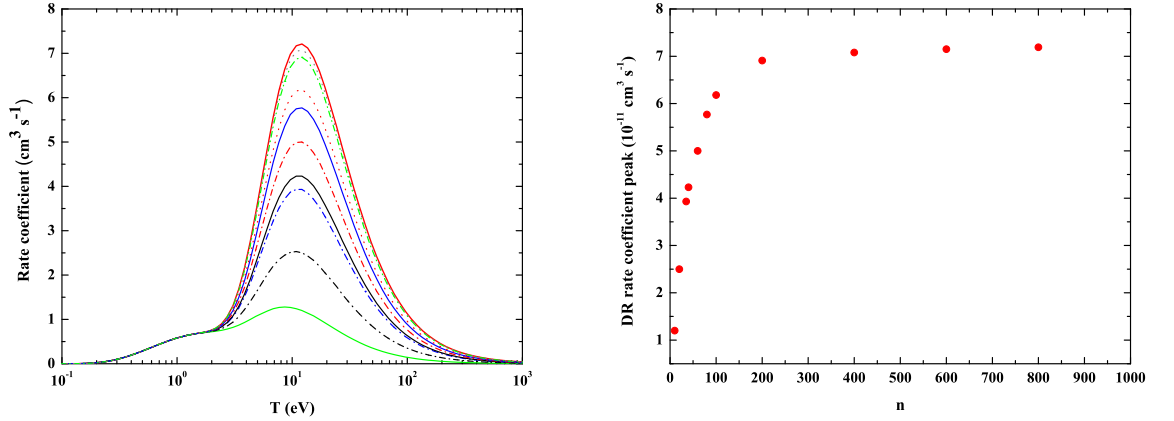
Figure 4.9   Study of the convergence of the principal quantum number n for the collision $e^- + 3s^23p\,(^2P_{1/2}) \to 3s^23d\,(^2D_{3/2,\,5/2})n\ell$ in IC-coupling: left panel, the rate coefficient at different values of n. Solid green curve is for $n = 10$; black dash-dotted curve, for $n = 20$; blue dash dotted curve, for $n = 35$; black solid curve, for $n = 40$; red dash-dotted curve, for $n = 60$; blue solid curve, for $n = 80$; red dotted curve, for $n = 100$; green dash-dotted curve, for $n = 200$; gray dotted curve, for $n = 400$; and red solid curve, for $n \leq 1000$. Right panel, the variation of the DR rate coefficient peak with n. Convergence occurs at $n \geq 200$.

The discrepancy in these two results can be attributed to the fact that the first result is based on an empirical data while the second is obtained by using the general expression
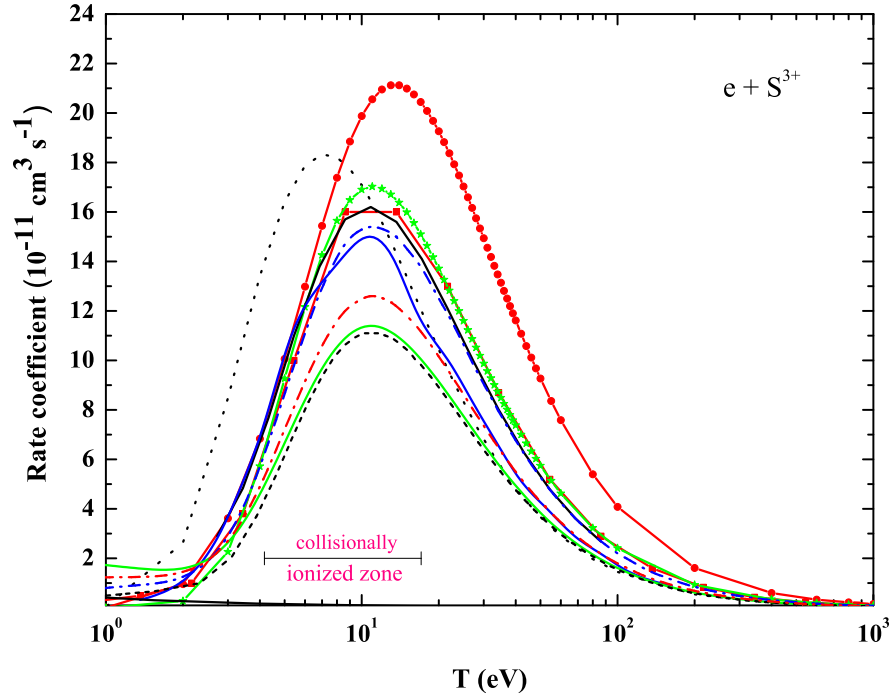
Figure 4.10 Comparisons between previous and present DR rate coefficients for S^{3+}: black dotted curve, empirical results of Mewe *et al.* [85]; red solid curve with circles, results of Aldrovandi and Péquignot [84]; green solid curve with stars, results of Shull and Steenberg [86]; red solid line with squares, data of Jacobs *et al.* [127]; black solid curve, data of Badnell [128]; blue solid line, data of Al-Mulhem and Nasser [129]; solid green curve, total rate coefficient by Nahar [130]; black dashed curve, recommended data of Mazzotta *et al.* [123], blue dash-dotted and red dash-dotted curves are my rate coefficients in *LS*- and IC-coupling schemes, respectively. The collisionally ionized zone is as recommended by Bryans *et al.* [204].

given by Burgess [4] that may overestimate the DR rate coefficients. The results of Shull and Steenberg [86] and Jacobs *et al.* [127] are nearly identical since the first one is just a fitting for the second. The data of Jacobs *et al.* are about 4% higher than my *LS*-coupling data. However, their calculations were truncated at a certain n value using the Inglis-Teller formula [206], where they applied a field strength which is determined by the Holtzmark formula for the micro field produced by a plasma with an electron density of 10^{10} cm^{-3}. Moreover, non-dipole autoionizing transitions into excited states were neglected. These

transitions are included in my calculations, with a contribution of 15% to the total rate. The rate coefficient by Al-Mulhem and Nasser [129] in LS-coupling peaks nearly at the same electron temperature as mine and is 2.6% lower. But those calculations were not complete because they considered only $3s \rightarrow 3p$ core excitation and did not include the other transitions such as $3s \rightarrow 3d$ and $3p \rightarrow 3d$, which we found to be more important. As seen, the recommended data by Mazzotta *et al.* [123] are taken from Nahar [130]. The data of Nahar are 26% lower than my LS-coupling calculations. I believe that my new results are more accurate and reliable [207].

For $\Delta n_c = 1$, only $3 \rightarrow 4$ ($3s \rightarrow 4\ell, 3p \rightarrow 4\ell$, and $3d \rightarrow 4\ell$) core excitations are considered. All the configurations in basis B plus the $3s^2 4\ell$, $3s3p4\ell$, and $3p^2 4\ell$ configurations are included for $0 \leq \ell \leq 3$. These 20 configurations give rise to 295 target levels. Contribution from $\Delta n_c = 1$ to the total DR rate coefficient for S^{3+} was found to be only about 3% at higher electron temperatures.

Now, the results for the rest of the Al-like isoelectronic sequence following the same methodology as for S^{3+} using basis B can be presented. The scaling parameters $\lambda_{3\ell}$ for all the Al-like ions are presented in Table 4.6.

4.4.2 Aluminum-Like Silicon, Phosphorus, Chlorine, and Argon

Fig. 4.11 shows a comparison between my calculated Maxwellian-averaged DR rate coefficients and other available data for Si^+. The curve of Mewe *et al.* [85] is 10% lower than my computed DR rate coefficient in LS-coupling and its peak is shifted to the lower electron temperatures by around 4.0 eV. I reproduced their DR data by using their fitting

Table 4.6 Radial scaling parameters used in the present study for $\Delta n_c = 0$ core excitations for the Al-like isoelectronic sequence.

	Si^+	P^{2+}	S^{3+}	Cl^{4+}	Ar^{5+}	K^{6+}	Ca^{7+}	Sc^{8+}	Ti^{9+}
λ_{3s}	1.2626	1.2183	1.1837	1.1543	1.1278	1.1032	1.0799	1.0574	1.0351
λ_{3p}	1.2526	1.2506	1.2494	1.2466	1.2407	1.2307	1.2161	1.1963	1.1686
λ_{3d}	1.1322	1.0373	0.9820	0.9496	0.9288	0.9142	0.9031	0.8945	0.8877

	V^{10+}	Cr^{11+}	Mn^{12+}	Fe^{13+}	Co^{14+}	Ni^{15+}	Cu^{16+}	Zn^{17+}
λ_{3s}	1.0132	0.9916	0.9701	0.9489	0.9281	0.9074	0.8870	0.8668
λ_{3p}	1.1392	1.1019	1.0613	1.0222	0.9884	0.9599	0.9360	0.9153
λ_{3d}	0.8817	0.8769	0.8727	0.8687	0.8650	0.8613	0.8578	0.8545

formula in Eq. (4.4) and the fitting parameters in Table 4.1. The DR rate coefficient of Aldrovandi and Péquignot [84] is only 2% higher, but their DR rate coefficient is based on the Burgess formula [4]. The rate of Jacobs *et al.* [189] is around 85% lower. Their calculations were performed for an electron density of 10^{10} cm^{-3} and they took into account all radiative stabilization and all autoionization processes that involve only single-electron electric-dipole transitions of the recombining ion core. Also, they omitted all other non-dipole transitions and truncated their calculations at a specific n value based on the Inglis-Teller limit [206]. As we can see from Fig. 4.11, all these calculations are missing the contribution at the low electron temperatures. The Nussbaumer and Storey [208] calculations were limited to the low-electron temperature region, covering the range between 0.086 and 5.171 eV. The rate coefficient of Nahar [130] is around 85% lower the my rate performed in LS-coupling. In 1995, Nahar and Pradhan [44] and Nahar [194] calculated the total rate coefficient for Si$^+$ in the close coupling approximation using the R-matrix method. But these calculations were performed in *LS*-coupling. A numerical error was then corrected in their integration step size that affected the total rate coefficients only in

the low-electron temperature region [195]. Finally, in 2000, Nahar presented electron ion recombination rate coefficients for Si^+, S^{3+}, Ar^{5+}, Ca^{7+}, and Fe^{13+} [130] [their target is the $(N+1)$-electron system]. The recommended data of Mazzotta *et al.* [123] are based on the data of Nahar [130]. My Mawellian-averaged DR rate coefficient performed in IC-coupling is the only calculation that accounts for the contribution of the fine structure in the ground state of Si^+.
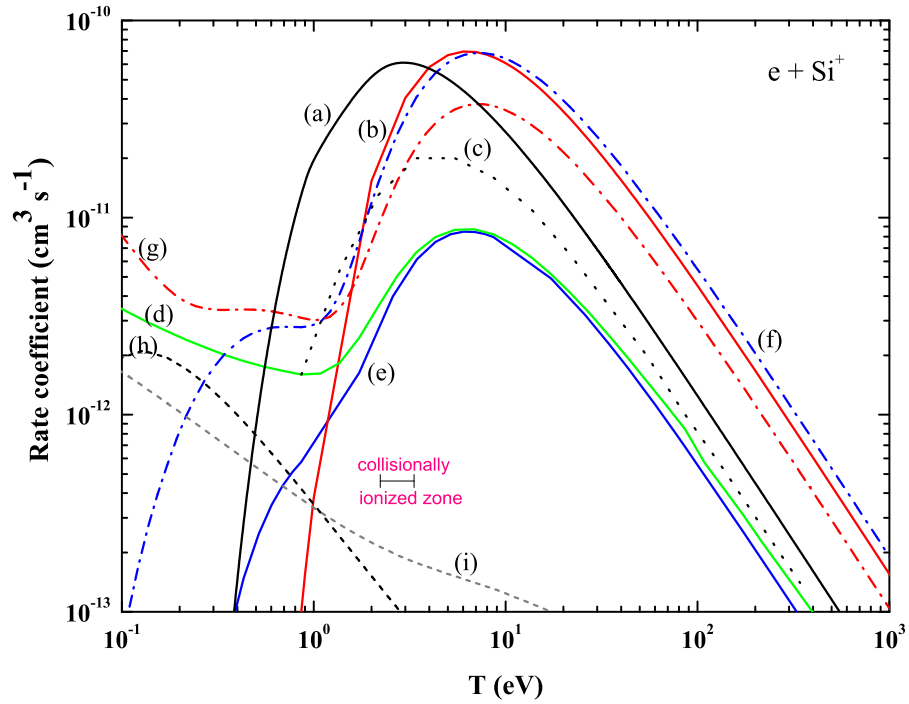
Figure 4.11   Comparison of available DR rate coefficients for Si^+: (a) black solid curve, DR data from the empirical formula of Mewe *et al.* [85]; (b) red solid curve, recommended DR data of Aldrovandi and Péquignot [84]; (c) black dotted curve, DR data from Jacobs *et al.* [189]; (d) green solid curve, total rate coefficient (RR + DR) using R-matrix by Nahar [130]; (e) blue solid curve, recommended DR data by Mazzotta *et al.* [123]; (f) blue dash-dotted curve, my DR data using *LS*-coupling; (g) red dash-dotted curve, my DR data using IC-coupling (MCBP); (h) black dashed curve, low temperature DR data from Nussbaumer and Storey [208]; and (i) gray dashed curve, my RR rate coefficient. The collisionally ionized zone is as recommended by Bryans *et al.* [204]. The photoionized zone is taken from Ref. [205].

To my knowledge, there are no computed DR rate coefficients for P^{2+}. Fig. 4.12, shows

81
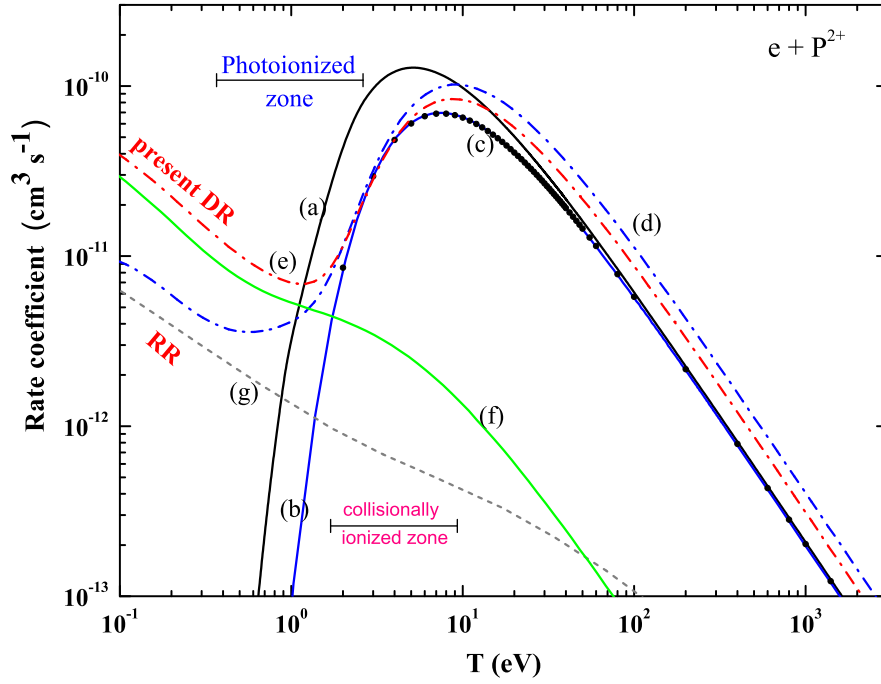
Figure 4.12 Comparison of available DR rate coefficients for P^{2+}: (a) black solid curve, DR data from the empirical formula of Mewe *et al.* [85]; (b) blue solid curve, recommended DR data by Mazzotta *et al.* [123]; (c) black circles, DR data from Landini and Fossi [89]; (d) blue dash-dotted curve, my DR data in *LS*-coupling; (e) red dash-dotted curve, my DR data using IC-coupling (MCBP); (f) green solid curve, contribution from the $3s3p3dn\ell$ series at low-electron temperatures; and (g) gray dashed curve, my RR rate coefficient. The collisionally ionized zone is as recommended by Bryans *et al.* [204]. The photoionized zone is taken from Ref. [205].

the Maxwellian-averaged DR rate coefficients in both *LS*- and IC-coupling schemes. The

fitting data of Mewe *et al.* [85] are reproduced from their fitting parameters for P^{2+} given

in Table 4.1 and using Eq. (4.4). The peak of their DR rate coefficient is 21% higher than

my DR rate coefficient in *LS*-coupling and is shifted by 5 eV toward the lower electron

temperatures. The DR rate coefficient of Landini and Fossi [89] is 33% lower than my DR

rate coefficient in *LS*-coupling. They computed the ionization equilibrium of P ions for

the low-density plasma using the same approximations as Shull and Steenberg [86], where

their fitting parameters for the rate coefficient for P^{2+} were obtained by an extrapolation

through the isoelectric sequence. As we can see from Fig. 4.12, the recommended data of Mazzotta *et al.* [123] for P^{2+} are based on the data of Landini and Fossi [89]. The contribution to the DR rate coefficient at low electron temperatures is mainly due to the $3s3p3dn\ell$ series.

In Table 4.7, a comparison between my calculated energy levels (in Ryderg) for Al-like Cl^{4+} and Ar^{5+} ions with the available data from NIST and MCHF calculations by Fischer *et al.* [198]. Good agreement is obtained for most of the levels.

Table 4.7 Comparisons of the lowest energy levels (in Rydbergs) for Al-like Cl^{4+} and Ar^{5+}.

m	config.	$^{2S+1}L_J^\pi$	Present[a]	NIST[b]	MCHF[c]	$^{2S+1}L_J^\pi$	Present[a]	NIST[b]	MCHF[c]
			Cl^{4+}				Ar^{5+}		
1	$3s^23p$	$^2P_{1/2}^o$	0.00000	0.00000	0.00000	$^2P_{1/2}^o$	0.00000	0.00000	0.00000
2		$^2P_{3/2}^o$	0.01113	0.01358	0.01240	$^2P_{3/2}^o$	0.01646	0.02011	0.01866
3	$3s3p^2$	$^4P_{1/2}$	0.76229	0.77998	0.76781	$^4P_{1/2}$	0.89646	0.91271	0.89984
4		$^4P_{3/2}$	0.76621	0.78486	0.77228	$^4P_{3/2}$	0.90231	0.91997	0.90659
5		$^4P_{5/2}$	0.77248	0.79256	0.77923	$^4P_{5/2}$	0.91155	0.93122	0.91691
6		$^2D_{3/2}$	1.02861	1.03186	1.02534	$^2D_{3/2}$	1.20553	1.20708	1.20063
7		$^2D_{5/2}$	1.02895	1.03251	1.02591	$^2D_{5/2}$	1.20611	1.20810	1.20151
8		$^2S_{1/2}$	1.30234	1.33633	1.33875	$^2S_{1/2}$	1.51656	1.54737	1.55076
9		$^2P_{1/2}$	1.40521	1.43918	1.45729	$^2P_{1/2}$	1.63326	1.66016	1.68074
10		$^2P_{3/2}$	1.41243	1.44794	1.46535	$^2P_{3/2}$	1.64379	1.67287	1.69261

[a] present work: 129-level MCBP calculations.

[b] data taken from NIST.

[c] MCHF theory calculations of Froese-Fischer *et al.* [198].

My Maxwellian-averaged DR rate coefficients for Cl^{4+} are presented in Fig. 4.13 for *LS*- and IC-coupling calculations. The peak of the DR rate coefficient of Mewe *et al.* is 18% lower than my DR rate coefficient performed in *LS*-coupling scheme and is shifted
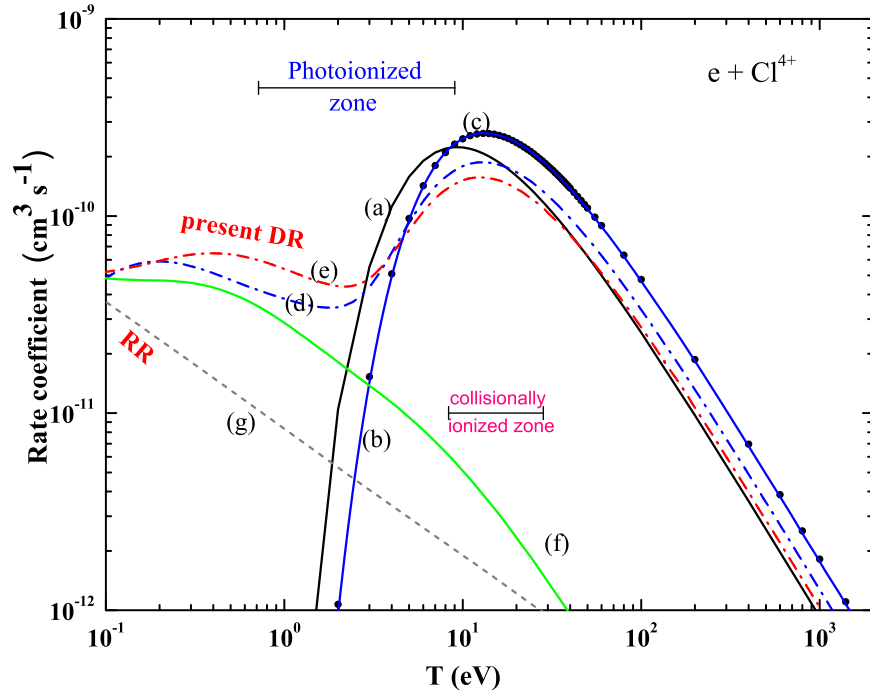
Figure 4.13 Comparison of available DR rate coefficients for Cl^{4+}: (a) black solid curve, DR data from the empirical formula of Mewe *et al.* [85]; (b) blue solid curve, recommended DR data by Mazzotta *et al.* [123]; (c) back circles curve, DR data from Landini and Fossi [89]; (d) blue dash-dotted curve, my DR data in *LS*-coupling; (e) red dash-dotted curve, my DR data in IC-coupling, (f) green solid curve, contribution from the series $3s^2 3pn\ell$; and (g) gray dashed curve, my RR rate coefficient. The collisionally ionized zone is as recommended by Bryans *et al.* [204]. The photoionized zone is taken from Ref. [205].

by around $4\,\mathrm{eV}$ toward the lower electron temperatures. The DR rate coefficient of Landini and Fossi [89] is higher by 44% than my DR rate coefficient performed in LS-coupling. Their DR rate coefficient is obtained by extrapolation of the fitting parameters from Shull and Steenberg [86]. As seen from Fig. 4.13, the recommended DR data of Mazzotta *et al.* [123] for Cl^{4+} are exactly the same as the work of Landini and Fossi [89]. The DR rate coefficient at the low electron temperatures is dominated by the contribution from $3s^2 3pn\ell$ series.

Fig. 4.14 shows a comparison of my Maxwellian-averaged DR rate coefficients for
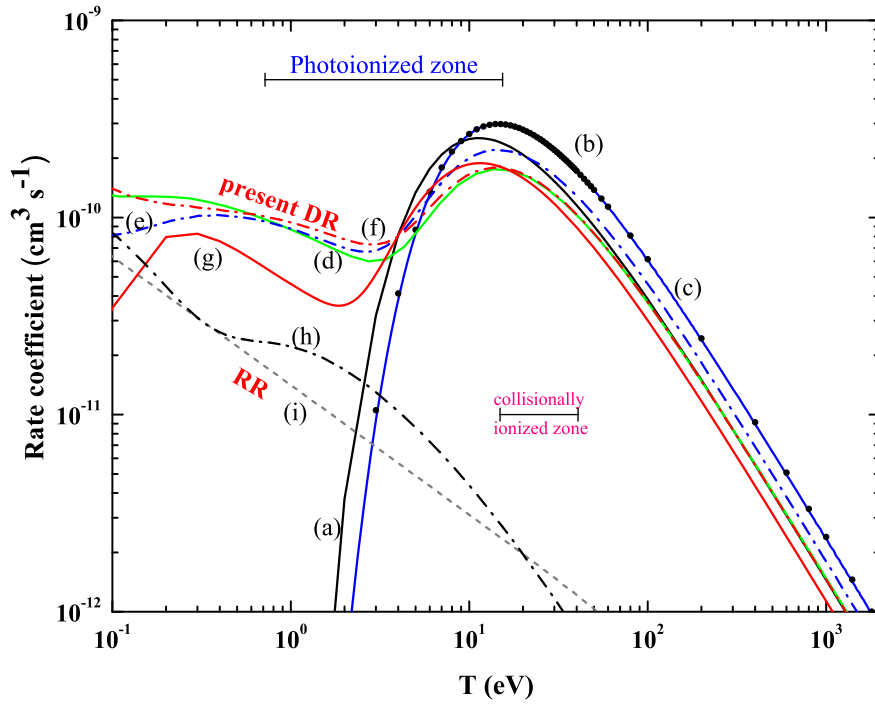
Figure 4.14 Comparison of available DR rate coefficients for Ar^{5+}: (a) black solid curve, DR from the empirical formula of Mewe *et al.* [85]; (b) black circles, recommended DR data of Shull and Steenberg [86]; (c) blue solid curve, recommended DR data by Mazzotta *et al.* [123]; (d) green solid curve, total rate coefficient (RR + DR) using R-matrix by Nahar [130]; (e) blue dash-dotted curve, my DR data in *LS*-coupling scheme; (f) red dash-dotted curve, my DR data in IC-coupling scheme; (g) red solid curve, configuration-average data of Loch *et al.* [185]; (h) black dash-dotted curve, contribution from the series $3s^2 3pn\ell$; and (i) gray dashed curve, my RR rate coefficient. The collisionally ionized zone is as recommended by Bryans *et al.* [204]. The photoionized zone is taken from Ref. [205].

Ar^{5+} in both *LS*- and IC-coupling and other available DR rate coefficients. The peak of the empirical DR rate coefficient of Mewe *et al.* [85] is higher than my DR rate coefficient performed in *LS*-coupling by 15% and is shifted toward the lower electron temperatures by 4.5 eV. Their DR data are obtained by using the empirical formula in Eq. (4.4) and the fitting parameters in Table 4.1. The DR rate coefficient of Shull and Steenberg [86] is 40% higher than my DR rate coefficient performed in *LS*-coupling. Their rate coefficient for Ar^{5+} is obtained by extrapolation for the work of Jacobs *et al.* [127, 190] between

S and Ca ions. The recommended data of Mazzotta *et al.* [123] are based on Shull and Steenberg [86] (see Fig. 4.14). Available calculations for DR rate coefficients for Ar^{5+} are either from the unified close-coupling R-matrix approximation in *LS*-coupling by Nahar [130] or from the configuration-average distorted-wave approximation (CADWA) of Loch *et al.* [185] (see Chapter III). The peak of the DR rate coefficient of Nahar [130] is 18% lower than my DR rate coefficient performed in *LS*-coupling. The peak of the CADWA is 13% lower and is shifted toward the lower electron temperatures by 5 eV. Neither of these calculations included the fine structure splitting in the ground state, which has an effect on the rate coefficient at higher electron temperatures as seen in my study of S^{3+} (see Sec. 4.4.1). Moreover, the CADWA DR rate coefficient is missing the $3s \rightarrow 3d$ core-excitation. The code was designed to handle the transitions only between two active electrons, but for Ar^{5+} $\Delta n_c = 0$ ($3s \rightarrow 3p, 3p \rightarrow 3d$, and $3s \rightarrow 3d$) core excitations give rise to three active electrons when one excites $3s \rightarrow 3d$. The modifications of the code are underway to overcome such limitation.

4.4.3 Aluminum-Like Potassium, Calcium, Scandium, and Titanium

Now we move to higher Al-like ions though the periodic table. Comparisons between my calculated energy levels for the Al-like K^{6+}, Ca^{7+}, Sc^{8+}, and Ti^{9+} ions and other available data are presented in Table 4.8. Good agreement is obtained between my calculated energy levels and the available data taken from NIST, the perturbation theory calculations (MR-MP) of Santana *et al.* [209], and the MCHF calculations of Froese-Fischer *et al.* [198].

Table 4.8   Comparisons of the lowest energy levels (in Rydbergs) for the Al-like K^{6+}, Ca^{7+}, Sc^{8+}, and Ti^{9+}.

			K^{6+}					Ca^{7+}			
m	config.	$^{2S+1}L_J^{\pi}$	Present[a]	NIST[b]	MR-MP[c]	MCHF[d]	$^{2S+1}L_J^{\pi}$	Present[a]	NIST[b]	MR-MP[c]	MCHF[d]
1	$3s^23p$	$^2P_{1/2}^o$	0.00000	0.00000	0.00000	0.00000	$^2P_{1/2}^o$	0.00000	0.00000	0.00000	0.00000
2		$^2P_{3/2}^o$	0.02354	0.02856	0.02857	0.02684	$^2P_{3/2}^o$	0.03270	0.03926	0.03925	0.03729
3	$3s3p^2$	$^4P_{1/2}$	1.03189	1.04477	1.04654	1.03346	$^4P_{1/2}$	1.16874	1.17645	1.18279	1.16892
4		$^4P_{3/2}$	1.04033	1.05512	1.05696	1.04322	$^4P_{3/2}$	1.18060	1.19083	1.19724	1.18261
5		$^4P_{5/2}$	1.05346	1.07095	1.07280	1.05789	$^4P_{5/2}$	1.19874	1.21237	1.21877	1.20278
6		$^2D_{3/2}$	1.38437	1.38407	1.38384	1.37757	$^2D_{3/2}$	1.56549	1.56348	1.56316	1.55694
7		$^2D_{5/2}$	1.38533	1.38560	1.38538	1.37892	$^2D_{5/2}$	1.56704	1.56584	1.56546	1.55899
8		$^2S_{1/2}$	1.73307	1.75952	1.76008	1.76369	$^2S_{1/2}$	1.95223	1.97367	1.97333	1.97839
9		$^2P_{1/2}$	1.86305	1.88179	1.88226	1.90423	$^2P_{1/2}$	2.09485	2.10518	2.12885	2.12893
10		$^2P_{3/2}$	1.87787	1.89938	1.89985	1.92093	$^2P_{3/2}$	2.11503	2.12865	2.10536	2.15152

			Sc^{8+}					Ti^{9+}			
m	config.	$^{2S+1}L_J^{\pi}$	Present[a]	NIST[b]	MR-MP[c]	MCHF[d]	$^{2S+1}L_J^{\pi}$	Present[a]	NIST[b]	MR-MP[c]	MCHF[d]
1	$3s^23p$	$^2P_{1/2}^o$	0.00000	0.00000	0.00000	0.00000	$^2P_{1/2}^o$	0.00000	0.0	0.00000	0.00000
2		$^2P_{3/2}^o$	0.04437	0.05250	0.05253	0.05038	$^2P_{3/2}^o$	0.05908	0.06875	0.06874	0.06652
3	$3s3p^2$	$^4P_{1/2}$	1.30716	1.30767	1.32106	1.30780	$^4P_{1/2}$	1.44718	1.46175	1.46178	1.44781
4		$^4P_{3/2}$	1.32347	1.32701	1.34064	1.32676	$^4P_{3/2}$	1.46922	1.48771	1.48778	1.47324
5		$^4P_{5/2}$	1.34792	1.35577	1.36917	1.35392	$^4P_{5/2}$	1.50152	1.52463	1.52473	1.50870
6		$^2D_{3/2}$	1.74930	1.74607	1.74574	1.74119	$^2D_{3/2}$	1.93625	1.93237	1.93211	1.92770
7		$^2D_{5/2}$	1.75172	1.74952	1.74914	1.74435	$^2D_{5/2}$	1.93996	1.93743	1.93712	1.93237
8		$^2S_{1/2}$	2.17444	2.19033	2.19099	2.19686	$^2S_{1/2}$	2.40039	2.40990	2.41116	2.41723
9		$^2P_{1/2}$	2.32908	2.33129	2.33150	2.35746	$^2P_{1/2}$	2.56655	2.56113	2.56132	2.58795
10		$^2P_{3/2}$	2.35578	2.36158	2.36182	2.38729	$^2P_{3/2}$	2.60099	2.59912	2.59928	2.62591

[a] present work: 129-level MCBP calculations.

[b] data taken from NIST.

[c] perturbation theory calculations of Santana *et al.* [209].

[d] MCHF theory calculations of Froese-Fischer *et al.* [198].

Fig. 4.15 shows my calculated Maxwellian-averaged DR rate coefficients for K^{6+} in both *LS*- and IC-coupling. The peak of the DR rate coefficient of Mewe *et al.* [85] is 8% higher than my DR rate coefficient performed in *LS*-coupling and is shifted to the lower electron temperatures by 3 eV. I reproduced their data for K^{6+} by using their fitting
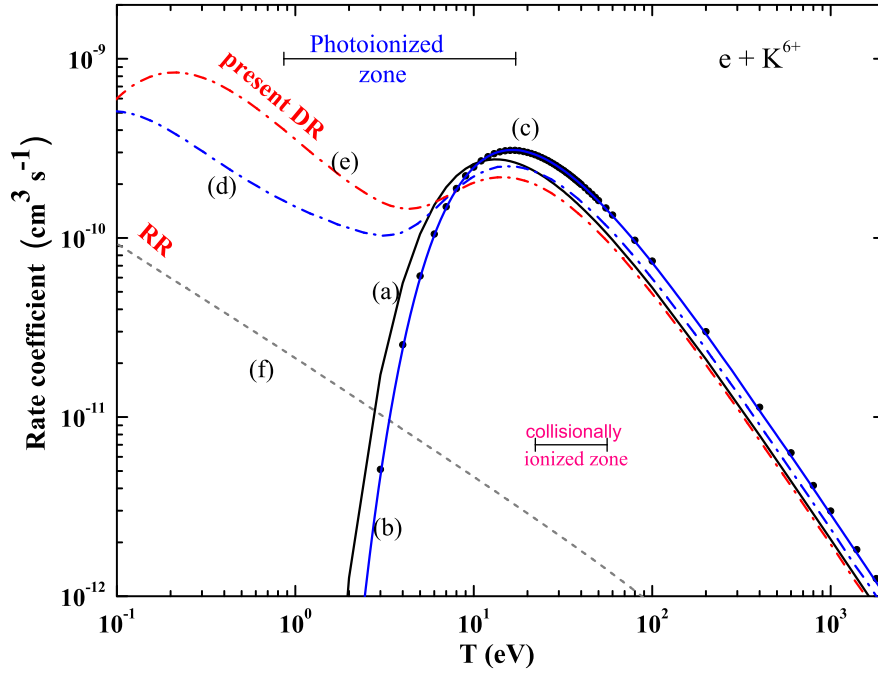
Figure 4.15 Comparison of available DR rate coefficients for K^{6+}: (a) black solid curve, DR data from the empirical formula of Mewe *et al.* [85]; (b) blue solid curve, recommended DR data by Mazzotta *et al.* [123]; (c) black circles curve, DR data from Landini and Fossi [89]; (d) blue dash-dotted curve, my DR data in *LS*-coupling; (e) red dash-dotted curve, my DR rate coefficient in IC-coupling; and (e) gray dashed curve, my RR rate coefficient. The collisionally ionized zone is as recommended by Bryans *et al.* [204]. The photoionized zone is taken from Ref. [205].

parameters in Table 4.1 and their Eq. (4.4). The DR rate coefficient of Landini and Fossi [89] is 25% higher than my DR rate coefficient performed in LS-coupling. The DR data of Landini and Fossi [89] are reproduced by using the DR fitting parameters given in Table 4.2 and using Eq. (4.3). The parameters for the DR rate coefficients of Landini and Fossi [89] were obtained by extrapolating the work of Shull and Steenberg [86]. From Fig. 4.15, it is clear that the recommended DR rate coefficient of Mazzotta *et al.* [123] are taken from the extrapolation work of Landini and Fossi [89]. The DR rate coefficient peak at 0.2 eV is due to contributions form $3s3p^2n\ell$, $3s^23dn\ell$, and $3s3p3dn\ell$ series, that are omitted in the data

of Mewe *et al.* [85], Landini and Fossi [89], and Mazzotta *et al.* [123].
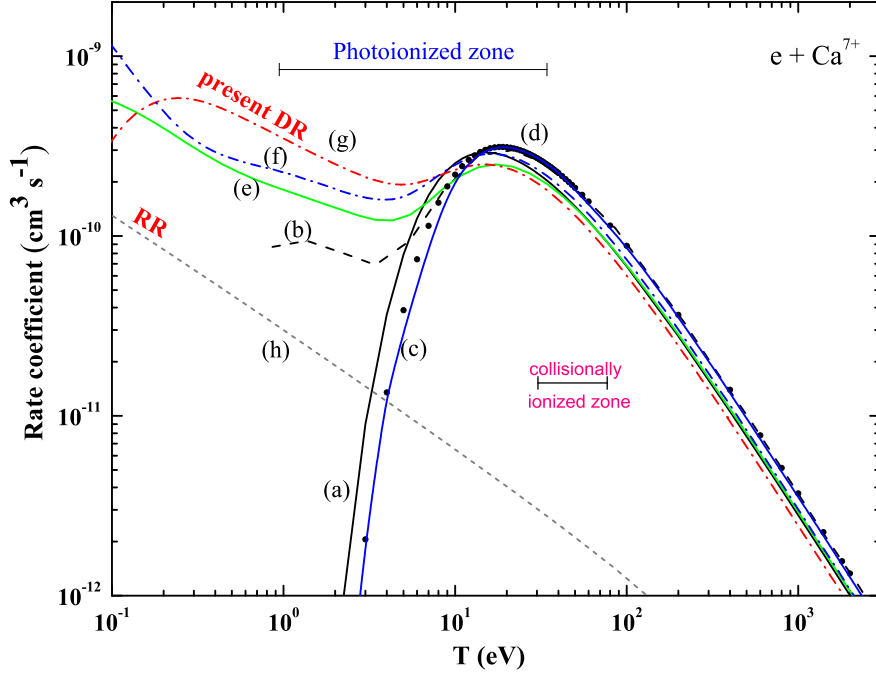
Figure 4.16 Maxwellian-averaged DR rate coefficients for Ca^{7+}: (a) black solid curve, DR from the empirical formula of Mewe *et al.* [85]; (b) black dashed curve, data of Jacobs *et al.* [190]; (c) blue solid curve, recommended DR data by Mazzotta *et al.* [123]; (d) black circles curve, recommended DR data of Shull and Steenberg [86]; (e) green solid curve, total rate coefficient (RR + DR) using R-matrix by Nahar [130]; (f) blue dash-dotted curve, my DR data using *LS*-coupling scheme; (g) and (h) red dash-dotted and gray dashed curves, my DR and RR data using IC-coupling (MCBP) scheme, respectively. The collisionally ionized zone is as recommended by Bryans *et al.* [204]. The photoionized zone is taken from Ref. [205].

Fig. 4.16, shows my calculated Maxwellian-averaged DR rate coefficients for Ca^{7+} in both *LS*- and IC-coupling. The DR rate coefficient of Mewe *et al.* [85] is 2% higher than my DR rate coefficient performed in *LS*-coupling and is shifted to the lower electron temperatures by 2 eV. I reproduced their data for Ca^{7+} by using their fitting parameters in Table 4.1 and their Eq. (4.4). The DR rate coefficients of Jacobs *et al.* [190] is 2% higher than my DR rate coefficient performed in *LS*-coupling. They took into account autoionization to

excited states of Ca^{7+} and stabilizing radiative transitions of the recombing electron. The DR rate coefficient of Shull and Steenberg [86] is based on a least square fitting for the work of Jacobs *et al.* [190]. The peak of the DR rate coefficient of Nahar [130] is 12% lower than my DR rate coefficient performed in LS-coupling. This rate coefficient was carried out in the close coupling approximation using the R-matrix method. As we can see from Fig. 4.16, the recommended DR rate coefficient of Mazzotta *et al.* [123] matches the work of Shull and Steenberg [86] for Ca^{7+}. The peak at an electron temperature of 0.2 eV is due to contributions form $3s^23pn\ell, 3s3p^2n\ell, 3s^23dn\ell, 3p^3n\ell$, and $3s3p3dn\ell$ series, that are omitted in the data of Mewe *et al.* [85], Shull and Steenberg [86], and Mazzotta *et al.* [123].

Fig. 4.17 shows the Maxwellian-averaged DR rate coefficients performed in LS- and IC-coupling for Sc^{8+}. The DR rate coefficient of Mewe *et al.* [85] is 5% higher than my DR rate coefficient performed in LS-coupling. I reproduced their data for Sc^{8+} by using their fitting parameters in Table 4.1 and their Eq. (4.4). The recommended DR rate coefficient of Mazzotta *et al.* [123] is 11% higher than my DR rate coefficient performed in LS-coupling. It is not clear how Mazzotta *et al.* [123] obtained their fitting coefficients. The peak of my DR rate coefficient performed in IC-coupling scheme is 10% lower than the one performed in LS-coupling. As seen from Fig. 4.17, the DR rate coefficients of Mewe *et al.* [85] and Mazzotta *et al.* [123] missed the contributions at electron temperatures below 1 eV. The main contributions to the DR rate coefficients at electron temperatures below 0.1 eV are due to the $3s^23dn\ell$ series.

Fig. 4.18 shows the calculated Maxwellian-averaged DR rate coefficients for Ti^{9+} in
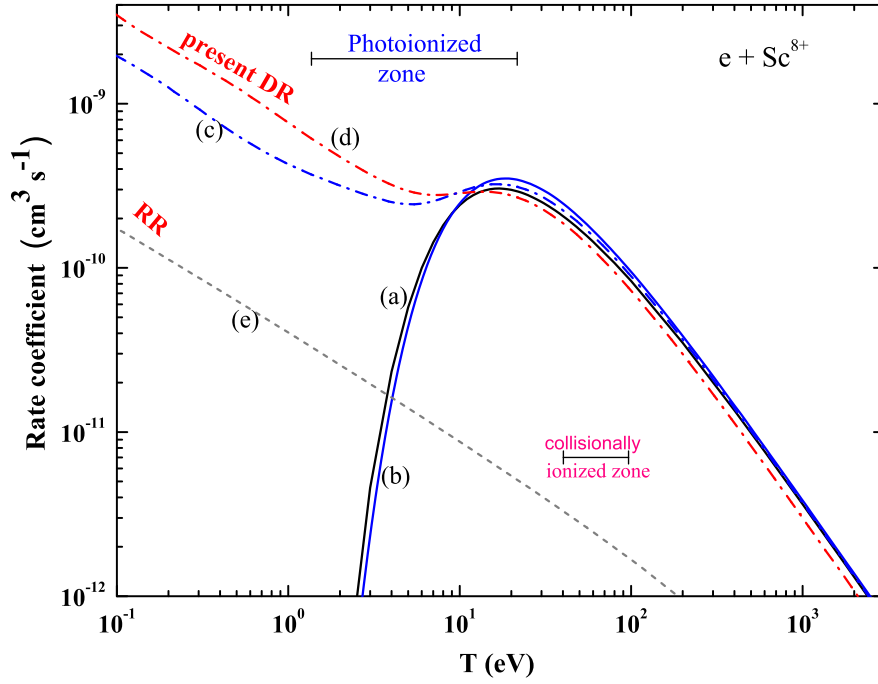
Figure 4.17 Comparison of available DR rate coefficients for Sc^{8+}: (a) black solid curve, DR from the empirical formula of Mewe *et al.* [85]; (b) blue solid curve, recommended DR data by Mazzotta *et al.* [123]; (c) blue dash-dotted curve, my DR data in *LS*-coupling; (d) red dash-dotted curve, my DR data in IC-coupling; and (e) gray dashed curve, my RR data. The collisionally ionized zone is as recommended by Bryans *et al.* [204]. The photoionized zone is taken from Ref. [205].

both *LS*- and IC-coupling schemes. The DR rate coefficient of Mewe *et al.* [85] for Ti^{9+} was reproduced by using their fitting parameters in Table 4.1 and their Eq. (4.4). The recommended DR rate coefficient of Mazzotta *et al.* [123] matches the DR rate coefficient of Landini and Fossi [89]. The data of Landini and Fossi were obtained by extrapolating the work of Shull and Steenberg [86]. The main contributions to the DR rate coefficients for Ti^{9+} below 1.0 eV are mainly due to the $3s3p3dn\ell$ and $3s3p^2n\ell$ series.

It is clear from my study for these Al-like ions that all previously existing work for this isoelectronic sequence are based on empirical formulas that differ by orders of magnitudes at the low-electron temperatures compared to my present results. In Sec. 4.4.4, The

91
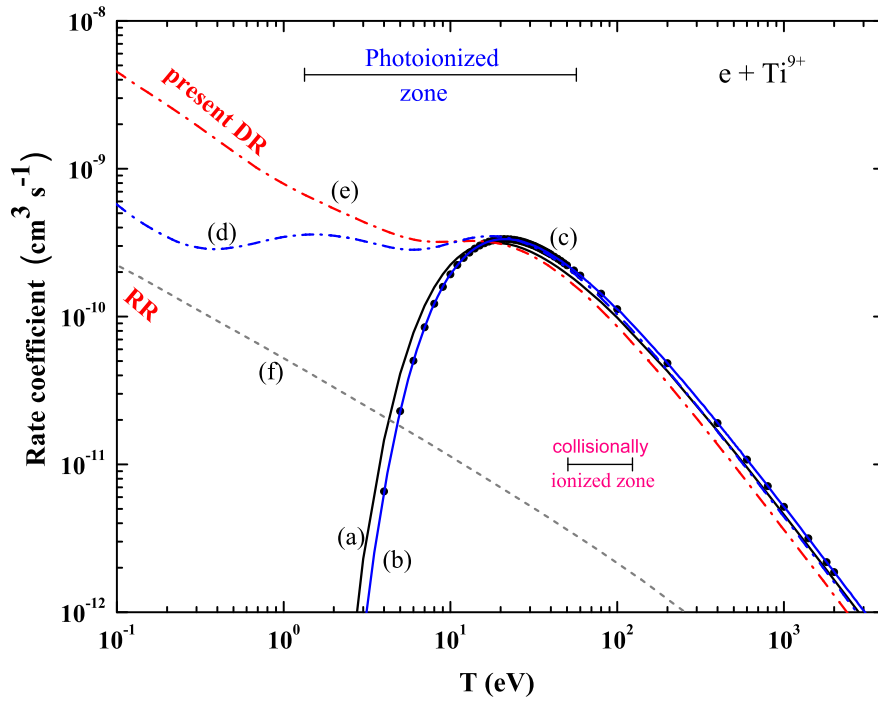
Figure 4.18 Maxwellian-averaged rate coefficients for Ti^{9+}: (a) black solid curve, DR data from the empirical formula of Mewe *et al.* [85]; (b) blue solid curve, recommended DR data by Mazzotta *et al.* [123]; (c) black circles, DR data from Landini and Fossi [89]; (d) blue dash-dotted curve, my DR data using *LS*-coupling; (e) red dash-dotted curve, my DR in IC-coupling; and (f) gray dashed curves, my RR data. The collisionally ionized zone is as recommended by Bryans *et al.* [204]. The photoionized zone is taken from Ref. [205].

comparison with the experimental measurements for Fe^{13+} will be used as a check on my

results.

4.4.4 Aluminum-Like Iron Peak Elements

In Table 4.9, comparisons between my lowest calculated energy levels for Al-like V^{10+}, Cr^{11+}, Mn^{12+}, and Fe^{13+} ions with the data taken from NIST, the perturbation theory (MR-MP) calculations of Santana *et al.* [209], and the MCHF calculations of Froese-Fischer *et al.* [198]. The energy levels for the rest of the iron peak elements (Co^{14+} and Ni^{15+}) are presented in Table 4.10. Very good agreement is obtained for all these ions.

Table 4.9 Comparisons of the lowest energy levels (in Rydbergs) for the Al-like V^{10+}, Cr^{11+}, Mn^{12+}, and Fe^{13+}.

			V^{10+}					Cr^{11+}			
m	config.	$^{2S+1}L_J^{\pi}$	Present[a]	NIST[b]	MR-MP[c]	MCHF[d]	$^{2S+1}L_J^{\pi}$	Present[a]	NIST[b]	MR-MP[c]	MCHF[d]
1	$3s^23p$	$^2P_{1/2}^o$	0.00000	0.00000	0.00000	0.00000	$^2P_{1/2}^o$	0.00000	0.00000	0.00000	0.00000
2		$^2P_{3/2}^o$	0.07718	0.08836	0.11174	0.08615	$^2P_{3/2}^o$	0.09943	0.11173	0.11174	0.10976
3	$3s3p^2$	$^4P_{1/2}$	1.58928	1.60490	1.75051	1.59039	$^4P_{1/2}$	1.73327	1.75073	1.75051	1.73579
4		$^4P_{3/2}$	1.61855	1.63881	1.79428	1.62393	$^4P_{3/2}$	1.77169	1.79439	1.79428	1.77941
5		$^4P_{5/2}$	1.66036	1.68577	1.85290	1.66930	$^4P_{5/2}$	1.82498	1.85305	1.85290	1.83644
6		$^2D_{3/2}$	2.12694	2.12300	2.31828	2.11867	$^2D_{3/2}$	2.32190	2.31852	2.31828	2.31481
7		$^2D_{5/2}$	2.13251	2.13034	2.32862	2.12549	$^2D_{5/2}$	2.33011	2.32889	2.32862	2.32461
8		$^2S_{1/2}$	2.62949	2.63278	2.85964	2.64103	$^2S_{1/2}$	2.86276	2.85905	2.85964	2.86862
9		$^2P_{1/2}$	2.80725	2.79578	3.03631	2.82288	$^2P_{1/2}$	3.05274	3.03631	3.03631	3.06354
10		$^2P_{3/2}$	2.85049	2.84215	3.09154	2.86991	$^2P_{3/2}$	3.10571	3.09148	3.09154	3.12033

			Mn^{12+}					Fe^{13+}			
m	config.	$^{2S+1}L_J^{\pi}$	Present[a]	NIST[b]	MR-MP[c]	MCHF[d]	$^{2S+1}L_J^{\pi}$	Present[a]	NIST[b]	MR-MP[c]	MCHF[d]
1	$3s^23p$	$^2P_{1/2}^o$	0.00000	0.00000	0.00000	0.00000	$^2P_{1/2}^o$	0.00000	0.00000	0.00000	0.00000
2		$^2P_{3/2}^o$	0.12633	0.13938	0.13939	0.13786	$^2P_{3/2}^o$	0.15824	0.171797	0.17179	0.17101
3	$3s3p^2$	$^4P_{1/2}$	1.87950	1.89955	1.89916	1.88426	$^4P_{1/2}$	2.02835	2.05139	2.05117	2.03602
4		$^4P_{3/2}$	1.92932	1.95509	1.95489	1.94027	$^4P_{3/2}$	2.09214	2.12133	2.12137	2.10720
5		$^4P_{5/2}$	1.99618	2.02723	2.02697	2.01083	$^4P_{5/2}$	2.17468	2.20879	2.20878	2.19326
6		$^2D_{3/2}$	2.52181	2.51963	2.51942	2.51679	$^2D_{3/2}$	2.72742	2.72689	2.72679	2.72540
7		$^2D_{5/2}$	2.53374	2.53422	2.53398	2.53072	$^2D_{5/2}$	2.74446	2.74719	2.74703	2.74494
8		$^2S_{1/2}$	3.09966	3.08920	3.08967	3.10028	$^2S_{1/2}$	3.33960	3.32333	3.32355	3.33631
9		$^2P_{1/2}$	3.30384	3.28409	3.28410	3.31132	$^2P_{1/2}$	3.56183	3.54036	3.54029	3.56777
10		$^2P_{3/2}$	3.36700	3.34822	3.34831	3.37826	$^2P_{3/2}$	3.63508	3.61328	3.61332	3.64486

[a] present work: 129-level MCBP calculations.

[b] data taken from NIST.

[c] perturbation theory calculations of Santana *et al.* [209].

[d] MCHF theory calculations of Froese-Fischer *et al.* [198].

Fig. 4.19 shows my calculated Maxwellian-averaged DR rate coefficients in both *LS*- and IC-coupling for V^{10+}. The DR rate coefficient of Mewe *et al.* [85] for V^{10+} was reproduced by using their fitting parameters in Table 4.1 and their Eq. (4.4). The recommended DR data of Mazzotta *et al.* [123] are very close to Mewe *et al.* data [85]. Contributions to

Table 4.10 Comparisons of the lowest energy levels (in Rydbergs) for the Al-like Co^{14+}, Ni^{15+}, Cu^{16+}, and Zn^{17+}.

			Co^{14+}				Ni^{15+}		
m	config.	$^{2S+1}L_J^\pi$	Present[a]	NIST[b]	MR-MP[c]	$^{2S+1}L_J^\pi$	Present[a]	NIST[b]	MR-MP[c]
1	$3s^23p$	$^2P_{1/2}^o$	0.00000	0.00000	0.00000	$^2P_{1/2}^o$	0.00000	0.00000	0.00000
2		$^2P_{3/2}^o$	0.19545	0.20940	0.20947	$^2P_{3/2}^o$	0.23841	0.25297	0.25296
3	$3s3p^2$	$^4P_{1/2}$	2.18019	2.20640	2.20612	$^4P_{1/2}$	2.33525	2.36464	2.36443
4		$^4P_{3/2}$	2.26085	2.29365	2.29374	$^4P_{3/2}$	2.43607	2.47264	2.47288
5		$^4P_{5/2}$	2.36111	2.39835	2.39840	$^4P_{5/2}$	2.55609	2.59665	2.59669
6		$^2D_{3/2}$	2.93950	2.94089	2.94087	$^2D_{3/2}$	3.15876	3.16239	3.16237
7		$^2D_{5/2}$	2.96338	2.96882	2.96865	$^2D_{5/2}$	3.19169	3.20023	3.20006
8		$^2S_{1/2}$	3.58235	3.56173	3.56191	$^2S_{1/2}$	3.82840	3.80475	3.80492
9		$^2P_{1/2}$	3.82830	3.80652	3.80648	$^2P_{1/2}$	4.10504	4.08402	4.08393
10		$^2P_{3/2}$	3.91106	3.88773	3.88777	$^2P_{3/2}$	4.19641	4.17280	4.17269

			Cu^{16+}				Zn^{17+}		
m	config.	$^{2S+1}L_J^\pi$	Present[a]	NIST[b]	MR-MP[c]	$^{2S+1}L_J^\pi$	Present[a]	NIST[b]	MR-MP[c]
1	$3s^23p$	$^2P_{1/2}^o$	0.00000	0.00000	0.00000	$^2P_{1/2}^o$	0.00000	0.00000	0.00000
2		$^2P_{3/2}^o$	0.28761	0.30290	0.30286	$^2P_{3/2}^o$	0.34368	0.35980	0.35976
3	$3s3p^2$	$^4P_{1/2}$	2.49368	2.52631	2.52618	$^4P_{1/2}$	2.65562	2.69006	2.69136
4		$^4P_{3/2}$	2.61847	2.65917	2.65941	$^4P_{3/2}$	2.80873	2.85220	2.85391
5		$^4P_{5/2}$	2.76023	2.80404	2.80427	$^4P_{5/2}$	2.97416	3.01957	3.02160
6		$^2D_{3/2}$	3.38595	3.39206	3.39198	$^2D_{3/2}$	3.62178	3.63040	3.63031
7		$^2D_{5/2}$	3.43058	3.44261	3.44249	$^2D_{5/2}$	3.68149	3.69756	3.69727
8		$^2S_{1/2}$	4.07847	4.05294	4.05309	$^2S_{1/2}$	4.33341	4.30666	4.30697
9		$^2P_{1/2}$	4.39370	4.37423	4.37401	$^2P_{1/2}$	4.69582	4.67820	4.67807
10		$^2P_{3/2}$	4.49257	4.46946	4.46920	$^2P_{3/2}$	4.80090	4.77852	4.77848

[a] present work: 129-level MCBP calculations.

[b] data taken from NIST.

[c] perturbation theory calculations of Santana *et al.* [209].

the DR rate coefficients at the low electron temperatures below 1.0 eV mainly come from

the $3p^3n\ell$ and $3s3p^2n\ell$ series, that are omitted in the DR rate coefficients of Mewe *et al.*
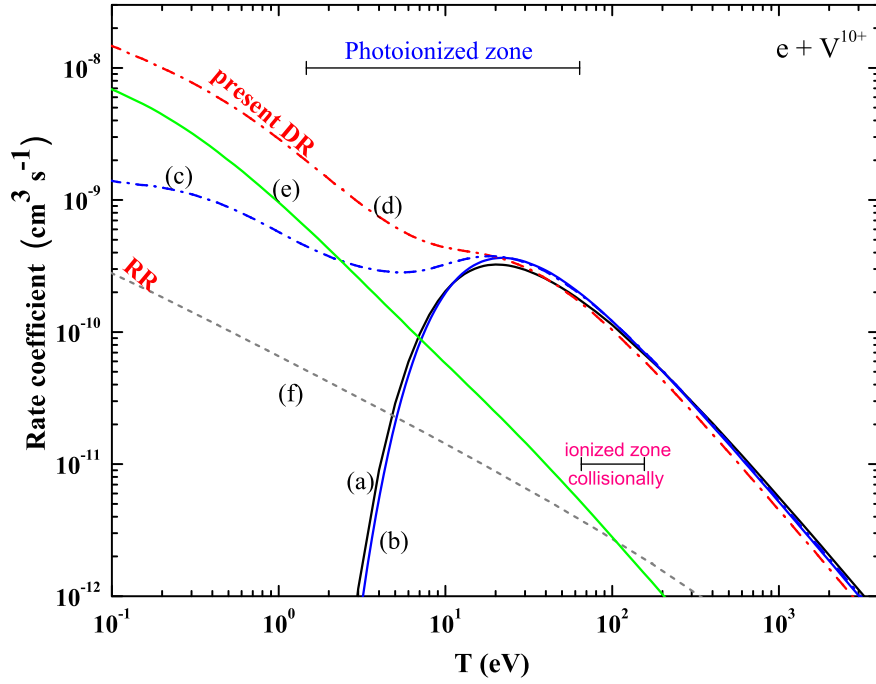
Figure 4.19 Maxwellian-averaged rate coefficients for V^{10+}: (a) black solid curve, DR data from the empirical formula of Mewe *et al.* [85]; (b) blue solid curve, recommended DR data by Mazzotta *et al.* [123]; (c) blue dash-dotted curve, my DR data in *LS*-coupling; (d) red dash-dotted curve, my DR data in IC-coupling; (e) green solid curve, contribution from the series $3p^3n\ell$; and (f) gray dashed curve, my RR data. The collisionally ionized zone is as recommended by Bryans *et al.* [204]. The photoionized zone is taken from Ref. [205].

[85] and Mazzotta *et al.* [123].

The calculated Maxwellian-averaged DR rate coefficients in both *LS*- and IC-coupling for Cr^{11+} are shown in n Fig. 4.20. The peak of the DR rate coefficient of Mewe *et al.* [85] is 23% lower than my DR rate coefficient performed in *LS*-coupling. The The DR rate coefficient of Mewe *et al.* [85] for V^{10+} was reproduced by using their fitting parameters in Table 4.1 and their Eq. (4.4). The peak of the DR rate coefficient of Landini and Fossi [89] is 13% lower than my DR rate coefficient performed in *LS*-coupling. I reproduced the DR rate coefficient of Landini and Fossi [89] for Cr^{11+} by using their fitting coefficients in
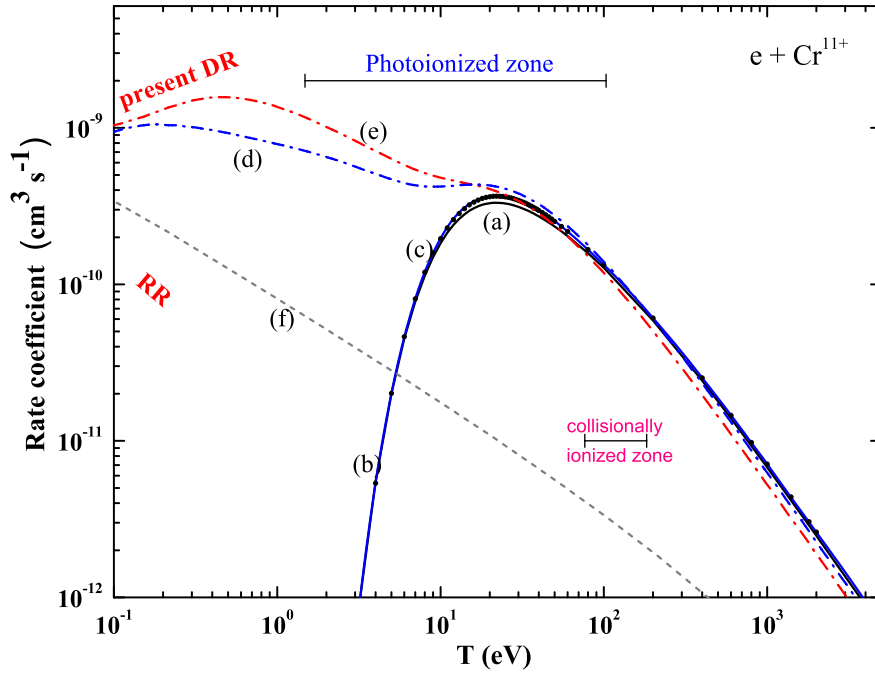
Figure 4.20 Maxwellian-averaged rate coefficients for Cr^{11+}: (a) black solid curve, DR data from the empirical formula of Mewe *et al.* [85]; (b) blue solid curve, recommended DR data by Mazzotta *et al.* [123]; (c) black circles, DR data from Landini and Fossi [89]; (d) blue dash-dotted curve, my DR data in *LS*-coupling; (e) red dash-dotted curve, my DR in IC-coupling; and (f) gray dashed curve, my RR data. The collisionally ionized zone is as recommended by Bryans *et al.* [204]. The photoionized zone is taken from Ref. [205].

Table 4.2. These fitting coefficients were derived by extrapolating the fitting work of Shull and Steenberg along the sequence [86]. As we can see from Fig. 4.20, the recommended DR rate coefficient of Mazzotta *et al.* [123] is identical to the DR rate coefficient of Landini and Fossi [89]. The little peak for the DR rate coefficient at 0.5 eV is due to the contribution of the $3s3p3dn\ell$ and $3p^3n\ell$ series.

Fig. 4.21 shows my Maxwellian-averaged DR rate coefficients in both *LS*- and IC-coupling schemes for Mn^{12+}. The peak of the DR rate coefficient of Mewe *et al.* [85] is 26% lower than my DR rate coefficient performed in *LS*-coupling. The The DR rate

Figure 4.21   Comparison of available DR rate coefficients for Mn^{12+}: (a) black solid curve, DR data from the empirical formula of Mewe *et al.* [85]; (b) blue solid curve, recommended DR data by Mazzotta *et al.* [123]; (c) black circles, DR data from Landini and Fossi [89]; (d) blue dash-dotted curve, my DR data in *LS*-coupling; (e) red dash-dotted curve, my DR data in IC-coupling; and (f) gray dashed curve, my RR data . The collisionally ionized zone is as recommended by Bryans *et al.* [204]. The photoionized zone is taken from Ref. [205].

coefficient of Mewe *et al.* [85] for Mn^{12+} was reproduced by using their fitting parameters

in Table 4.1 and their Eq. (4.4). The peak of the DR rate coefficient of Landini and Fossi

[89] is 16% lower than my DR rate coefficient performed in LS-coupling. I reproduced the

DR rate coefficient results of Landini and Fossi [89] by using their fitting coefficients in

Table 4.2, which were derived by extrapolating the DR fitting work of Shull and Steenberg

along the sequences [86]. The recommended DR rate coefficient of Mazzotta *et al.* [123]

are identical to the DR rate coefficient of Landini and Fossi [89]. The DR rate coefficients

of Mewe *et al.* [85], Landini and Fossi [89], and Mazzotta *et al.* [123] are missing contribu-

tions below 10 eV. Contributions at electron temperatures seen up to 1.0 eV are dominated

by both series $3s^2 3dn\ell$ and $3s3p3dn\ell$. A comparison to the experimental results for Fe^{13+}

is made to confirm the inadequacy of these previously existing data.
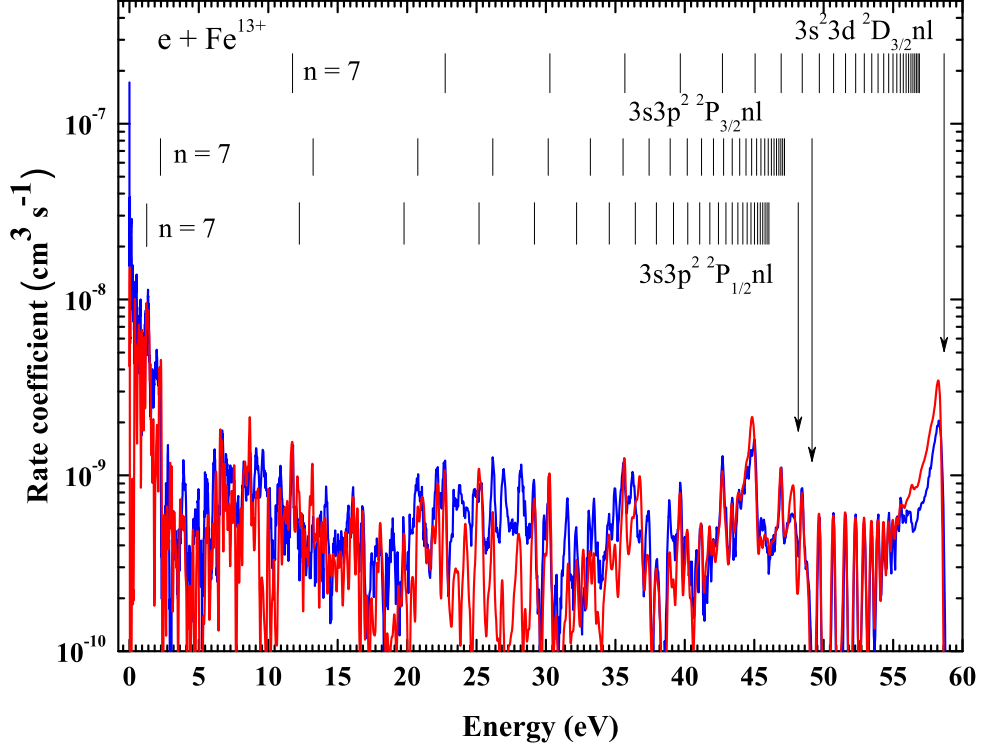
Figure 4.22 Comparisons of the DR rate coefficients with the TSR measured merged-beams electron-ion recombination rate coefficient (MBRRC) for Fe^{13+} from intra-shell $\Delta n_c = 0$ transitions: blue solid curve, experimental measurements by Schmidt *et al.* [76]; red solid curve, my multi-configuration Breit-Pauli calculation (MCBP). The expected DR resonance positions are represented by vertical bars using the hydrogenic Rydberg formula.

Test Storage Ring (TSR) measurements of Schmidt *et al.* [76] for Fe^{13+} do exist and a

comparison with my calculated MCBP DR rate coefficient for $\Delta n_c = 0$ core excitations is

shown in Fig. 4.22. A flattened Maxwellian was used to describe the electron cooler, char-

acterized by a transverse temperature of $kT_\perp = 12$ meV and a longitudinal temperature of

$kT_\parallel = 0.09$ meV, with respect to the ion beam direction in Eq. (2.78) [173]. There is poor
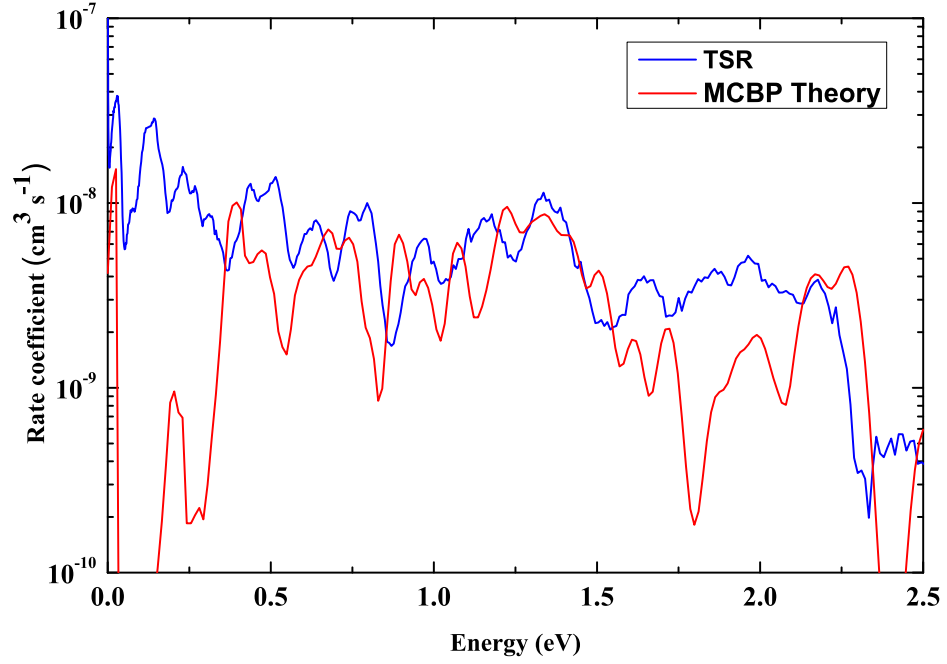
Figure 4.23   Same as Fig. 4.22, but for low energy.

agreement between theory and experiment at low energies (0.05 - 0.36 eV), where the mea-

sured DR rate coefficient is higher by an order of magnitude (see Fig. 4.23). The resonances

located at this energy range are members of the $3s^23p[^2P_{3/2}]n\ell$, $3s3p^2[^4P_{3/2}]9f$, $3s3p3d5g$,

$3p^23dn\ell$, and $3s3d^2n\ell$ series. Both DR rate coefficients drop at 2.34 eV, where autoioniza-

tion to $3s^23p[^2P_{3/2}]$ becomes energetically available. Good agreement is obtained up to 20

eV, while disagreement at the energy range $23-29$ eV is seen, where the measured rate

is higher. Contributions to the DR rate coefficient at this energy range are coming from

$3s \rightarrow 3p$ and $3p \rightarrow 3d$ core excitations. I think this may be due to correlations with higher

n-values ($n = 4$, and 5) are required. The $3s \rightarrow 3p$ core excitations have series limits at

48.169 eV for $3s3p^2[^2P_{1/2}]n\ell$ and 49.61 for $3s3p^2[^2P_{3/2}]n\ell$, while the $3p \rightarrow 3d$ core exci-

tations have limits of 58.672 eV for $3s^23d[^2D_{3/2}]n\ell$. Better agreement is obtained at higher

energies, where a hard cut-off at $n_{cut} = 95$ was used. The time of flight of $T_f = 166.5$ ns

was used in Eqs. (2.80) and (2.81) for the recombined series including up to $\ell = 8$, where

the recombined states can re-ionize while they are traveling from the electron cooler to the

charge-state analyzer by the motional electric field induced in the magnetic elements as in

Eq. (2.80). Overall, reasonable agreement is obtained except at the low energies below

0.35 eV.
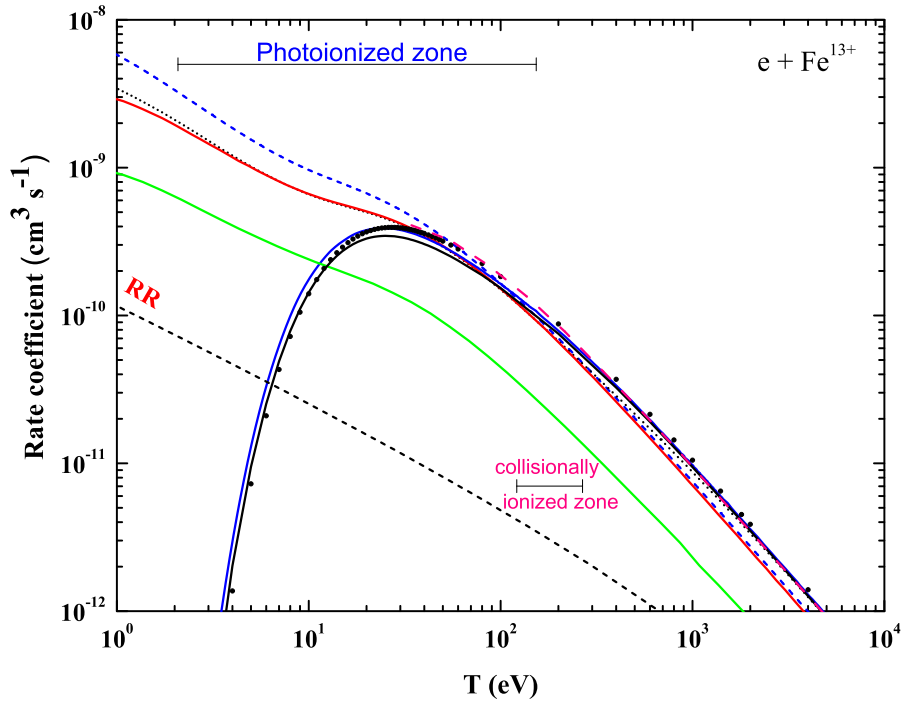
Figure 4.24   Maxwellian-averaged DR and RR rate coefficients for Fe^{13+}: blue dashed curve, Maxwellian-average DR rate coefficient for the experimental measurements of Schmidt *et al.* [76]; black dotted curve, DR calculations of Badnell [104]; red solid curve, my DR rate coefficient in IC-coupling; pink dashed curve, DR data of Jacobs *et al.* [191]; black circles, DR data fitting of Shull and Steenberg [86]; black solid curve, DR data from the empirical formula of Mewe *et al.* [85]; blue solid curve, recommended DR data by Mazzotta *et al.* [123]; green solid curve, total rate coefficient (RR + DR) using R-matrix by Nahar [130]; and gray dashed curve, my RR data. The collisionally ionized zone is as recommended by Bryans *et al.* [204]. The photoionized zone is taken from Ref. [205].

Fig. 4.24 shows a comparison between my calculated Maxwellian-averaged DR rate

coefficients in both LS- and IC-coupling and other available data for Fe^{13+}. The peak of the DR rate coefficient of Mewe *et al.* [85] is 23% lower than my DR rate coefficient performed in IC-coupling. The DR rate coefficient of Mewe *et al.* [85] for Fe^{13+} was reproduced by using their fitting parameters in Table 4.1 and their Eq. (4.4). The peak of the DR rate coefficients of Shull and Steenberg [86] are 11% lower than my DR rate coefficient performed in IC-coupling. This rate coefficient is reproduced by using the DR fitting parameters in Table 4.2 and using Eq. (4.3) and is based on the calculations of Jacobs *et al.* [191]. The recommended DR rate coefficient of Mazzotta *et al.* [123] is matching the rate coefficient of Shull and Steenberg [86], especially after 11 eV. The total rate coefficient (RR + DR) of Nahar [130] is obtained by using R-matrix method and is three times lower than my DR rate coefficient performed in IC-coupling. The DR rate coefficient of Badnell [104] is higher at high-electron temperatures since it includes the contributions from $\Delta n_c = 1$ ($n = 2 \rightarrow n = 3$ and $n = 3 \rightarrow n = 4$) core transitions.

Fig. 4.25 shows my Maxwellian-averaged rate coefficients for Co^{14+} in both *LS*- and IC-coupling. The peak of the DR rate coefficient of Mewe *et al.* [85] is 28% lower than my DR rate coefficient performed in IC-coupling. The DR rate coefficient of Mewe *et al.* [85] for Co^{14+} was reproduced by using their fitting parameters in Table 4.1 and their Eq. (4.4). The peak of the DR rate coefficient of Landini and Fossi is 19% lower than my DR rate coefficient performed in IC-coupling. The DR rate coefficient of Landini and Fossi was reproduced by using their DR fitting parameters in Tale 4.2 and using Eq. (4.3). They obtained these parameters by extrapolating the work of Shull and Steenberg [86]. The fitting work of Shull and Steenberg [86] is based on the work of Aldrovandi and
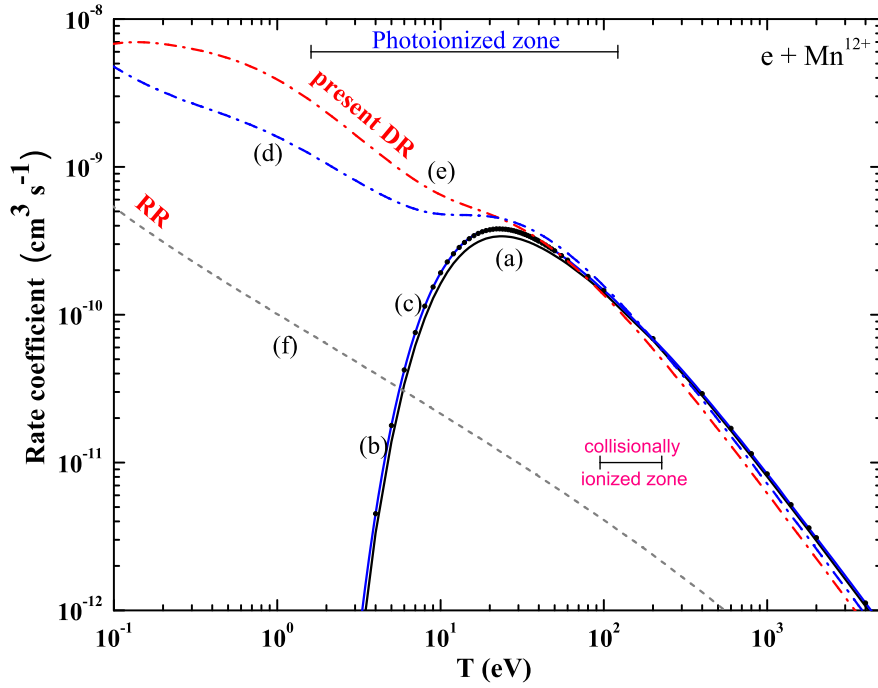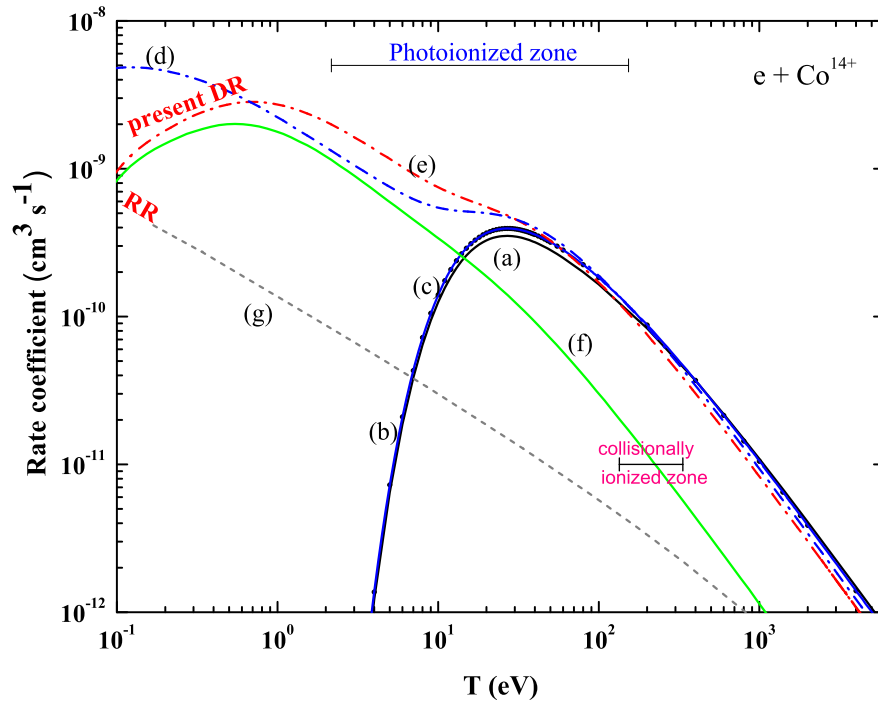
Figure 4.25 Maxwellian-averaged rate coefficients for Co^{14+}: (a) black solid curve, DR data from the empirical formula of Mewe *et al.* [85]; (b) blue solid curve, recommended DR data by Mazzotta *et al.* [123]; (c) black circles, DR data from Landini and Fossi [89]; (d) blue dash-dotted curve, my DR data in *LS*-coupling; (e) red dash-dotted curve, my DR data in IC-coupling; (f) green solid curve, contribution from the $3s3p3dn\ell$ series; and (g) gray dashed curve, my RR data . The collisionally ionized zone is as recommended by Bryans *et al.* [204]. The photoionized zone is taken from Ref. [205].

Péquignot [84], Jacobs *et al.* [127, 189, 190, 191]. The DR rate coefficient for Co^{14+} at the low electron temperatures below 1.0 eV is mainly due to the contribution of the $3s3p3dn\ell$ series.

The calculated Maxwellian-averaged DR rate coefficients for Ni^{15+} in both *LS*- and IC-coupling are shown in Fig. 4.26. The peak of the DR rate coefficient of Mewe *et al.* [85] is 26% lower than my DR rate coefficient performed in IC-coupling. The DR rate coefficient of Mewe *et al.* [85] for Ni^{14+} was reproduced by using their fitting parameters in Table 4.1 and their Eq. (4.4). The peak of the DR rate coefficient of Shull and Steenberg [86] is
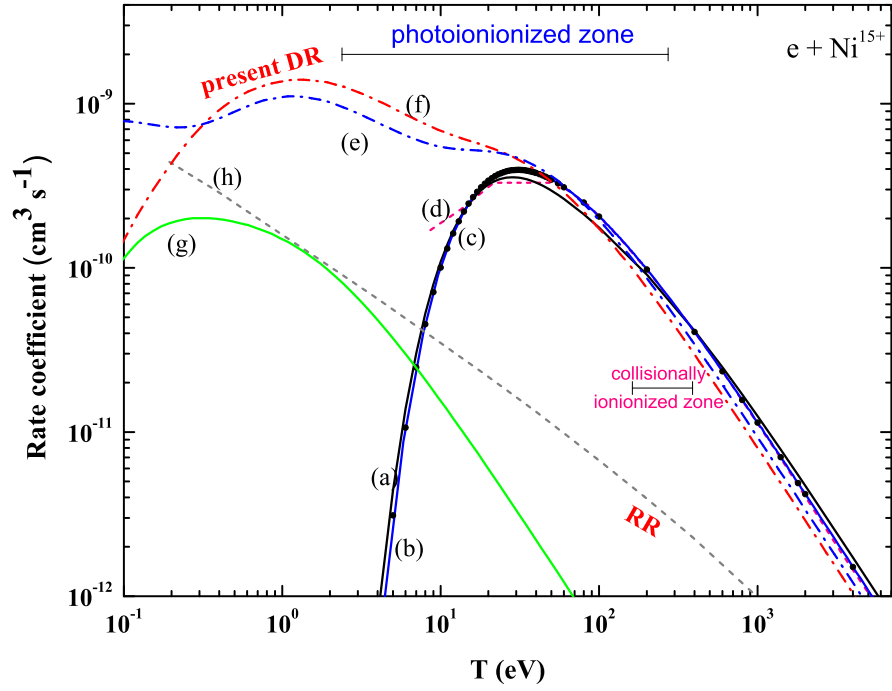
Figure 4.26 Maxwellian-averaged DR rate coefficients for Ni^{15+}: (a) black solid curve, DR data from the empirical formula of Mewe *et al.* [85]; (b) blue solid curve, recommended DR data by Mazzotta *et al.* [123]; (c) black circles, DR data of Shull and Steenberg [86]; (d) pink dashed curve, DR data of Jacobs *et al.* [190]; (e) blue dash-dotted curve, my DR data in *LS*-coupling; (f) red dash-dotted curve, my DR data in IC-coupling; and (g) green solid curve, contribution from the $3s^23pn\ell$ series; (h) gray dashed curve, my RR data. The collisionally ionized zone is as recommended by Bryans *et al.* [204]. The photoionized zone is taken from Ref. [205].

is 15% lower than my DR rate coefficient performed in IC-coupling. I reproduced the DR rate coefficient of Shull and Steenberg [86] from their DR parameters in Table 4.2 and by using Eq. (4.3). Their fitting work is based on Jacobs *et al.* [190], which is 30% lower than my DR rate coefficient performed in IC-coupling. The recommended DR rate coefficient of Mazzotta *et al.* [123] matches the rate coefficient of Shull and Steenberg [86]. The DR rate coefficient for Ni^{15+} at the low electron temperatures below 0.1 eV comes from the contribution of the $3s^23pn\ell$ series. The DR rate coefficient peak at 1 eV is due to contributions from $3s3p^2n\ell$, $3s^23dn\ell$, and $3s3p3dn\ell$ series.
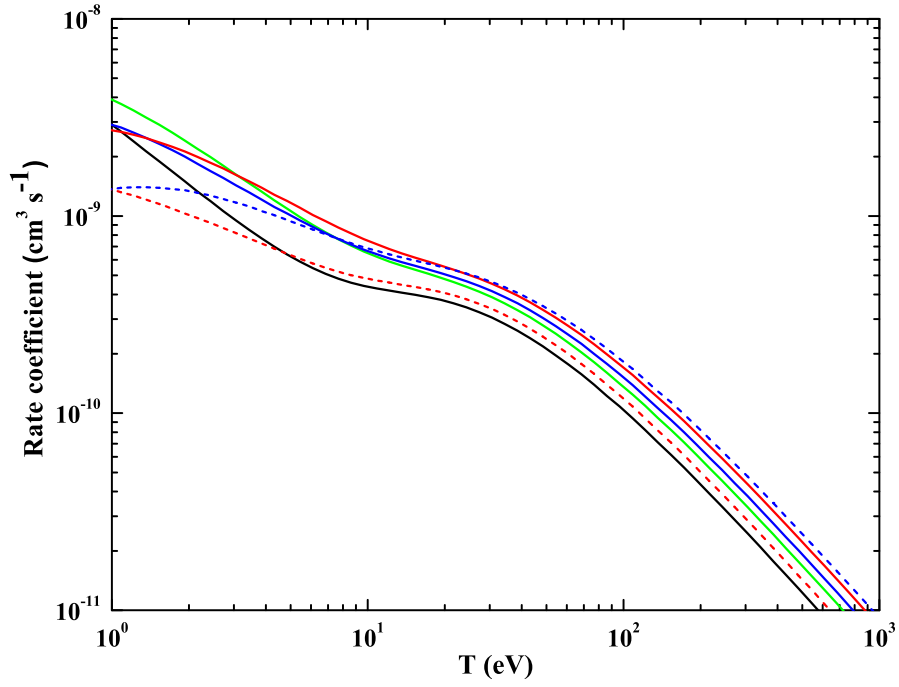
Figure 4.27 Maxwellian-averaged DR rate coefficients for the iron peak elements for $\Delta n_c = 0$ and $\Delta n_c = 1$ core excitations: black solid curve, DR for V^{10+}; red dashed curve, DR for Cr^{11+}; green solid curve, DR for Mn^{12+}; blue solid curve, DR for Fe^{13+}; red solid curve, DR for Co^{14+}; and blue dashed curve, DR for Ni^{15+}.

In Fig. 4.27, I present the calculated total Maxewllian-averaged DR rate coefficients ($\Delta n_c = 0$ and $\Delta n_c = 1$ core excitations) for iron peak elements. For the collisionally ionized electron temperature ranges, the total DR rate coefficients increase as the ionic charge q increases, while there is no systematic trend for the DR rate coefficients at the low-electron temperatures. Thus, extrapolations or interpolations are not recommended through the Al-like isoelectronic sequence and systematic calculations are required.

4.4.5 Aluminum-Like Copper and Zinc

In Table 4.10, comparisons between my lowest energy levels for Al-like Cu^{16+} and Zn^{17+} ions for $\Delta n_c = 0$ core excitations and the data taken from NIST, the perturba-

tion theory calculations (MR-MP) of Santana *et al.* [209], and the MCHF calculations of Froese-Fischer *et al.* [198], where very good agreement is obtained.
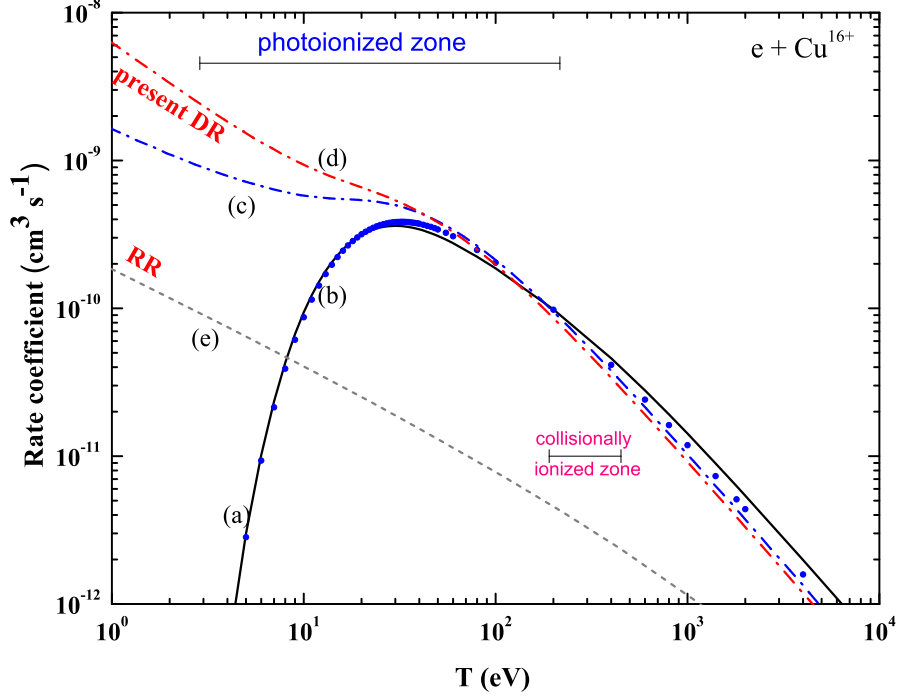
Figure 4.28   Maxwellian-averaged DR and RR rate coefficients for Cu^{16+}: (a) black solid curve, DR data from the empirical formula of Mewe *et al.* [85]; (b) blue circles, DR data from Mazzitelli and Mattioli [192]; (c) blue dash-dotted curve, my DR data in *LS*-coupling; (d) red dash-dotted curve, my DR data in IC-coupling; and (e) gray dashed curve, my RR data . The collisionally ionized zone is as recommended by Bryans *et al.* [204]. The photoionized zone is taken from Ref. [205].

My calculated Maxwellian-averaged DR rate coefficients for Al-like Cu^{16+} and Zn^{17+} ions are presented in Fig. 4.28 and Fig. 4.29, respectively. The DR rate coefficients of Mewe *et al.* were obtained by using their empirical formula in Eq. (4.4) and their fitting coefficients in Table 4.1 [85]. The DR rate coefficients of Mazzitelli and Mattioli were obtained by using their DR fitting coefficients in Table 4.3. Their DR rate coefficients were obtained by extrapolations through the isoelectronic sequences beyond Ni ions.
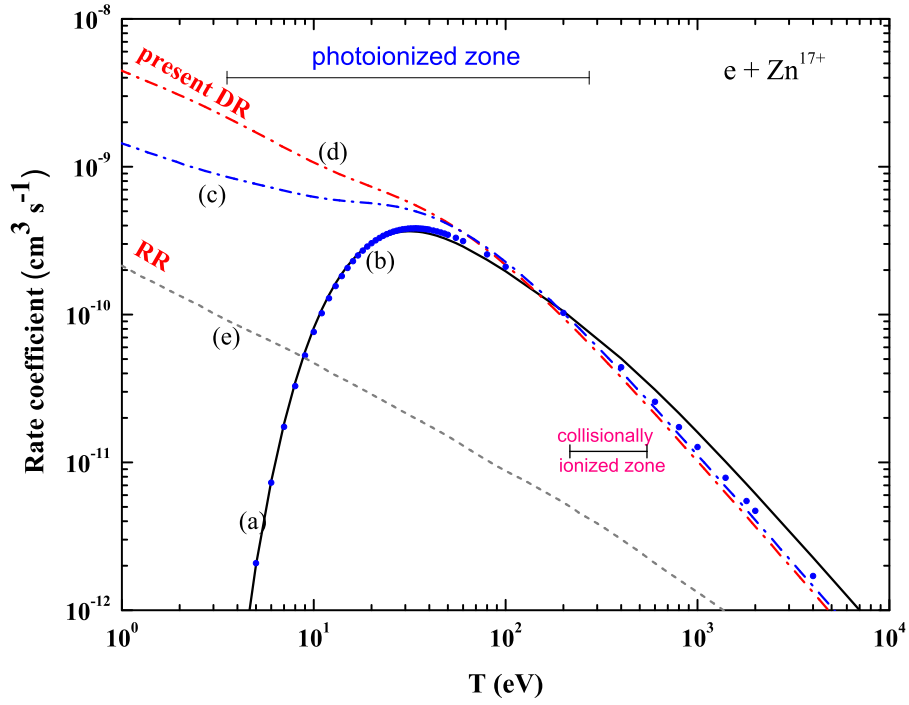
Figure 4.29 Maxwellian-averaged DR and RR rate coefficients for Zn^{17+}: (a) black solid curve, DR data from the empirical formula of Mewe *et al.* [85]; (b) blue circles, DR data from Mazzitelli and Mattioli [192]; (c) blue dash-dotted curve, my DR data in *LS*-coupling; (d) red dash-dotted curve, my DR data in IC-coupling; and (e) gray dashed curve, my RR data . The collisionally ionized zone is as recommended by Bryans *et al.* [204]. The photoionized zone is taken from Ref. [205].

The total DR rate coefficients $\Delta n_c = 0$ and $\Delta n_c = 1$ for the entire Al-like isoelectronic sequence are fitted using Eq. (4.6), with E_i and T are in units of K, and α^{DR} is in units of $cm^3 \, s^{-1}$. These fits are accurate to better than 5% for all the Al-like isoelectronic sequence in the electron temperature range $q^2(10 - 10^7)$ K, where q is the charge of the recombing ion. The accuracy is better than 1% over the collisionally ionized range. In Table 4.11, the total DR rate fitting coefficients for the Al-like isoelectronic sequence forming the Si-like ions are presented.

In Fig. 4.30, an overview of the total ground state RR rate coefficients for the Al-
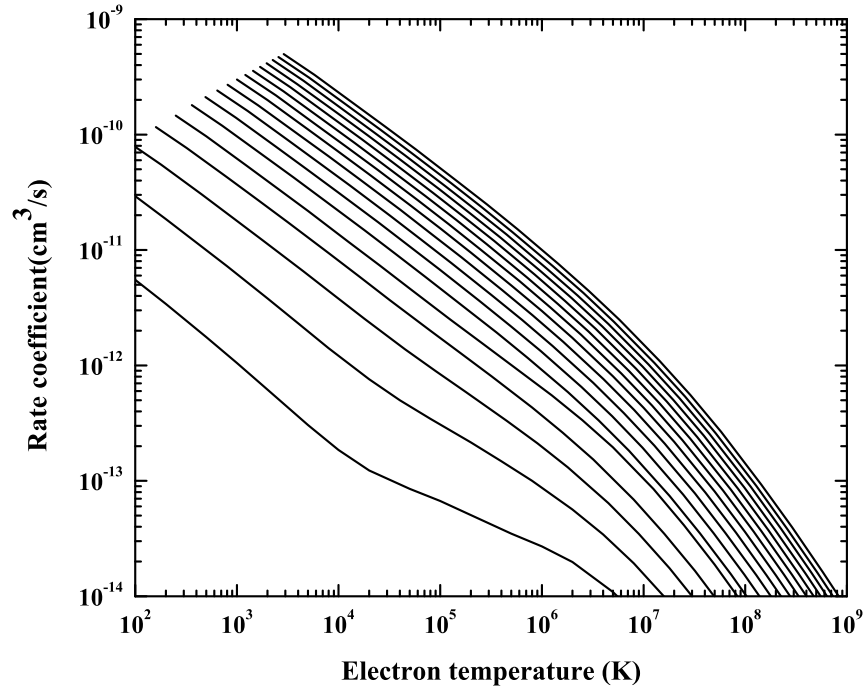
Figure 4.30 Total ground state RR rate coefficients for the Al-like isoelectronic sequence using the AUTOSTRUCTURE package. Curves from Si to Zn are shown from left to right.

like isoelectronic sequence are shown. At low charges (Si$^+$), the characteristic high-temperature bump is seen due to the highly non-hydrogenic screening of the wave functions for low-$n\ell$ states, in low-charge many-electron ions, which dominate the recombination at high temperatures. Table 4.12 presents the RR fitting coefficients for the initial ground and metastable states ($m = 1$ to $m = 5$), where $m = 1$ is the ground state of the Al-like ions ($3s^2 3p[^2P_{1/2}]$) and $m = 2$ is the first excited state ($3s^2 3p[^2P_{3/2}]$) and so on as can be figured out from Table 4.7.

The DR study of the Al-like isoelectronic sequence is closed with the following conclusions. Previous DR data were obtained either by using empirical formulas or were performed in a non-relativistic *LS*-coupling framework. The commonly used database of Mazzotta *et al.* [123] was generated by fitting these previous data, but it was not clear from

107

which sources they obtained their data [123]. Through this study, these sources were identified for most of the Al-like isoelectronic sequence. My results for S^{3+}, agreed very well with the previously existing results of Badnell [128]. A further study of the DR rate coefficients for S^{3+} in IC-coupling stressed the importance of the fine structure effects on the DR study. The DR rate coefficient performed in IC-coupling was higher than the DR rate coefficient performed in *LS*-couplin at low-electron temperatures due to the fine structure series that can autoionize to the ground state of S^{3+}, which does not exist in a non-relativistic *LS* treatment. On the other hand, for higher-electron temperatures, the DR rate coefficient obtained in IC-coupling was lower due to the doubly-excited states that can radiatively decay to autoionizing states for $n \geq 36$. Thus IC-coupling calculations are required for this isoelectronic sequence. My work on S^{3+} was published by Abdel-Naby *et al.* [207].

Calculations for the DR rate coefficient have been carried out for the entire Al-like isoelectronic sequence in both *LS*- and IC-coupling. Comparisons of my present DR rate coefficients in IC-coupling versus the existing *LS*-results or the DR rates of Mazzotta *et al.* [123] were found to differ by orders of magnitudes at the low-electron temperatures since they did not include the fine structure splitting. This was confirmed by a comparison to the measurements from the Heidelberg heavy-ion Test Storage Ring facility of Schmidt *et al.* [76], where my DR rate coefficient at low-electron temperatures is comparable to the experimental results. The DR and RR rate coefficients were then fitted with simple formulas for efficient dissemination of data and ease of use in plasma modeling codes. These results for the Al-like sequence are in preparation for publications [210].

Table 4.11 Fitting coefficients c_i and E_i for Eq. (4.6) for the total DR rate coefficients of the ground Al-like isoelectronic sequence forming the Si-like ions. All coefficients refer to my IC-coupling calculations. $X(Y)$ means $X \times 10^Y$.

ion	c_1	c_2	c_3	c_4	c_5	c_6
Si^+	3.463(-08)	1.934(-07)	1.652(-07)	6.273(-06)	5.465(-05)	4.103(-03)
P^{2+}	1.399(-07)	1.809(-06)	2.659(-06)	1.362(-05)	4.795(-04)	1.202(-02)
S^{3+}	5.817(-07)	1.391(-06)	1.123(-05)	1.521(-04)	1.875(-03)	2.097(-02)
Cl^{4+}	1.399(-06)	1.371(-05)	1.215(-04)	1.183(-03)	4.048(-02)	$\cdots$
Ar^{5+}	1.136(-05)	1.302(-04)	8.017(-04)	4.318(-02)	7.582(-03)	7.582(-03)
K^{6+}	2.674(-04)	4.405(-04)	2.397(-03)	6.775(-02)	4.313(-03)	4.313(-03)
Ca^{7+}	2.978(-04)	7.585(-04)	5.973(-03)	8.950(-02)	2.076(-03)	2.078(-03)
Sc^{8+}	2.469(-04)	1.117(-03)	4.082(-03)	6.220(-02)	5.721(-02)	$\cdots$
Ti^{9+}	3.790(-04)	1.098(-03)	7.060(-03)	9.301(-02)	5.030(-02)	$\cdots$
V^{10+}	1.890(-03)	4.228(-03)	9.756(-03)	1.225(-01)	4.594(-02)	$\cdots$
Cr^{11+}	5.673(-04)	4.535(-03)	1.811(-02)	1.522(-01)	4.117(-02)	$\cdots$
Mn^{12+}	3.619(-03)	8.488(-03)	2.212(-02)	1.824(-01)	3.920(-02)	$\cdots$
Fe^{13+}	2.305(-03)	1.072(-02)	3.512(-02)	2.105(-01)	3.622(-02)	$\cdots$
Co^{14+}	2.468(-03)	1.431(-02)	4.235(-02)	2.450(-01)	4.216(-02)	$\cdots$
Ni^{15+}	1.625(-03)	1.378(-02)	5.373(-02)	2.721(-01)	4.276(-02)	$\cdots$
Cu^{16+}	7.414(-03)	1.566(-02)	7.305(-02)	3.055(-01)	4.986(-02)	$\cdots$
Zn^{17+}	5.463(-03)	2.664(-02)	8.918(-02)	3.348(-01)	6.397(-02)	$\cdots$

ion	E_1	E_2	E_3	E_4	E_5	E_6
Si^+	2.411(+01)	1.289(+02)	4.201(+02)	1.009(+04)	5.042(+04)	1.291(+05)
P^{2+}	1.997(+02)	5.684(+02)	2.420(+03)	1.511(+04)	7.690(+04)	1.606(+05)
S^{3+}	3.628(+02)	1.058(+03)	7.160(+03)	3.260(+04)	1.235(+05)	2.070(+05)
Cl^{4+}	5.776(+02)	2.707(+03)	1.065(+04)	6.346(+04)	2.407(+05)	$\cdots$
Ar^{5+}	7.953(+02)	7.596(+03)	3.505(+04)	2.299(+05)	4.576(+05)	4.576(+05)
K^{6+}	2.667(+03)	8.588(+03)	5.812(+04)	2.807(+05)	6.088(+05)	6.088(+05)
Ca^{7+}	3.540(+03)	1.530(+04)	7.536(+04)	3.313(+05)	8.562(+05)	8.562(+05)
Sc^{8+}	6.596(+02)	6.965(+03)	4.220(+04)	2.481(+05)	5.378(+05)	$\cdots$
Ti^{9+}	8.123(+02)	8.315(+03)	4.990(+04)	3.000(+05)	6.558(+05)	$\cdots$
V^{10+}	1.324(+03)	9.205(+03)	6.872(+04)	3.450(+05)	8.177(+05)	$\cdots$
Cr^{11+}	3.088(+03)	1.472(+04)	7.630(+04)	3.956(+05)	9.864(+05)	$\cdots$
Mn^{12+}	2.073(+03)	1.548(+04)	9.187(+04)	4.434(+05)	1.265(+06)	$\cdots$
Fe^{13+}	4.747(+03)	1.877(+04)	1.190(+05)	5.090(+05)	1.595(+06)	$\cdots$
Co^{14+}	5.617(+03)	2.330(+04)	1.259(+05)	5.619(+05)	1.982(+06)	$\cdots$
Ni^{15+}	8.084(+03)	3.157(+04)	1.497(+05)	6.139(+05)	2.428(+06)	$\cdots$
Cu^{16+}	2.345(+03)	2.556(+04)	1.636(+05)	6.788(+05)	2.789(+06)	$\cdots$
Zn^{17+}	3.634(+03)	3.351(+04)	1.835(+05)	7.410(+05)	3.102(+06)	$\cdots$

Table 4.12 RR fitting coefficients for the ground and metastable initial levels ($m = 1 - 5$) for Al-like ions using Eq. (4.7). $X(Y)$ means $X \times 10^Y$.

ion	m	A	B	T_0	T_1	C	T_2	ion	m	A	B	T_0	T_1	C	T_2
Si$^+$	1	3.501(-11)	0.6344	1.410(+1)	4.343(+7)	0.2248	5.831(+4)	V^{10+}	1	4.244(-10)	0.6487	8.751(+2)	3.451(+7)	0.0285	8.744(+4)
	2	5.985(-13)	0.2381	1.089(+4)	1.729(+7)	0.8233	4.020(+4)		2	1.627(-11)	0.5367	1.637(+5)	4.448(+7)	0.0366	1.140(+9)
	3	2.152(-11)	0.9649	1.545(+0)	1.528(+6)	0.3331	2.933(+5)		3	1.006(-10)	0.9380	1.192(+3)	1.984(+7)	0.0744	2.950(+3)
	4	2.154(-11)	0.9643	1.546(+0)	1.552(+6)	0.3316	2.927(+5)		4	9.994(-11)	0.9390	1.183(+3)	2.022(+7)	0.0732	3.276(+3)
	5	9.959(-14)	0.0012	6.859(+4)	8.113(+6)	1.6259	9.307(+4)		5	4.097(-11)	0.4298	9.074(+3)	3.013(+7)	0.4880	3.481(+3)
P^{2+}	1	1.348(-10)	0.6342	1.410(+1)	2.213(+7)	0.1784	4.692(+4)	Cr^{11+}	1	5.256(-10)	0.6587	8.457(+2)	3.709(+7)	0.0217	9.474(+4)
	2	1.249(-12)	0.0601	2.931(+4)	1.141(+7)	0.9362	2.880(+4)		2	1.722(-11)	0.5271	2.064(+5)	4.872(+7)	0.0321	1.358(+9)
	3	2.368(-11)	1.0332	7.367(+0)	1.027(+7)	0.1323	1.864(+4)		3	3.823(-11)	0.6279	1.385(+4)	2.345(+7)	0.3505	2.555(+3)
	4	2.363(-11)	1.0331	7.396(+0)	1.025(+7)	0.1325	1.864(+4)		4	3.823(-11)	0.6279	1.385(+4)	2.345(+7)	0.3505	2.555(+3)
	5	2.600(-10)	1.0270	5.518(-2)	1.346(+7)	0.0843	1.895(+4)		5	4.340(-11)	0.3872	1.292(+4)	3.267(+7)	0.5146	3.812(+3)
S^{3+}	1	2.664(-10)	0.6896	2.107(+1)	2.028(+7)	0.0840	6.752(+4)	Mn^{12+}	1	5.330(-10)	0.6471	1.146(+3)	4.169(+7)	0.0236	1.013(+5)
	2	2.037(-12)	0.0000	8.032(+4)	2.377(+7)	0.6629	4.283(+4)		2	8.228(-12)	0.0000	1.210(+6)	9.275(+7)	0.1636	1.043(+6)
	3	3.990(-11)	1.0288	2.885(+1)	9.662(+6)	0.0760	2.067(+4)		3	3.881(-11)	0.5895	1.880(+4)	2.668(+7)	0.3827	3.531(+3)
	4	3.990(-11)	1.0288	2.885(+1)	9.662(+6)	0.0760	2.067(+4)		4	3.881(-11)	0.5895	1.880(+4)	2.668(+7)	0.3827	3.531(+3)
	5	2.095(-09)	1.0125	1.002(-2)	1.294(+7)	0.0378	1.793(+4)		5	4.538(-11)	0.3885	1.595(+4)	3.601(+7)	0.5147	4.487(+3)
Cl^{4+}	1	3.996(-10)	0.7062	3.177(+1)	2.018(+7)	0.0467	8.299(+4)	Fe^{13+}	1	5.370(-10)	0.6338	1.531(+3)	4.632(+7)	0.0278	9.070(+4)
	2	2.950(-12)	0.0000	1.387(+5)	3.410(+7)	0.4928	6.877(+4)		2	8.622(-12)	0.0000	1.459(+6)	1.003(+8)	0.1494	1.457(+6)
	3	5.362(-10)	1.0184	6.138(-1)	1.257(+7)	0.0265	2.431(+4)		3	4.474(-11)	0.4792	2.200(+4)	2.966(+7)	0.4683	3.641(+3)
	4	4.837(-10)	1.0184	7.570(-1)	1.260(+7)	0.0268	2.337(+4)		4	4.428(-11)	0.6068	1.966(+4)	2.807(+7)	0.3725	3.529(+3)
	5	4.745(-11)	0.9944	9.020(+1)	1.461(+7)	0.0478	7.954(+3)		5	4.938(-11)	0.3881	1.843(+4)	3.891(+7)	0.5164	5.474(+3)
Ar^{5+}	1	4.137(-10)	0.7064	6.853(+1)	2.108(+7)	0.0316	1.020(+5)	Co^{14+}	1	6.045(-10)	0.6412	1.616(+3)	4.963(+7)	0.0223	1.249(+5)
	2	2.076(-11)	0.7485	7.323(+3)	2.159(+7)	0.0316	3.418(+8)		2	9.072(-12)	0.0000	1.711(+6)	1.074(+8)	0.1402	1.730(+6)
	3	2.527(-10)	1.0167	8.983(+0)	1.306(+7)	0.0172	1.780(+4)		3	4.963(-11)	0.5071	2.299(+4)	3.173(+7)	0.4475	3.840(+3)
	4	2.641(-10)	1.0168	8.213(+0)	1.289(+7)	0.0172	1.901(+4)		4	5.035(-11)	0.5127	2.230(+4)	3.168(+7)	0.4426	3.744(+3)
	5	1.861(-11)	0.6489	2.225(+3)	1.744(+7)	0.3318	1.298(+3)		5	1.258(-09)	1.0283	2.566(+1)	2.239(+7)	0.0444	2.157(+8)
K^{6+}	1	4.328(-10)	0.6985	1.259(+2)	2.237(+7)	0.0271	1.033(+5)	Ni^{15+}	1	6.334(-10)	0.6317	1.936(+3)	5.428(+7)	0.0256	1.048(+5)
	2	2.100(-11)	0.7104	1.497(+4)	2.373(+7)	0.0303	3.331(+8)		2	9.256(-12)	0.0000	2.080(+6)	1.120(+8)	0.1274	2.596(+6)
	3	2.927(-10)	1.0172	1.452(+1)	1.353(+7)	0.0152	1.462(+4)		3	5.124(-11)	0.5416	2.723(+4)	3.411(+7)	0.4204	4.005(+3)
	4	3.074(-10)	1.0179	1.262(+1)	1.373(+7)	0.0158	1.870(+4)		4	5.151(-11)	0.4597	2.811(+4)	3.550(+7)	0.4859	4.854(+3)
	5	2.317(-11)	0.6127	3.066(+3)	1.897(+7)	0.3608	1.702(+3)		5	1.780(-09)	1.0307	1.590(+1)	2.404(+7)	0.0414	2.166(+8)
Ca^{7+}	1	4.279(-10)	0.6860	2.289(+2)	2.459(+7)	0.0262	9.582(+4)	Cu^{16+}	1	5.858(-10)	0.6135	2.836(+3)	6.013(+7)	0.0317	1.033(+5)
	2	1.862(-11)	0.6624	3.392(+4)	2.753(+7)	0.0283	3.671(+8)		2	9.564(-12)	0.0000	2.439(+6)	1.161(+8)	0.1206	3.239(+6)
	3	3.125(-09)	1.0120	2.393(-1)	1.550(+7)	0.0079	1.024(+4)		3	2.960(-10)	1.0431	9.572(+2)	2.076(+7)	0.0667	1.245(+8)
	4	4.480(-10)	1.0138	1.208(+1)	1.516(+7)	0.0110	1.214(+4)		4	5.146(-11)	0.5187	3.575(+4)	3.596(+7)	0.4417	5.281(+3)
	5	2.892(-11)	0.4841	4.257(+3)	2.260(+7)	0.4515	1.922(+3)		5	5.332(-11)	0.3476	3.575(+4)	4.969(+7)	0.5441	7.563(+3)
Sc^{8+}	1	4.952(-10)	0.6887	2.874(+2)	2.679(+7)	0.0192	1.075(+5)	Zn^{17+}	1	7.187(-10)	0.6349	2.440(+3)	6.073(+7)	0.0221	1.534(+5)
	2	1.878(-11)	0.6351	5.494(+4)	3.071(+7)	0.0363	5.128(+8)		2	9.719(-12)	0.0000	2.896(+6)	1.258(+8)	0.0991	4.624(+6)
	3	8.650(-11)	0.9903	6.081(+2)	1.599(+7)	0.0368	3.842(+3)		3	3.276(-10)	1.0369	9.099(+2)	2.486(+7)	0.0589	1.557(+8)
	4	8.656(-11)	0.9905	6.058(+2)	1.605(+7)	0.0365	3.497(+3)		4	2.969(-10)	1.0391	1.109(+3)	2.449(+7)	0.0608	1.484(+8)
	5	3.353(-11)	0.4908	5.286(+3)	2.409(+7)	0.4483	2.402(+3)		5	5.350(-11)	0.3438	4.561(+4)	5.213(+7)	0.5488	8.640(+3)
Ti^{9+}	1	6.008(-10)	0.6876	3.176(+2)	2.946(+7)	0.0162	8.938(+4)								
	2	1.768(-11)	0.5850	9.609(+4)	3.726(+7)	0.0367	8.356(+8)								
	3	3.359(-11)	0.7686	7.365(+3)	1.911(+7)	0.2317	2.128(+3)								
	4	9.553(-11)	0.9332	8.792(+2)	1.845(+7)	0.0744	2.876(+3)								
	5	3.803(-11)	0.4213	7.284(+3)	2.757(+7)	0.4922	2.848(+3)								

CHAPTER V

K-SHELL PHOTOABSORPTION FOR MAGNESIUM IONS

5.1 Introduction

There is a demand for accurate data for inner shell processes such as excitation and ionization, especially after the huge advances in the spectral resolutions of the launched X-ray telescopes. Such data are used for modeling astrophysical plasmas, interpreting the observed spectra from distant cosmic emitters, and determining the elemental abundances of the interstellar medium (ISM). Spectra of K-shell processes were observed from all ionic stages of the most abundant elements between oxygen and nickel [211]. An interesting study of K-shell photoionization and electron impact excitations of Fe^{16+} - Fe^{22+} has been carried out by Bautista *et al.* [212], followed by photoionization cross section calculations for the lower ionic stages of iron ions [213]. A series of successful K-shell photoabsorption calculations were carried out at Western Michigan University (WMU) for argon [138], oxygen [135], and neon [133]. These calculations were also used as an application to *Chandra* high-resolution spectroscopic observations for oxygen ions [134, 136] and neon ions [132]. Recently, I have been involved in the calculations for the K-shell photoabsorption for carbon ions [137].

I extend the efforts for the K-shell photoabsorption studies to magnesium ions. While I was performing these calculations, in late 2009 Witthoeft *et al.* [140] presented K-shell photoionization and photoabsorption calculations for Mg^{2+} - Mg^{9+} using the Breit-Pauli R-matrix method (BPRM). Thus, comparisons between these two results for multiply ion-

111

ized Mg^{6+}, Mg^{3+}, and Mg^{2+} ionic stages will be presented and I conclude my study by presenting a further calculation for neutral magnesium.

The rest of this Chapter is organized as follows. In Sec. 5.2, the methodology for calculating the K-shell photoabsorption cross sections is presented, while in Sec. 5.3 the results for Mg ions are discussed.

5.2 Methodology

The K-shell photo-excitation of the ground states of Mg ions up to Ne-like (Mg^{2+} - Mg^{9+}) can be represented as initial $1s \rightarrow np$ photoabsorption,

$$h\nu + 1s^2 2\ell^w \rightarrow 1s 2\ell^w np, \tag{5.1}$$

followed by two competing decay routes. The first one is called *participator* Auger decay which can be represented as

$$1s 2\ell^w np \rightarrow 1s^2 2\ell^{w-1} + e^-, \tag{5.2}$$

where the valence electron np participates in the autoionization process with a decay rate that scales as $1/n^3$ and goes to zero near the K-shell threshold. These channels are included in the R-matrix calculations. The second route is the *spectator* Auger decay which can be represented as

$$1s 2\ell^w np \rightarrow 1s^2 2\ell^{w-2} np + e^-, \tag{5.3}$$

where the valence electron np does not participate in the autoionization process, giving instead a decay width that is independent of n. Therefore, it is the dominant decay route

112

as $n \to \infty$ and gives a smooth cross section as the K-shell threshold is approached; above each threshold, K-shell photoionization to the $1s2\ell^w$ states occurs instead.

The important spectator Auger broadening are accounted for via an optical potential approach [138]. The target energy for each closed channel $1s2\ell^w np$ is modified within a multi-channel quantum defect theory (MQDT) approach as

$$E_{1s2\ell^w} \to E_{1s2\ell^w} - i\frac{\Gamma_{1s2\ell^w}}{2}, \qquad (5.4)$$

where $\Gamma_{1s2\ell^w}$ is the $1s2\ell^w \to 1s^22\ell^{w-2} + e^-$ Auger width. This enhanced R-matrix method was shown to be successful in describing experimental synchrotron measurements for argon [138], oxygen [135], and neon [133]. We compute the $1s2\ell^w$ Auger widths by applying the Smith time-delay method [181] to the photoabsorption R-matrix calculation of the neighboring $1s^22\ell^{w-1}$ magnesium ion (see Sec. 2.7.1). Since $1s \to 2p$ photoabsorption of the $1s^22\ell^{w-1}$ ion gives an intermediate $1s2\ell^w$ resonance, the subsequent Auger decay to the $1s^22\ell^{w-2} + e^-$ channel can be analyzed to obtain the Auger width.

It is also important to obtain accurate target wave functions using a single orthogonal orbital basis, and this is problematic since orbital relaxation occurs when the $1s^22\ell^{w-1}$ states are excited to the $1s2\ell^w$ K-shell-vacancy states (the 2ℓ electrons are now only screened by one, not two, $1s$ electrons). We account for orbital relaxation by using additional pseudo-orbitals as follows. A basis of physical $1s$, $2s$, and $2p$ orbitals is first constructed by performing Hartree-Fock (HF) [159] calculations for the $1s^22\ell^{w-1}$ ground states. Then a multiconfiguration Hartree-Fock calculation (MCHF) [160] is performed for the lowest $1s2\ell^w$ K-shell-excited states, including all configurations obtained from single and double promo-

tions to the $n = 3$ shell, to obtain $\overline{3s}$, $\overline{3p}$, and $\overline{3d}$ pseudo-orbitals. All target states are then described by a configuration-interaction (CI) expansion using all configurations consistent with single and double promotions out of the $1s^2 2\ell^{w-1}$ and $1s2\ell^w$ states, using the six $1s$, $2s$, $2p$, $\overline{3s}$, $\overline{3p}$, and $\overline{3d}$ orbitals.

5.3   K-Shell Photoabsorption Results

5.3.1   K-Shell Photoabsorption for Mg^{6+}

The inner-shell photoexcitation of the ground state of Mg^{6+} is obtained as follows.

$$h\nu + 1s^2 2s^2 2p^2[^3P] \; \rightarrow \; 1s2s^2 2p^2[^4P, \, ^2D, \, ^2P, \, ^2S]np[^3D, \, ^3P, \, ^3S]^o. \qquad (5.5)$$

The participator and spectator Auger transitions are obtained as follows:

$$1s2s^2 2p^2 np$$

participator Auger $\nearrow$	$\searrow$ spectator Auger
$1s^2 2s^2 2p + e^- \leftarrow$	$\rightarrow 1s^2 2s^2 np + e^-$
$1s^2 2s 2p^2 + e^- \leftarrow$	$\rightarrow 1s^2 2s2pnp + e^-$
$1s^2 2p^3 + e^- \leftarrow$	$\rightarrow 1s^2 2p^2 np + e^-.$

The physical $1s$, $2s$, and $2p$ orbitals are first generated by performing a Hartree-Fock (HF) [159] calculation for the ground state of Mg^{7+} ($1s^2 2s^2 2p[^2P]$). Then, a multiconfiguration Hartree-Fock (MCHF) [160] calculation is performed for the $1s2s^2 2p^2[^4P]$ K-shell excited state. Single and double promotions to the $n = 3$ shell to obtain the $\overline{3s}$, $\overline{3p}$, and $\overline{3d}$ pseudo-orbitals account for orbital relaxation effects due to the $1s$-vacancy. A summary for the optimization procedure is presented in Table 5.1.

114

Table 5.1 Methodology of determining the physical $1s$, $2s$, and $2p$ orbitals and correlation (or pseudo) $\overline{3s}$, $\overline{3p}$, and $\overline{3d}$ orbitals for Mg^{7+}.

$1s$, $2s$, and $2p$	From a HF (single-configuration) calculation for the $1s^2 2s^2 2p[^2P]$ term.
$\overline{3s}$, $\overline{3p}$, and $\overline{3d}$	From a MCHF (multiconfiguration) calculation for the lowest K-shell vacancy $1s 2s^2 2p^2[^4P]$ term including single and double $n=1 \to n=3$ promotions.
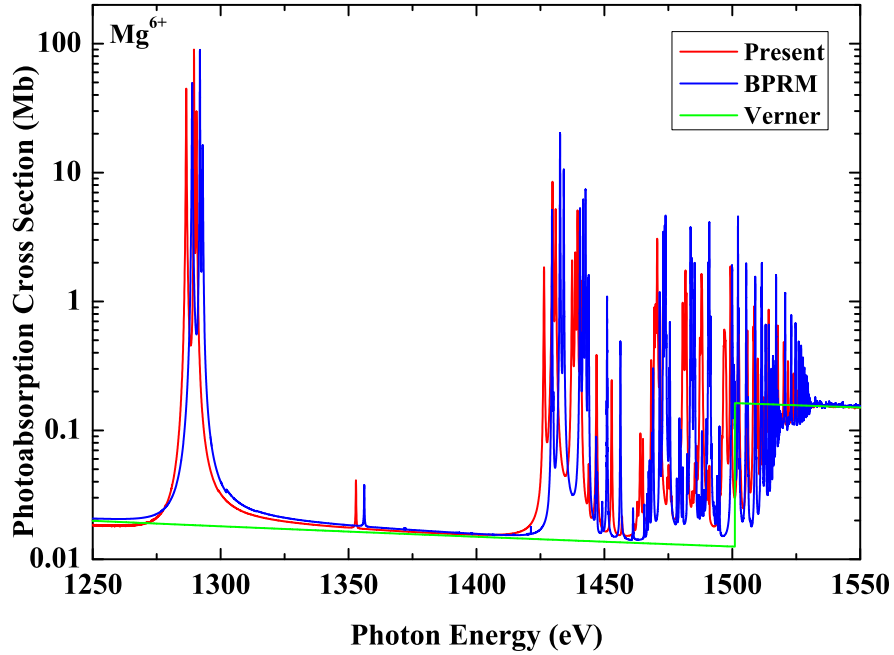
Figure 5.1 Comparisons of my calculated K-shell photoabsorption cross section for Mg^{6+}, the results of Witthoeft *et al.* [140] obtained by using the Breit Pauli R-matrix method (BPRM), and the photoionization results of Verner *et al.* [214].

In Table 5.2, a comparison of my R-matrix results of the target energies with the results obtained from another theoretical MCBP calculations using AUTOSTRUCTURE, and the available data taken from NIST for Mg^{6+} and Mg^{7+}, respectively. Overall, good agreement between these results is obtained.

In Table 5.3, the calculated Auger widths of the lowest 17 autoionizing Mg^{7+} target

115

Table 5.2 Comparison of term energies (in Rydbergs) for Mg^{6+} and Mg^{7+} for the states included in my calculations relative to the $1s^2 2s^2 2p\,(^2P)$ ground state of Mg^{7+}.

| | State | Term Energy (Ryd) | | |
		Present[a]	AUTO[b]	OTHER[c]
1	$1s^2 2s^2 2p^2\,(^3P)$	-16.5579	-16.4238	-16.539
2	$1s^2 2s^2 2p\,(^2P)$	0.0000	0.0000	0.0201
3	$1s^2 2s 2p^2\,(^4P)$	1.1451	1.1281	1.1999
4	$1s^2 2s 2p^2\,(^2D)$	2.1005	2.1267	2.11676
5	$1s^2 2s 2p^2\,(^2S)$	2.7687	2.7038	2.71815
6	$1s^2 2s 2p^2\,(^2P)$	2.9011	2.9600	2.91656
7	$1s^2 2p^3\,(^4S)$	3.7144	3.6865	3.76909
8	$1s^2 2p^3\,(^2D)$	4.2246	4.2702	4.24445
9	$1s^2 2p^3\,(^2P)$	4.8198	4.8169	4.78213
10	$1s 2s^2 2p^3\,(^3D)$	94.5583	94.5606	
11	$1s 2s^2 2p^3\,(^3S)$	94.7810	94.7236	
12	$1s 2s^2 2p^3\,(^3P)$	94.8530	94.7850	
13	$1s 2s^2 2p^2\,(^4P)$	94.9294	95.0231	
14	$1s 2s^2 2p^2\,(^2D)$	95.6410	95.6978	
15	$1s 2s^2 2p^2\,(^2P)$	95.8064	95.8232	
16	$1s 2s^2 2p^2\,(^2S)$	96.0802	96.0404	
17	$1s 2s(^3S) 2p^3\,(^4D)$	96.5659	96.6016	
18	$1s 2s(^1S) 2p^3\,(^4S)$	96.6427	96.6066	
19	$1s 2s(^3S) 2p^3\,(^4P)$	97.0262	97.0107	
20	$1s 2s(^1S) 2p^3\,(^2D)$	97.5674	97.6081	
21	$1s 2s(^3S) 2p^3\,(^4S)$	97.8702	98.0119	
22	$1s 2s(^1S) 2p^3\,(^2P)$	98.0284	98.0183	
23	$1s 2s(^3S) 2p^3\,(^2D)$	98.1166	98.2379	
24	$1s 2s(^3S) 2p^3\,(^2P)$	98.5875	98.6480	
25	$1s 2s(^3S) 2p^3\,(^2S)$	98.6118	98.6772	
26	$1s 2p^4\,(^4P)$	99.1148	99.1586	
27	$1s 2p^4\,(^2D)$	99.7499	99.8361	
28	$1s 2p^4\,(^2P)$	99.9272	99.9600	
29	$1s 2p^4\,(^2S)$	100.6980	100.7207	

[a] Present R-matrix results.

[b] MCBP AUTOSTRUCTURE results [32, 186].

[c] NIST data.

states (in eV) using R-matrix calculations [181] are presented. Comparisons with the re-

sults obtained by using the MCBP method of AUTOSTRUCTURE [32, 186] and the avail-
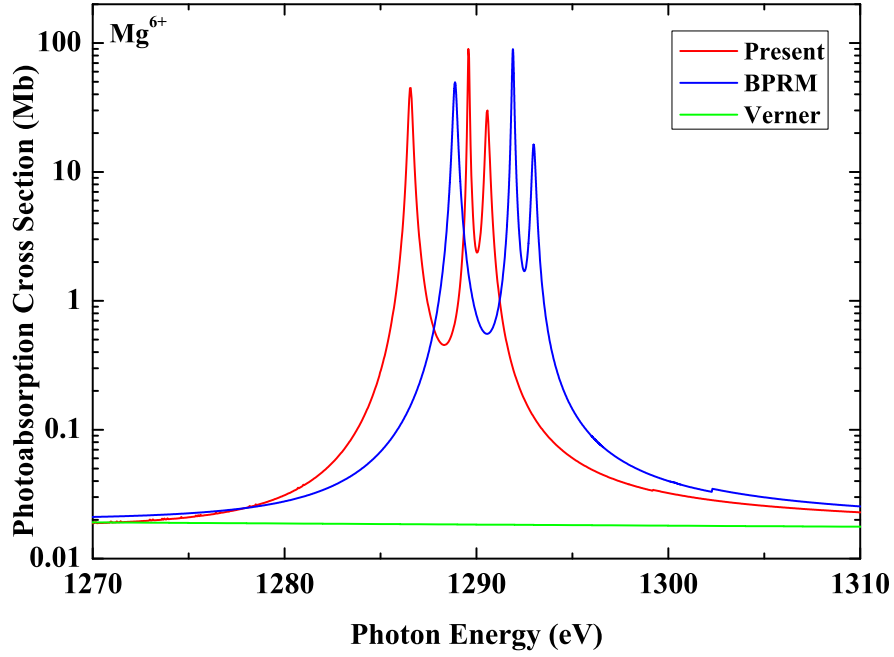
Figure 5.2   Same as Fig. 5.1, but for the photon energy range $1270 - 1310$ eV.

able data of Palmeri *et al.* [215] show good agreement.

In Fig. 5.1, the results for the K-shell photoabsorption cross section for Mg^{6+} versus the incident photon energy are presented. Also, my results are compared to the results obtained by Witthoeft *et al.* [140] using the Breit Pauli R-matrix (BPRM) method. Overall, good agreement is obtained and they align very well with the background of the photoionization results of Verner *et al.* [214].

Fig. 5.2 shows the photon energy range from 1270 to 1310 eV where the lowest $1s \rightarrow np$ photoexcitation is obtained from the $1s^2 2s^2 2p^2 [^3P]$ ground state of Mg^{6+} which can form the $1s 2s^2 2p^2 np [^3D, \, ^3S, \, ^3P]$ photoexcited states for $n = 2$. The energy positions for ^3D, ^3S, and ^3P are located at 1286.57, 1289.66, and 1290.63 eV, respectively, while the corresponding energy positions of Witthoeft *et al.* [140] obtained by using the BPRM are

Table 5.3 Comparison of Auger widths (in eV) for the 17 Mg^{7+} autoionizing target states above the K-shell threshold.

	State	Auger width (eV)		
		Present[a]	AUTO[b]	OTHER[c]
1	$1s2s^22p^2\,(^4P)$	0.11884	0.12341	0.106303
2	$1s2s^22p^2\,(^2D)$	0.17731	0.17741	0.167321
3	$1s2s^22p^2\,(^2P)$	0.07672	0.07139	0.062575
4	$1s2s^22p^2\,(^2S)$	0.15615	0.15202	0.136252
5	$1s2s(^3S)2p^3\,(^4D)$	0.11374	0.11462	0.118480
6	$1s2s(^1S)2p^3\,(^4S)$	0.02820	0.01962	0.009413
7	$1s2s(^3S)2p^3\,(^4P)$	0.08735	0.08698	0.090177
8	$1s2s(^1S)2p^3\,(^2D)$	0.15325	0.15515	0.144809
9	$1s2s(^3S)2p^3\,(^4S)$	0.10399	0.11340	0.094784
10	$1s2s(^1S)2p^3\,(^2P)$	0.12862	0.12420	0.114970
11	$1s2s(^3S)2p^3\,(^2D)$	0.18078	0.19156	0.177194
12	$1s2s(^3S)2p^3\,(^2P)$	0.15542	0.16217	0.146126
13	$1s2s(^3S)2p^3\,(^2S)$	0.03905	0.03308	0.050420
14	$1s2p^4\,(^4P)$	0.11414	0.12058	0.088202
15	$1s2p^4\,(^2D)$	0.18133	0.19077	0.137964
16	$1s2p^4\,(^2P)$	0.11356	0.11861	0.087983
17	$1s2p^4\,(^2S)$	0.12504	0.12932	0.091493

[a] Present R-matrix results.

[b] MCBP AUTOSTRUCTURE results [32, 186].

[c] Palmeri *et al*. [215].

1288.88, 1291.88, and 1292.94 eV, with a difference of up to 2.31 eV. Our binding energy for Mg^{6+} is higher than the one obtained form NIST by 0.26 eV. The calculated K-shelll photoabsorption in length and velocity gauges differs by less than 5%, so only the length results will be shown.

5.3.2 K-Shell Photoabsorption for Mg^{3+}

For Mg^{3+}, the K-shell photoexcitation of the ground state can be obtained as follows.

$$h\nu + 1s^2 2s^2 2p^5 [^2P] \rightarrow 1s 2s^2 2p^5 np [^2S, \, ^2P, \, ^2D]. \tag{5.6}$$

The participator and spectator Auger transitions are obtained as follows:

$$1s 2s^2 2p^5 np$$

participator Auger $\swarrow$ $\qquad\qquad\qquad$ $\searrow$ spectator Auger

$1s^2 2s^2 2p^4 + e^- \leftarrow$ $\qquad\qquad\qquad$ $\rightarrow 1s^2 2s^2 2p^3 np + e^-$

$1s^2 2s 2p^5 + e^- \leftarrow$ $\qquad\qquad\qquad$ $\rightarrow 1s^2 2s 2p^4 np + e^-$

$1s^2 2p^6 + e^- \leftarrow$ $\qquad\qquad\qquad$ $\rightarrow 1s^2 2p^5 np + e^-.$

Table 5.4 summarizes the procedure for generating the optimized radial orbitals for

Mg^{4+}, using the HF [159] and MCHF [160] program packages.

Table 5.4 Methodology of determining the physical $1s$, $2s$, and $2p$ orbitals and correlation (or pseudo) $\overline{3s}$, $\overline{3p}$, and $\overline{3d}$ orbitals for Mg^{4+}.

$1s$, $2s$, and $2p$	From a HF (single-configuration) calculation for the $1s^2 2s^2 2p^4 [^3P]$ term.
$\overline{3s}$, $\overline{3p}$, and $\overline{3d}$	From a MCHF (multiconfiguration) calculation for the lowest K-shell vacancy $1s 2s^2 2p^5 [^3P]$ term including single and double $n = 1 \rightarrow n = 3$ promotions.

The calculated term energies for Mg^{3+} and Mg^{4+}, relative to the $1s^2 2s^2 2p^4 [^3P]$ ground

state of Mg^{4+}, are compared to the data taken from NIST in Table 5.5. Good agreement is

obtained.

Table 5.5 Comparison of term energies (in Rydbergs) for Mg^{3+} and Mg^{4+} for the states included in my calculations relative to the $1s^2 2s^2 2p^4\,(^3P)$ ground state of Mg^{4+}.

		Term Energy (Ryd)	
	State	Present [a]	OTHER [b]
1	$1s^2 2s^2 2p^5\,(^2P)$	-8.082626	-8.036954
2	$1s^2 2s^2 2p^4\,(^3P)$	0.000000	0.00797
3	$1s^2 2s^2 2p^4\,(^1D)$	0.338589	0.32738
4	$1s^2 2s^2 2p^4\,(^1S)$	0.745541	0.70422
5	$1s^2 2s 2p^5\,(^3P)$	2.624466	2.58826
6	$1s^2 2s 2p^5\,(^1P)$	3.698571	3.62212
7	$1s^2 2p^6\,(^1S)$	6.176948	6.04143
8	$1s 2s^2 2p^5\,(^3P)$	92.810045	
9	$1s 2s^2 2p^5\,(^1P)$	93.280049	
10	$1s 2s 2p^6\,(^3S)$	95.458438	
11	$1s 2s 2p^6\,(^1S)$	96.142518	

[a] Present R-matrix results.

[b] NIST data.
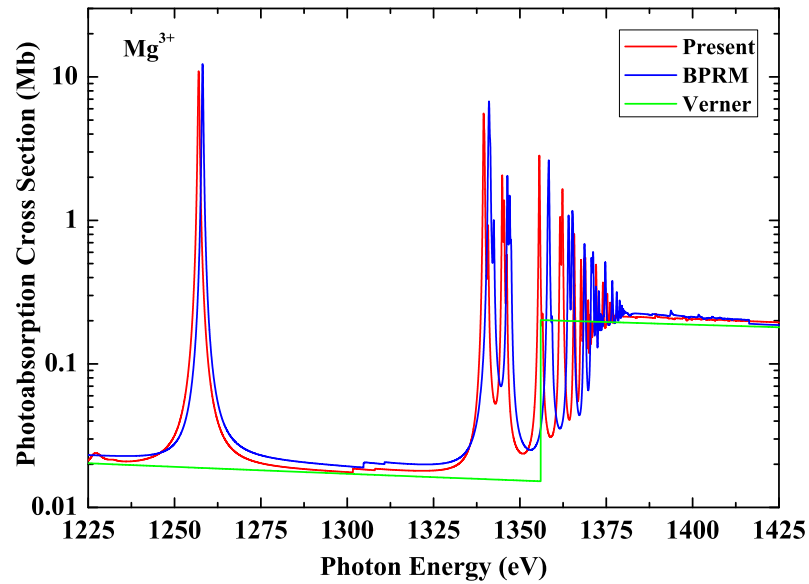
Figure 5.3 Same as Fig. 5.1 but for Mg^{3+}.

The results for the $1s \rightarrow np$ photoabsorption for Mg^{3+} are presented in Fig. 5.3. Analyzing the allowed partial waves (see Eq. (5.6)), we find that the lowest resonance is obtained by the $1s \rightarrow 2p$ photoexcitation, which gives the ^2S state and is located at 1257 eV with a cross section of 10.97 Mb. The corresponding BPRM [140] results are 1258.13 eV with a cross section of 12.32 Mb. There is an energy difference in the position of the peaks for this partial wave of 1.13 eV and a difference in the cross section of 12%. The rest of the K-shell photoabsorption is for $1s \rightarrow np$ $(n \geq 3)$ above 1325 eV.

5.3.3   K-Shell Photoabsorption for Mg^{2+}

In neon-like magnesium, which we expect to be much simpler because of the absence of the fine structure splitting, the K-shell photoabsorption can be represented as

$$h\nu + 1s^2 2s^2 2p^6 [^1S] \rightarrow 1s 2s^2 2p^6 np [^1P^o]. \tag{5.7}$$

The participator and spectator Auger transitions are obtained via

$$1s 2s^2 2p^6 np$$

participator Auger $\nearrow$ $\qquad\qquad\qquad$ $\searrow$ spectator Auger

$1s^2 2s^2 2p^5 + e^- \leftarrow$ $\qquad\qquad\qquad$ $\rightarrow 1s^2 2s^2 2p^4 np + e^-$

$1s^2 2s 2p^6 + e^- \leftarrow$ $\qquad\qquad\qquad$ $\rightarrow 1s^2 2s 2p^5 np + e^-$

$\qquad\qquad\qquad\qquad\qquad\qquad$ $\rightarrow 1s^2 2p^6 np + e^-.$
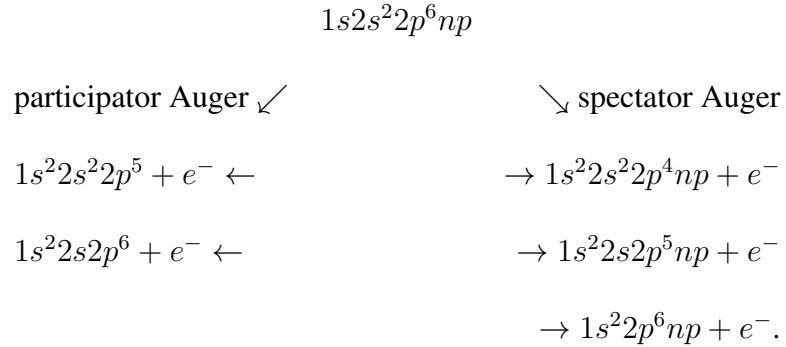
The Hartree-Fock [159] and multiconfiguration Hartree-Fock [160] atomic structure program packages are used to generate the radial orbitals for our target Mg^{3+}. The optimization procedure is summarized in Table 5.6.

Table 5.6   Methodology of determining the physical $1s$, $2s$, and $2p$ orbitals and correlation (or pseudo) $\overline{3s}$, $\overline{3p}$, and $\overline{3d}$ orbitals for Mg^{3+}.

$1s$, $2s$, and $2p$	From a HF (single-configuration) calculation for the $1s^2 2s^2 2p^5 [^2P]$ term.
$\overline{3s}$, $\overline{3p}$, and $\overline{3d}$	From a MCHF (multiconfiguration) calculation for the lowest K-shell vacancy $1s 2s^2 2p^6 [^2S]$ term including single and double $n = 1 \rightarrow n = 3$ promotions.

Fig. 5.4 presents the K-shell photoabsorption results for Mg^{2+} using the length and velocity forms of the dipole operator, where good agreement is obtained (difference of up to 4.5%).
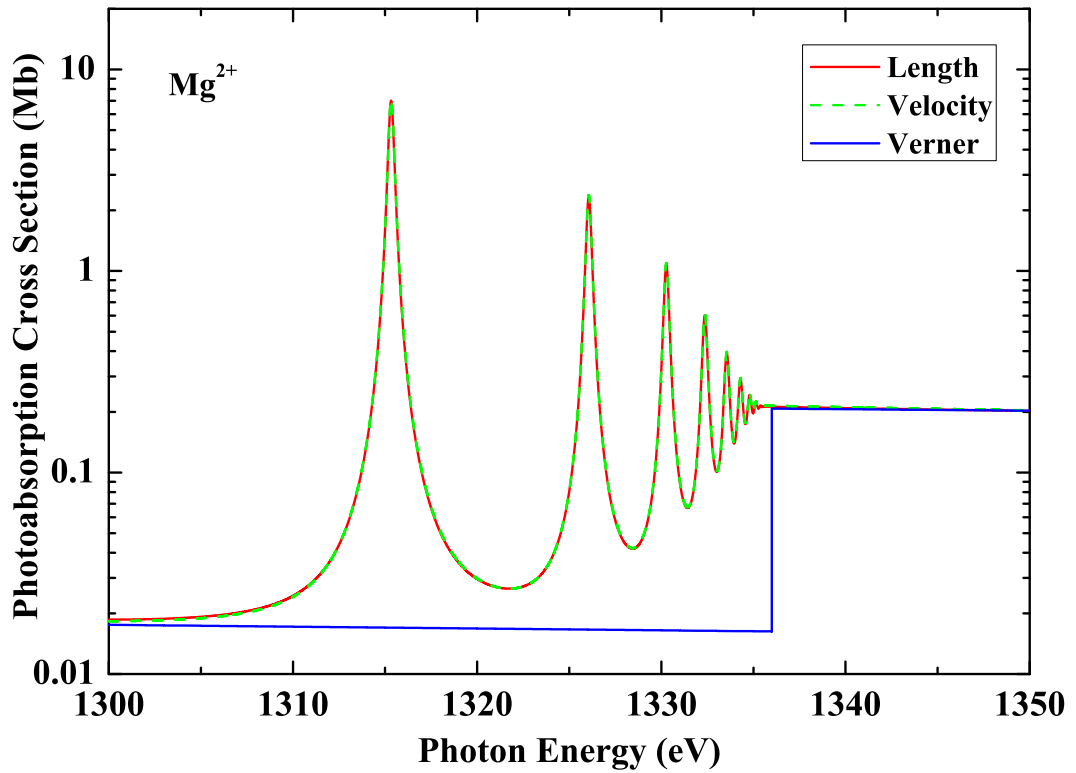
Figure 5.4   Comparisons of my results for the K-shell photoabsorption cross section in the length and velocity forms for the dipole operator for Mg^{2+}. Also, The K-shell photoionization results of Verner *et al.* [214].

Spectator Auger decay was found to be very important especially for $n \to \infty$, where the participator Auger decay scales as $1/n^3$ and goes to zero [133]. Fig. 5.5 shows my K-shell photoabsorption results with and without including the spectator Auger decays in the length form of the dipole operator for Mg^{2+}. As seen, the spectator Auger decay not only affects the photoabsorption cross sections for higher $1s2s^22p^6np$ resonances but also does for $n = 3$.
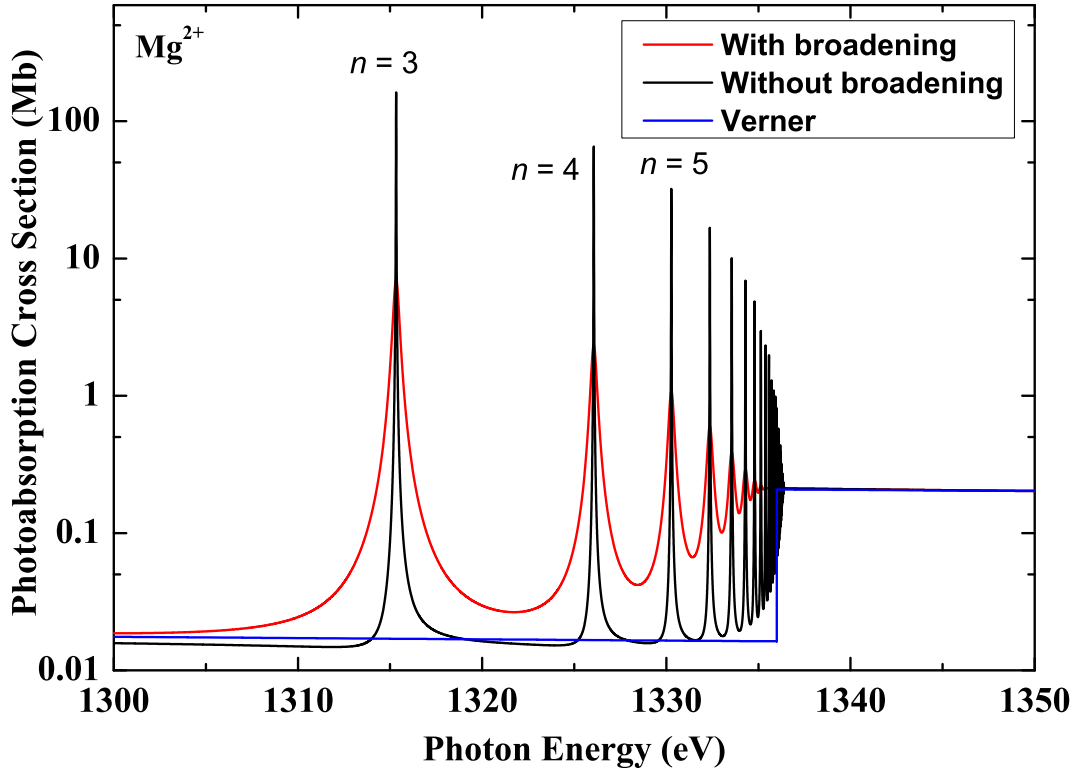
Figure 5.5   K-shell photoabsorption with and without including the spectator Auger decays (with broadening and without) in the length form of the dipole operator Mg^{2+}.

As can be seen from Eq. (5.7), K-shell photoabsorption of the $1s^22s^22p^6[^1S]$ ground state of Mg^{2+} gives rise to the $1s2s^22p^6np[^1P]$ states (see Sec. 2.5.1). Fig. 5.6 shows a

comparison between my results and those obtained using the BPRM by Witthoeft *et al.*
[140]. According to my calculations, the lowest resonance is obtained for $n = 3$ with its
peak located at 1315.33 eV and has a cross section of 7.01 Mb, while the corresponding one
from the BPRM is located at 1314.77 eV and a cross section of 8.495 Mb, with an energy
difference of 0.56 eV and 17% in the cross section. The higher resonances for $n = 4 - 6$
are located at 1326.06, 1330.27, and 1332.36 eV. As seen, our results align very well with
the photoionization results of Verner *et al.* [214].
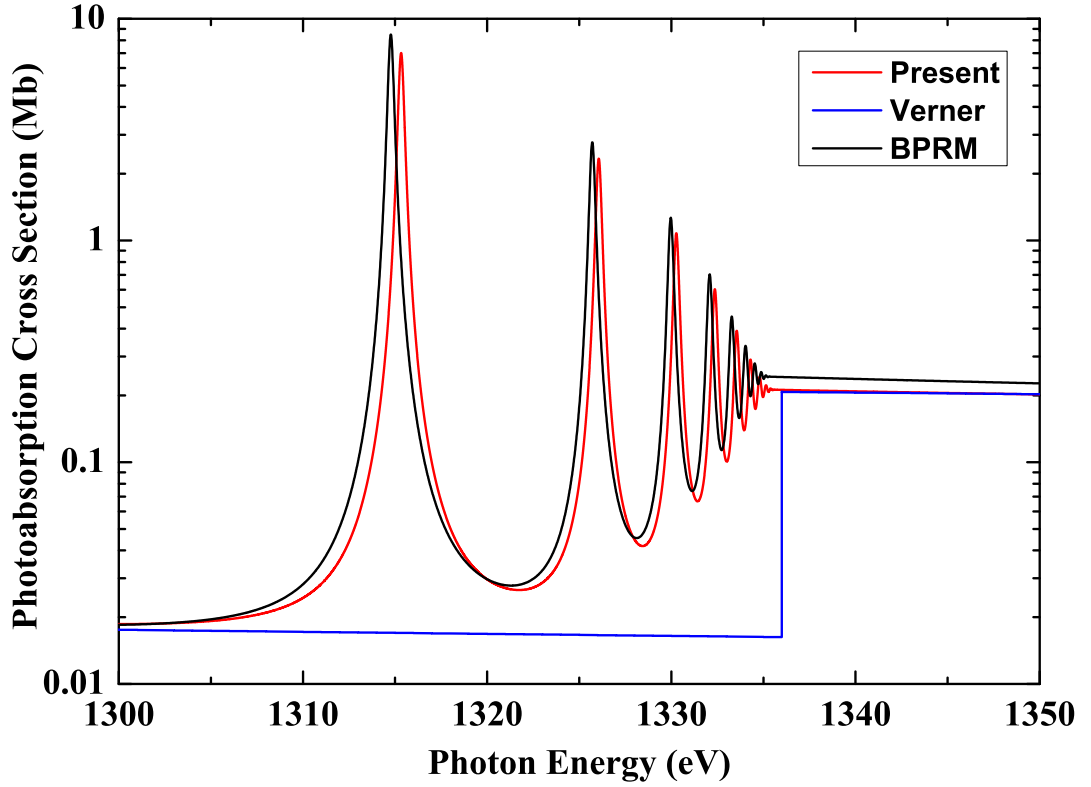
Figure 5.6   Comparisons of my calculated K-shell photoabsorption cross section for Mg^{2+},
the results of Witthoeft *et al.* [140] obtained by using the Breit Pauli R-matrix (BPRM), and the
photoionization results of Verner *et al.* [214].

5.3.4   K-Shell Photoabsorption for Neutral Mg

K-shell photoexcitation for the ground state of neutral magnesium is represented as

$$h\nu + 1s^2 2s^2 2p^6 3s^2 [^1S] \rightarrow 1s 2s^2 2p^6 3s^2 np [^1P]^o. \tag{5.8}$$

The participator and spectator Auger transitions are obtained as follows:

$$1s 2s^2 2p^6 3s^2 np$$

participator Auger $\swarrow$ $\qquad\qquad\qquad\qquad$ $\searrow$ spectator Auger

$$1s^2 2s^2 2p^6 3s + e^- \leftarrow \qquad\qquad \rightarrow 1s^2 2s^2 2p^6 np + e^-$$

$$1s^2 2s^2 2p^5 3s^2 + e^- \leftarrow \qquad\qquad \rightarrow 1s^2 2s^2 2p^5 3s np + e^-$$

$$1s^2 2s 2p^6 3s^2 + e^- \leftarrow \qquad\qquad \rightarrow 1s^2 2s 2p^6 3s np + e^-$$

$$\rightarrow 1s^2 2s^2 2p^4 3s^2 np + e^-$$

$$\rightarrow 1s^2 2s 2p^5 3s^2 np + e^-$$

$$\rightarrow 1s^2 2p^6 3s^2 np + e^-.$$

The physical $1s$, $2s$, $2p$, $3s$, $3p$, and $3d$ orbitals are first generated by performing a Hartree-Fock (HF) [159] calculation for the Mg$^+$ ($1s^2 2s^2 2p^6 3\ell [^2S]$) states. Then a multi-configuration Hartree-Fock (MCHF) [160] calculation is performed for the $1s 2s^2 2p^6 3s^2 [^2S]$ K-shell excited state including single and double promotions to $n = 4$ shell to obtain the $\overline{4s}$, $\overline{4p}$, and $\overline{4d}$ pseudo-orbitals, which accounts for orbital relaxation effects due to the $1s$-vacancy. A summary for the optimization procedure is presented in Table 5.7.

In my calculations, I included $1s^2 2s^2 2p^6 3s$, $1s^2 2s^2 2p^6 3p$, $1s^2 2s^2 2p^5 3s^2$, $1s^2 2s 2p^6 3s^2$, $1s 2s^2 2p^6 3s^2$, and $1s 2s^2 2p^6 3s 3p$ target states. Then the bound and pseudo-orbitals $\{1s, 2s,$

Table 5.7 Methodology of determining the physical $1s$, $2s$, $2p$, $3s$, $3p$, and $3d$ orbitals and correlation (or pseudo) $\overline{4s}$, $\overline{4p}$, and $\overline{4d}$ orbitals for Mg$^+$.

$1s$, $2s$, $2p$, $3s$, $3p$, and $3d$	From a HF (single-configuration) calculation for the $1s^2 2s^2 2p^6 3\ell[^2S]$ term.
$\overline{4s}$, $\overline{4p}$, and $\overline{4d}$	From a MCHF (multiconfiguration) calculation for the lowest K-shell vacancy $1s2s^2 2p^6 3s^2[^2S]$ term including single and double $n = 1 \rightarrow n = 4$ promotions.

$2p$, $3s$, $3p$, $3d$, $\overline{4s}$, $\overline{4p}$, $\overline{4d}$} are used to generate a CI basis considering single and double promotions out of the above six target configurations.
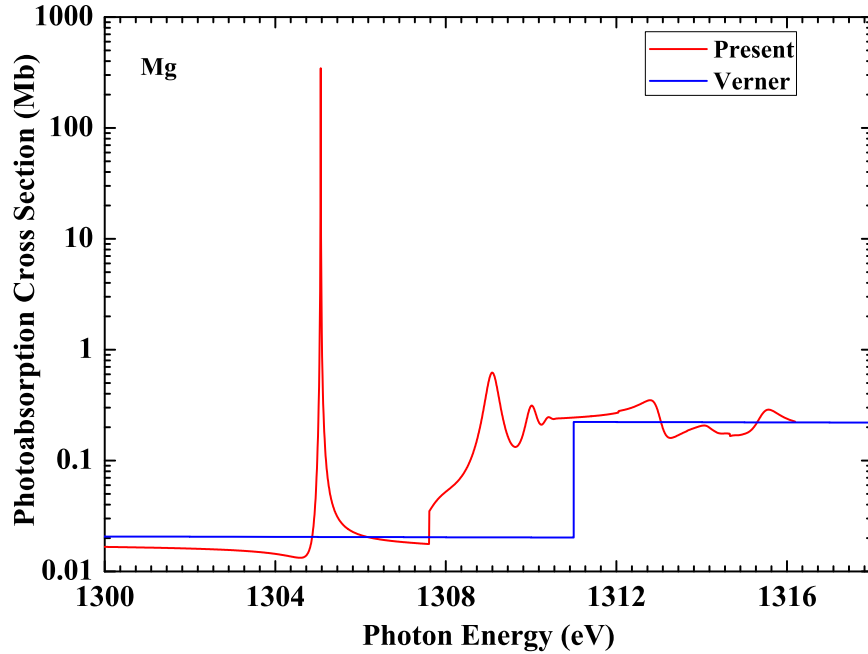
Figure 5.7 K-shell photoabsorption cross section for Mg and the photoionization results of Verner *et al.* [214].

Fig. 5.7 presents preliminary results for the K-shell photoabsorption of neutral magnesium. Above the threshold the $1s2s^2 2p^6 3s3p(ns, nd)$ resonances complicate the spectrum. The $1s2s^2 2p^6 3s^2 3p$ spectator Auger decay is not treated correctly (see Eq. 5.4) since the R-

126

matrix box contains this resonance. Therefore, these spectator channels need to be included in R-matrix explicitly and further work for neutral magnesium is required.

In summary, a series of K-shell photoabsorption calculations for Mg^{2+}, Mg^{3+}, Mg^{6+} were performed using the R-matrix method in *LS*-coupling. Good agreement with the recent results by Witthoeft *et al.* [140] of the Breit Pauli R-matrix was obtained. Preliminary work for neutral Mg was presented, which is complicated by the $n = 3$ physical orbitals.

CHAPTER VI

SUMMARY

The work in this dissertation has been focused on producing accurate and reliable DR and K-shell photoabsorption data. The DR rate coefficient data can be used for modeling ions that are found in astrophysical and fusion plasmas, and K-shell photoabsorption data can be used for modeling X-ray astrophysical spectra. Three projects have been studied throughout this work. The first one resulted in producing DR data for M-shell argon ions for fusion applications. The second one produced a comprehensive DR data set for the Al-like isoelectronic sequence for all the ions from Si^+ up to Zn^{17+}, and the third one produced K-shell photoabsorption results for Mg ions for astrophysical applications.

In the study of M-shell argon ions, DR rate coefficients for Ar^+- Ar^{7+} were produced using a configuration-average distorted-wave approximation (CADWA). Good agreement was obtained with the level-resolved distorted-wave rate coefficients for Ar^{6+} and Ar^{7+} for electron temperatures above 10.0 eV, where these ions are abundant in fusion sources. My M-shell DR rate coefficient data have been used in a study to determine the fractional abundances of argon, where significant differences from those obtained using the recommended data of Mazzotta *et al.* [123] were found and this ended in a publication by Loch *et al.* [185].

For the Al-like isoelectronic sequence, all previous DR data were either obtained by using empirical formulas or were performed in a non-relativistic *LS*-coupling framework. The commonly used database of Mazzotta *et al.* [123] was generated by fitting these pre-

vious data, but it was not clear from which sources they obtained their data [123]. I started the Al-like DR study by revisiting S^{3+}, where previous *LS*-coupling data were available for this ion by Badnell [128]. Good agreement was obtained with my results performed in *LS*-coupling and that pushed me to perform another calculation in IC-coupling. When I compared my *LS*- and IC-coupling DR rate coefficients, I found that fine structure effects led to the following. The DR rate coefficient performed in IC-coupling was higher at low-electron temperatures due to the fine structure series that can autoionize to the ground state of S^{3+}, which does not exist in a non-relativistic *LS* treatment. On the other hand, for higher-electron temperatures, the DR rate coefficient obtained in IC-coupling was lower due to the doubly excited states that can radiatively decay to autoionizing states for $n \geq 36$. Thus IC-coupling calculations are required for this isoelectronic sequence. The work on S^{3+} was published by Abdel-Naby *et al.* [207].

Calculations for the DR rate coefficient have been carried out for the entire Al-like isoelectronic sequence in both *LS*- and IC-coupling. Comparisons of my present DR rate coefficients in IC-coupling versus the existing *LS* results or the DR rate coefficients of Mazzotta *et al.* [123] were found to differ by orders of magnitudes at the low-electron temperatures since the latter did not include the fine structure splitting. This was confirmed by a comparison to the measurements from the Heidelberg heavy-ion Test Storage Ring (TSR) facility of Schmidt *et al.* [76], where my DR rate coefficient at low-electron temperatures is comparable to the experimental results. The DR and RR rate coefficients were then fitted to simple formulas for efficient dissemination of data and ease of use in plasma modeling codes. These results for the Al-like sequence are in preparation for publication [210].

The results for the K-shell photoabsorption of Mg^{2+}, Mg^{3+}, and Mg^{6+} agreed very well with the recent results of the Breit Pauli R-matrix of Witthoeft *et al.* [140]. Preliminary work for neutral Mg was presented, which was complicated by the $n = 3$ physical orbitals. The work on neutral Mg and Mg^{+} will be prepared for publication.

Appendix A

Atomic Units and Abbreviations

The Hamiltonian for our N-electron system is given by

$$\mathcal{H} = \sum_{i=1}^{N}\left(-\frac{\hbar^2}{2m_e}\nabla_i^2 - \frac{1}{4\pi\epsilon_0}\frac{Ze^2}{r_i}\right) + \sum_{i<j}^{N}\frac{1}{4\pi\epsilon_0}\frac{e^2}{r_{ij}}. \tag{A.1}$$

For simplicity in notation and for convenience in numerical work, we choose the atomic units (a.u.) such that $e = m_e = \hbar = a_0 = 4\pi\epsilon_0 = 1$. So the new form of the Hamiltonian is given by

$$\mathcal{H} = \sum_{i=1}^{N}\left(-\frac{1}{2}\nabla_i^2 - \frac{Z}{r_i}\right) + \sum_{i<j}^{N}\frac{1}{r_{ij}}. \tag{A.2}$$

In Table A.1, we present the conversion from the a.u. to the international system of units (SI) units. α is the fine-structure constant $\left(\alpha = \frac{1}{4\pi\epsilon_0}\frac{e^2}{\hbar c} = \frac{1}{137.03599911}\right)$.

Table A.1 Atomic units used through out this work.

Quantitiy	Symbol	SI Value[a,b]
Electric Charge	e	$1.60217648 \times 10^{-19}$ C
Electron Mass	m_e	$9.10938215 \times 10^{-31}$ kg
Action	$\hbar = \frac{h}{2\pi}$	$1.05457162 \times 10^{-34}$ J.s
Electrostatic force constant	$k = \frac{1}{4\pi\epsilon_0}$	8.9875518×10^{9} N.m^2/C^2
Borh radius	$a_0 = \frac{\hbar}{mc\alpha}$	$0.52917720 \times 10^{-10}$ m
Velocity	$v = \alpha c$	2.18769125×10^{6} m/s
Time	$\tau_0 = \frac{a_o}{\alpha c}$	$2.41888432 \times 10^{-17}$ s
Hartree Energy	$E_h = m(c\alpha)^2$	2 Ryd = 27.211 eV= 4.359743×10^{-18} J

[a] Mohr *et al.* [216].

[b] Mohr *et al.* [217].

Table A.2 Abbreviations used in this dissertation

ACRONYM	Name
AGN	active galactic nuclei
a.u.	atomic units
AUTOSTRUCTURE	atomic structure code
BPRM	Breit Pauli R-matrix method
CADWA	configuration-average distorted-wave approximation
CI	configuration interaction
CSF	configuration state function
DR	dielectronic recombination
EBIS	electron-beam ion source
EBIT	electron-beam ion trap
EIDE	electron impact de-excitation
EIE	electron impact excitation
EII	electron impact ionization
ESR	experimental Storage Ring
FAC	flexible atomic code
FWHM	full width at half maximum
HF	Hartree-Fock
HFR	Hartree-Fock relativistic approximation
HFSCF	Hartree-Fock self consistent field
IC	intermediate coupling
IP	independent-particle model
IPIRDW	independent-processes, isolated-resonance, distorted-wave approximation
ISM	interstellar medium
ITER	international thermonuclear experimental reactor
IXO	International X-ray observatory
LS	Russell-Saunders coupling
MBRRC	measured merged-beams electron-ion recombination rate coefficient
MCBP	multiconfiguration Breit-Pauli
MCDF	multiconfiguration Dirac-Fock
MQDT	multichannel quantum defect theory
MCHF	multiconfiguration Hartree-Fock
NIST	National Institute of Standards and Technology
PA	photoabsorption
PI	photoionization
RMBPT	relativistic many-body perturbation theory
RR	radiative recombination
RTE	resonant transfer excitation
SC	single configuration
SI	international system of units
SOHO	Solar and Heliospheric Observatory
STO	Slater-type-orbitals
TBR	three-body recombination
TSR	Test Storage Ring

BIBLIOGRAPHY

1. M. J. Seaton and P. J. Storey, *"Dielectronic Recombination."*, in *Atomic Processes and Applications*, edited by P. G. Burke, pp. 133–197, North-Holland, Amsterdam, Netherlands, 1976.

2. H. S. W. Massey and D. R. Bates, *"The Properties of Neutral and Ionized Atomic Oxygen and Their Influence on the Upper Atmosphere"*, Reports on Progress in Physics **9**, 62 (1942).

3. A. Burgess, *"Dielectronic Recombination and the Temperature of Solar Corona"*, Astrophysical Journal **139**, 776 (1964).

4. A. Burgess, *"A General Formula for Estimation of Dielectronic Recombination Coefficients in Low-Density Plasmas"*, Astrophysical Journal **141**, 1588 (1965).

5. W. H. Tucker and R. J. Gould, *"Radiation from a Low-Density Plasma at $10^6 - 10^8$ K"*, Astrophysical Journal **144**, 244 (1966).

6. I. L. Beĭgman, L. A. Vaĭnshteĭn, and R. A. Syunyaev, *"Special Issue: Dielectronic Recombination"*, Soviet Physics Uspekhi **11**, 411 (1968).

7. S. M. R. Ansari, G. Elwert, and P. Mücklich, *"On Dielectric Recombination"*, Zeitschrift Naturforschung Teil A **25**, 1781 (1970).

8. B. W. Shore, *"Dielectronic Recombination"*, Astrophysical Journal **158**, 1205 (1969).

9. A. Burgess and A. S. Tworkowski, *"Dielectronic Recombination to Form Helium-Like Ions"*, Astrophysical Journal **205**, L105 (1976).

10. J. N. Gau and Y. Hahn, *"Auger and Radiative Transition Probabilities of High Rydberg States"*, Physics Letters A **68**, 197 (1978).

11. J. A. Retter, J. N. Gau, and Y. Hahn, *"Scaling Properties of Dielectronic Recombination Amplitudes"*, Physical Review A **17**, 998 (1978).

12. Y. Hahn, *"Scaling Properties of the Dielectronic Recombination Rate"*, Physical Review A **22**, 2896 (1980).

13. K. J. LaGattuta and Y. Hahn, *"Dielectronic Recombination Involving High Rydberg States"*, Physics Letters A **84**, 468 (1981).

14. K. J. LaGattuta and Y. Hahn, *"Dielectronic Recombination Rate for Mo^{31+}"*, Physical Review A **24**, 785 (1981).

134

15. D. J. McLaughlin and Y. Hahn, *"Dielectronic Recombination Cross Section for the Li Sequence at Low Energies"*, Journal of Physics B: Atomic Molecular and Optical Physics **16**, L739 (1983).

16. K. LaGattuta, I. Nasser, and Y. Hahn, *"Electric Field Induced Mixing of High Rydberg-State Levels in Dielectronic Recombination: Mg^+ and Ca^+ Target Ions"*, Physical Review A **33**, 2782 (1986).

17. G. Omar and Y. Hahn, *"Dielectronic Recombination for Ca(XIII, XII, XI) with K-Shell Excitation"*, Physical Review A **35**, 918 (1987).

18. Y. Hahn, J. N. Gau, G. Omar, and M. P. Dube, *"Dielectronic Recombination for $Mo^{32+,31+,30+}$ with L-Shell Excitation"*, Physical Review A **36**, 576 (1987).

19. A. H. Moussa, H. H. Ramadan, and Y. Hahn, *"Dielectronic Recombination of Mg^{2+}, P^{5+}, and Cl^{7+}"*, Physical Review A **38**, 5076 (1988).

20. H. H. Ramadan and Y. Hahn, *"Resonant Electron Capture by B-Like Ions at Low Energies"*, Physical Review A **39**, 3350 (1989).

21. Y. Hahn and R. Bellantone, *"Dielectronic Recombination for Metastable O VII and C V Ions"*, Physical Review A **40**, 6117 (1989).

22. L. J. Roszman, *"Influence of Metastable States and Thermal Equilibration Upon Dielectronic Recombination in Low-Density to Moderate-Density Plasmas"*, Physical Review A **39**, 2073 (1989).

23. Y. Hahn, *"Improved Rate Formulas for Dielectronic Recombination"*, Journal of Quantitative Spectroscopy and Radiative Transfer **49**, 81 (1993).

24. J. Dubau and S. Volonte, *"Dielectronic Recombination and Its Applications in Astronomy"*, Reports on Progress in Physics **43**, 199 (1980).

25. Y. Hahn, *"Electron-Ion Recombination Processes- an Overview"*, Reports on Progress in Physics **60**, 691 (1997).

26. A. Dasgupta, *"Fine-Structure Resolved Dielectronic Recombination Rates for the $n = 3$ Excited Configurations of Fe XVI-Fe XIX"*, Astrophysical Journal Supplement Series **101**, 401 (1995).

27. M. H. Chen, *"Multiconfiguration Dirac-Fock Calculations of Dielectronic Recombination Coefficients for the He Isoelectronic Sequence"*, Physical Review A **33**, 994 (1986).

28. M. H. Chen, *"Relativistic Calculations of Dielectronic Recombination Coefficients for the Ne Isoelectronic Sequence"*, Physical Review A **34**, 1073 (1986).

29. M. H. Chen, *"Dielectronic Recombination Coefficient for F-Like Selenium"*, Physical Review A **34**, 1079 (1986).

30. M. H. Chen, *"Effects of Relativity and Configuration-Interaction on Dielectronic Recombination of Hydrogen-Like Ions"*, Physical Review A **38**, 3280 (1988).

31. M. H. Chen, K. J. Reed, D. S. Guo, and D. W. Savin, *"Dielectronic Recombination for Boron-Like Ions"*, Physical Review A **58**, 4539 (1998).

32. N. R. Badnell, *"Dielectronic Recombination of Fe^{22+} and Fe^{21+}"*, Journal of Physics B: Atomic and Molecular Physics **19**, 3827 (1986).

33. N. R. Badnell, *"Dielectronic Recombination Rate Coefficients for Be-Like Ions: $Z = 6 - 42$"*, Journal of Physics B: Atomic Molecular and Optical Physics **20**, 2081 (1987).

34. N. R. Badnell, *"The Influence of Core Fine Structure Interactions on Dielectronic Recombination at Low-Temperatures: B-Like C, N and O Recombined Ions"*, Journal of Physics B: Atomic Molecular and Optical Physics **21**, 749 (1988).

35. N. R. Badnell, *"Intermediate Coupling Dielectronic Recombination Rate Coefficients for the Ground and Metastable Levels of C and O Ions"*, Physica Scripta **T28**, 33 (1989).

36. N. R. Badnell and M. S. Pindzola, *"Intermediate Coupling Calculations for the Dielectronic Recombination of B-Like Ions"*, Physical Review A **39**, 1685 (1989).

37. N. R. Badnell and M. S. Pindzola, *"Intermediate Coupling Effects in the Dielectronic Recombination of Oxygen Ions"*, Physical Review A **39**, 1690 (1989).

38. N. R. Badnell and M. S. Pindzola, *"Dielectronic Recombination of P^{5+} and Cl^{7+} in Configuration-Average, LS-Coupling, and Intermediate-Coupling Approximations"*, Physical Review A **39**, 6165 (1989).

39. M. S. Pindzola, N. R. Badnell, and D. C. Griffin, *"Dielectronic Recombination Cross Sections for H-Like Ions"*, Physical Review A **42**, 282 (1990).

40. G. Kilgus, J. Berger, P. Blatt, M. Grieser, D. Habs, B. Hochadel, E. Jaeschke, D. Kramer, R. Neumann, G. Neureither, W. Ott, D. Schwalm, M. Steck, R. Stokstad, E. Szmola, A. Wolf, R. Schuch, A. Muller, and M. Wagner, *"Dielectronic Recombination of Hydrogen-Like Oxygen in a Heavy-Ion Storage Ring"*, Physical Review Letters **64**, 737 (1990).

41. T. W. Gorczyca and N. R. Badnell, *"Effect of the Configuration Interaction Between Resonances for Dielectronic Recombination and Resonant Transfer Excitation of Na-Like Ions"*, Physical Review A **54**, 4113 (1996).

42. J. Linkemann, J. Kenntner, A. Muller, A. Wolf, D. Habs, D. Schwalm, W. Spies, O. Uwira, A. Frank, A. Liedtke, G. Hofmann, E. Salzborn, N. R. Badnell, and M. S. Pindzola, *"Electron-Impact Ionization and Dielectronic Recombination of Sodium-Like Iron Ions"*, Nuclear Instruments and Methods in Physics Research Section B: Beam Interactions with Materials and Atoms **98**, 154 (1995).

43. S. N. Nahar and A. K. Pradhan, *"Unified Treatment of Electron-Ion Recombination in the Close-Coupling Approximation"*, Physical Review A **49**, 1816 (1994).

44. S. N. Nahar and A. K. Pradhan, *"Unified Electron-Ion Recombination Rate Coefficients of Silicon and Sulfur Ions"*, Astrophysical Journal **447**, 966 (1995).

45. F. Robicheaux, T. W. Gorczyca, M. S. Pindzola, and N. R. Badnell, *"Inclusion of Radiation Damping in the Close-Coupling Equations for Electron-Atom Scattering"*, Physical Review A **52**, 1319 (1995).

46. T. W. Gorczyca, F. Robicheaux, M. S. Pindzola, and N. R. Badnell, *"Comparisons Between Perturbative and Radiation-Damped R-Matrix Approaches to Dielectronic Recombination: Application to Ar^{15+}"*, Physical Review A **54**, 2107 (1996).

47. T. W. Gorczyca, N. R. Badnell, and D. W. Savin, *"Shortcomings of the R-matrix method for treating dielectronic recombination"*, Physical Review A **65**, 062707 (2002).

48. C. Breton, C. Demichelis, M. Finkenthal, and M. Mattioli, *"Ionization and Recombination Rate Coefficients of Highly Ionized Molybdenum Ions from Spectroscopy of Tokamak Plasmas"*, Physical Review Letters **41**, 110 (1978).

49. R. C. Isler, E. C. Crume, and D. E. Arnurius, *"Ionization and Recombination Coefficients for Fe XV Fe XIX"*, Physical Review A **26**, 2105 (1982).

50. J. P. Briand, P. Charles, J. Arianer, H. Laurent, C. Goldstein, J. Dubau, M. Loulergue, and F. Belydubau, *"Observation of the KLL Dielectronic Recombination Process in Highly Stripped Argon Ions"*, Physical Review Letters **52**, 617 (1984).

51. R. Ali, C. P. Bhalla, C. L. Cocke, and M. Stockli, *"Dielectronic Recombination on Heliumlike Argon"*, Physical Review Letters **64**, 633 (1990).

52. D. A. Knapp, R. E. Marrs, M. A. Levine, C. L. Bennett, M. H. Chen, J. R. Henderson, M. B. Schneider, and J. H. Scofield, *"Dielectronic Recombination of Helium-Like Nickel"*, Physical Review Letters **62**, 2104 (1989).

53. P. Beiersdorfer, T. W. Phillips, K. L. Wong, R. E. Marrs, and D. A. Vogel, *"Measurement of Level-Specific Dielectronic-Recombination Cross-Sections of Helium-Like Fe XXV"*, Physical Review A **46**, 3812 (1992).

54. J. A. Tanis, S. M. Shafroth, J. E. Willis, M. Clark, J. Swenson, E. N. Strait, and J. R. Mowat, *"Simultaneous Electron-Capture and Excitation in S + Ar Collisions"*, Physical Review Letters **47**, 828 (1981).

55. J. B. A. Mitchell, C. T. Ng, J. L. Forand, D. P. Levac, R. E. Mitchell, A. Sen, D. B. Miko, and J. W. Mcgowan, *"Dielectronic Recombination Cross-Section Measurements for C^+ Ions"*, Physical Review Letters **50**, 335 (1983).

56. P. F. Dittner, S. Datz, R. Hippler, H. F. Krause, P. D. Miller, P. L. Pepmiller, C. M. Fou, Y. Hahn, and I. Nasser, *"Dielectronic Recombination of the B-Like Ions - N^{2+}, O^{3+}, and F^{4+}"*, Physical Review A **38**, 2762 (1988).

57. D. R. Dewitt, E. Lindroth, R. Schuch, H. Gao, T. Quinteros, and W. Zong, *"Spectroscopy of Highly Doubly-Excited States of Helium through Dielectronic Recombination"*, Journal of Physics B: Atomic Molecular and Optical Physics **28**, L147 (1995).

58. D. W. Savin, T. Bartsch, M. H. Chen, S. M. Kahn, D. A. Liedahl, J. Linkemann, A. Muller, S. Schippers, M. Schmitt, D. Schwalm, and A. Wolf, *"Dielectronic Recombination in Photoionized Gas: the Importance of Fine-Structure Core Excitations"*, Astrophysical Journal **489**, L115 (1997).

59. O. Uwira, A. Muller, J. Linkemann, T. Bartsch, C. Brandau, M. Schmitt, A. Wolf, D. Schwalm, R. Schuch, W. Zong, H. Lebius, W. G. Graham, J. Doerfert, and D. W. Savin, *"Recombination Measurements at Low Energies With Au^{49+}, Au^{50+}, Au^{51+} at the TSR"*, Hyperfine Interactions **108**, 149 (1997).

60. W. Zong, R. Schuch, E. Lindroth, H. Gao, D. R. DeWitt, S. Asp, and H. Danared, *"Accurate Determination of Dielectronic Recombination Resonances with Lithium-Like Argon"*, Physical Review A **56**, 386 (1997).

61. S. Mannervik, D. DeWitt, L. Engstrom, J. Lidberg, E. Lindroth, R. Schuch, and W. Zong, *"Strong Relativistic Effects and Natural Linewidths Observed in Dielectronic Recombination of Lithium-Like Carbon"*, Physical Review Letters **81**, 313 (1998).

62. D. W. Savin, S. M. Kahn, J. Linkemann, A. A. Saghiri, M. Schmitt, M. Grieser, R. Repnow, D. Schwalm, A. Wolf, T. Bartsch, C. Brandau, A. Hoffknecht, A. Muller, S. Schippers, M. H. Chen, and N. R. Badnell, *"Dielectronic Recombination in Photoionized Gas. II. Laboratory Measurements for Fe XVIII and Fe XIX"*, Astrophysical Journal Supplement Series **123**, 687 (1999).

63. P. Glans, E. Lindroth, N. Eklow, W. Zong, G. Gwinner, A. A. Saghiri, M. Pajek, H. Danared, and R. Schuch, *"Dielectronic Recombination of Li-Like Fluorine Ions"*, Nuclear Instruments and Methods in Physics Research Section B: Beam Interactions with Materials and Atoms **154**, 97 (1999).

64. P. Glans, E. Lindroth, N. R. Badnell, N. Eklow, W. Zong, E. Justiniano, and R. Schuch, *"Dielectronic recombination of N^{4+}"*, Physical Review A **64**, 043609 (2001).

65. S. Bohm, S. Schippers, W. Shi, A. Muller, N. Djuric, G. H. Dunn, W. Zong, B. Jelenkovic, H. Danared, N. Eklow, P. Glans, and R. Schuch, *"Influence of Electromagnetic Fields on the Dielectronic Recombination of Ne^{7+} Ions"*, Physical Review A **64**, 032707 (2001).

66. S. Bohm, S. Schippers, W. Shi, A. Muller, N. Eklow, R. Schuch, H. Danared, N. R. Badnell, D. M. Mitnik, and D. C. Griffin, *"Measurement of the Field-Induced Dielectronic Recombination Rate Enhancement of O^{5+} Ions Differential in the Rydberg Quantum Number n"*, Physical Review A **65**, 52728 (2002).

67. D. W. Savin, S. M. Kahn, J. Linkemann, A. A. Saghiri, M. Schmitt, M. Grieser, R. Repnow, D. Schwalm, A. Wolf, T. Bartsch, A. Müller, S. Schippers, M. H. Chen, N. R. Badnell, T. W. Gorczyca, and O. Zatsarinny, *"Dielectronic Recombination of Fe XIX forming Fe XVIII: Laboratory Measurements and Theoretical Calculations"*, Astrophysical Journal **576**, 1098 (2002).

68. D. W. Savin, E. Behar, S. M. Kahn, G. Gwinner, A. A. Saghiri, M. Schmitt, M. Grieser, R. Repnow, D. Schwalm, A. Wolf, T. Bartsch, A. Müller, S. Schippers, N. R. Badnell, M. H. Chen, and T. W. Gorczyca, *"Dielectronic Recombination (via $N = 2 \rightarrow N' = 2$ Core Excitations) and Radiative Recombination of Fe XX: Laboratory Measurements and Theoretical Calculations"*, Astrophysical Journal Supplement Series **138**, 337 (2002).

69. S. Bohm, A. Muller, S. Schippers, W. Shi, N. Eklow, R. Schuch, H. Danared, and N. R. Badnell, *"Experimental O VI Dielectronic Recombination Rate Coefficient and Its Enhancement by External Electric Fields"*, Astronomy and Astrophysics **405**, 1157 (2003).

70. D. W. Savin, S. M. Kahn, G. Gwinner, M. Grieser, R. Repnow, G. Saathoff, D. Schwalm, A. Wolf, A. Müller, D. Schippers, P. A. Zavodszky, M. H. Chen, T. W. Gorczyca, O. Zatsarinny, and M. F. Gu, *"Dielectronic Recombination of Fe XXI and Fe XXII via $N = 2 \rightarrow N' = 2$ Core Excitations"*, Astrophysical Journal Supplement Series **147**, 421 (2003).

71. M. Fogle, N. R. Badnell, N. Eklow, T. Mohamed, and R. Schuch, *"Determination of the Ni XVIII Plasma Recombination Rate Coefficient"*, Astronomy and Astrophysics **409**, 781 (2003).

72. D. Nikolić, E. Lindroth, S. Kieslich, C. Brandau, S. Schippers, W. Shi, A. Muller, G. Gwinner, M. Schnell, and A. Wolf, *"Dielectronic Recombination Resonances in Na^{8+}"*, Physical Review A **70**, 062723 (2004).

73. P. Glans, M. Fogle, S. Madzunkov, M. Tokman, D. Nikolić, T. Mohamed, N. Eklow, N. R. Badnell, E. Lindroth, and R. Schuch, *"Dielectronic Recombination Used as a Tool for Spectroscopic Studies of Highly Charged Ions"*, Physica Scripta **T110**, 212 (2004).

74. M. Fogle, N. R. Badnell, P. Glans, S. D. Loch, S. Madzunkov, S. A. Abdel-Naby, M. S. Pindzola, and R. Schuch, *"Electron-Ion Recombination of Be-Like C, N, and O"*, Astronomy and Astrophysics **442**, 757 (2005).

75. M. Fogle, R. Schuch, N. R. Badnell, S. D. Loch, S. A. Abdel-Naby, M. S. Pindzola, and P. Glans, *"Recombination of Astrophysically Relevant Ions: Be-Like C, N, and O"*, in *Photonic, Electronic and Atomic Collisions*, edited by P. D. Fainstein, M. A. P. Lima, J. E. Miraglia, E. C. Montenegro, and R. D. Rivarola, p. 273, 2006.

76. E. W. Schmidt, S. Schippers, A. Müller, M. Lestinsky, F. Sprenger, M. Grieser, R. Repnow, A. Wolf, C. Brandau, D. Lukić, M. Schnell, and D. W. Savin, *"Electron-Ion Recombination Measurements Motivated by AGN X-Ray Absorption Features: Fe XIV Forming Fe XIII"*, Astrophysical Journal **641**, L157 (2006).

77. E. W. Schmidt, S. Schippers, C. Brandau, D. Bernhardt, A. Müller, M. Lestinsky, F. Sprenger, J. Homann, D. A. Orlov, M. Grieser, R. Repnow, A. Wolf, D. Lukic, M. Schnell, and D. W. Savin, *"Electron-Ion Recombination Measurements of Fe^{7+}, Fe^{8+}, Fe^{13+} Motivated by Active Galactic Nuclei X-Ray Absorption Features"*, Journal of Physics Conference Series **58**, 223 (2007).

78. E. W. Schmidt, S. Schippers, D. Bernhardt, A. Muller, J. Hoffmann, M. Lestinsky, D. A. Orlov, A. Wolf, D. V. Lukic, D. W. Savin, and N. R. Badnell, *"Electron-Ion Recombination for Fe VIII Forming Fe VII and Fe IX Forming Fe VIII: Measurements and Theory"*, Astronomy and Astrophysics **492**, 265 (2008).

79. E. W. Schmidt, D. Bernhardt, A. Muller, S. Schippers, S. Fritzsche, J. Hoffmann, A. S. Jaroshevich, C. Krantz, M. Lestinsky, D. A. Orlov, A. Wolf, D. Lukic, and D. W. Savin, *"Electron-Ion Recombination of Si IV Forming Si III: Storage-Ring Measurement and Multiconfiguration Dirac-Fock Calculations"*, Physical Review A **76**, 032717 (2007).

80. M. Lestinsky, N. R. Badnell, D. Bernhardt, M. Grieser, J. Hoffmann, D. Lukic, A. Muller, D. A. Orlov, R. Repnow, D. W. Savin, E. W. Schmidt, M. Schnell, S. Schippers, A. Wolf, and D. Yu, *"Electron-Ion Recombination of Fe X Forming Fe IX and of Fe XI Forming Fe X: Laboratory Measurements and Theoretical Calculations"*, Astrophysical Journal **698**, 648 (2009).

81. Y. Hahn, *"Theory of Dielectronic Recombination"*, Advances in Atomic and Molecular Physics **21**, 123 (1985).

82. M. S. Pindzola, D. C. Griffin, and N. R. Badnell, *"Dielectronic Recombination"*, in *Springer Handbook of Atomic, Molecular, and Optical Physics*, edited by Gordon W. F. Drake, pp. 829–834, New York, NY, 2006.

83. T. R. Kallman and P. Palmeri, *"Atomic Data for X-Ray Astrophysics"*, Reviews of Modern Physics **79**, 79 (2007).

84. S. M. V. Aldrovandi and D. Péquignot, *"Radiative and Dielectronic Recombination Coefficients for Complex Ions"*, Astronomy and Astrophysics **25**, 137 (1973).

85. R. Mewe, J. Schrijver, and J. Sylwester, *"Analysis of X-Ray Line Spectra From a Transient Plasma Under Solar Flare Conditions. II - Rate Coefficients. III - Diagnostics for Measuring Electron Temperature and Density"*, Astronomy and Astrophysics **40**, 323 (1980).

86. J. M. Shull and M. V. Steenberg, *"The Ionization Equilibrium of Astrophysically Abundant Elements"*, Astrophysical Journal Supplement Series **48**, 95 (1982).

87. M. Arnaud and J. Raymond, *"Iron Ionization and Recombination Rates and Ionization Equilibrium"*, Astrophysical Journal **398**, 394 (1992).

88. M. Landini and B. C. M. Fossi, *"The X-UV Spectrum of Thin Plasmas"*, Astronomy and Astrophysics Supplement Series **82**, 229 (1990).

89. M. Landini and B. C. M. Fossi, *"Ion Equilibrium for Minor Components in a Thin Plasma"*, Astronomy and Astrophysics Supplement Series **91**, 183 (1991).

90. N. R. Badnell, M. G. O'Mullane, H. P. Summers, Z. Altun, M. A. Bautista, J. Colgan, T. W. Gorczyca, D. M. Mitnik, M. S. Pindzola, and O. Zatsarinny, *"Dielectronic Recombination Data for Dynamic Finite-Density Plasmas. I. Goals and Methodology"*, Astronomy and Astrophysics **406**, 1151 (2003).

91. N. R. Badnell, *"Dielectronic Recombination Data for Dynamic Finite-Density Plasmas - X. The Hydrogen Isoelectronic Sequence"*, Astronomy and Astrophysics **447**, 389 (2006).

92. M. A. Bautista and N. R. Badnell, *"Dielectronic Recombination Data for Dynamic Finite-Density Plasmas - XII. The Helium Isoelectronic Sequence"*, Astronomy and Astrophysics **466**, 755 (2007).

93. J. Colgan, M. S. Pindzola, and N. R. Badnell, *"Dielectronic Recombination Data for Dynamic Finite-Density Plasmas - V: The Lithium Isoelectronic Sequence"*, Astronomy and Astrophysics **417**, 1183 (2004).

94. J. Colgan, M. S. Pindzola, A. D. Whiteford, and N. R. Badnell, *"Dielectronic Recombination Data for Dynamic Finite-Density Plasmas - III. The Beryllium Isoelectronic Sequence"*, Astronomy and Astrophysics **412**, 597 (2003).

95. Z. Altun, A. Yumak, N. R. Badnell, J. Colgan, and M. S. Pindzola, *"Dielectronic Recombination Data for Dynamic Finite-Density Plasmas - VI. The Boron Isoelectronic Sequence"*, Astronomy and Astrophysics **420**, 775 (2004).

96. O. Zatsarinny, T. W. Gorczyca, K. T. Korista, N. R. Badnell, and D. W. Savin, *"Dielectronic Recombination Data for Dynamic Finite-Density Plasmas - IV. The Carbon Isoelectronic Sequence"*, Astronomy and Astrophysics **417**, 1173 (2004).

97. D. M. Mitnik and N. R. Badnell, *"Dielectronic Recombination Data for Dynamic Finite-Density Plasmas - VIII. The Nitrogen Isoelectronic Sequence"*, Astronomy and Astrophysics **425**, 1153 (2004).

98. O. Zatsarinny, T. W. Gorczyca, K. T. Korista, N. R. Badnell, and D. W. Savin, *"Dielectronic Recombination Data for Dynamic Finite-Density Plasmas - II. The Oxygen Isoelectronic Sequence"*, Astronomy and Astrophysics **412**, 587 (2003).

99. O. Zatsarinny, T. W. Gorczyca, J. Fu, K. T. Korista, N. R. Badnell, and D. W. Savin, *"Dielectronic Recombination Data for Dynamic Finite-Density Plasmas IX. The Fluorine Isoelectronic Sequence"*, Astronomy and Astrophysics **447**, 379 (2006).

100. O. Zatsarinny, T. W. Gorczyca, K. Korista, N. R. Badnell, and D. W. Savin, *"Dielectronic Recombination Data for Dynamic Finite-Density Plasmas - VII. The Neon Isoelectronic Sequence"*, Astronomy and Astrophysics **426**, 699 (2004).

101. Z. Altun, A. Yumak, N. R. Badnell, S. D. Loch, and M. S. Pindzola, *"Dielectronic Recombination Data for Dynamic Finite-Density Plasmas - XI. The Sodium Isoelectronic Sequence"*, Astronomy and Astrophysics **447**, 1165 (2006).

102. Z. Altun, A. Yumak, I. Yavuz, N. R. Badnell, S. D. Loch, and M. S. Pindzola, *"Dielectronic Recombination Data for Dynamic Finite-Density Plasmas - XIII. The Magnesium Isoelectronic Sequence"*, Astronomy and Astrophysics **474**, 1051 (2007).

103. D. Nikolić, T. W. Gorczyca, K. T. Korista, and N. R. Badnell, *"Dielectronic Recombination of Argon-Like Ions"*, ArXiv: 1003.5161 (2010).

104. N. R. Badnell, *"Dielectronic Recombination of Fe^{13+}: Benchmarking the M-Shell"*, Journal of Physics B: Atomic Molecular and Optical Physics **39**, 4825 (2006).

105. N. R. Badnell, *"Radiative Recombination Data for Modeling Dynamic Finite-Density Plasmas"*, The Astrophysical Journal Supplement Series **167**, 334 (2006).

106. D. W. Savin and J. M. Laming, *"Uncertainties in Dielectronic Recombination Rate Coefficients: Effects on Solar and Stellar Upper Atmosphere Abundance Determinations"*, Astrophysical Journal **566**, 1166 (2002).

107. D. W. Savin, G. Gwinner, M. Grieser, R. Repnow, M. Schnell, D. Schwalm, A. Wolf, S. G. Zhou, S. Kieslich, A. Müller, S. Schippers, J. Colgan, S. D. Loch, N. R. Badnell, M. H. Chen, and M. F. Gu, *"Dielectronic Recombination of Fe XXIII forming Fe XXII: Laboratory Measurements and Theoretical Calculations"*, Astrophysical Journal **642**, 1275 (2006).

108. D. V. Lukic, M. Schnell, D. W. Savin, C. Brandau, E. W. Schmidt, S. Bohm, A. Müller, S. Schippers, M. Lestinsky, F. Sprenger, A. Wolf, Z. Altun, and N. R. Badnell, *"Dielectronic Recombination of Fe XV Forming Fe XIV: Laboratory Measurements and Theoretical Calculations"*, The Astrophysical Journal **664**, 1244 (2007).

109. S. Schippers, M. Lestinsky, A. Müller, D. W. Savin, E. W. Schmidt, and A. Wolf, *"Dielectronic Recombination Data for Astrophysical Applications: Plasma Rate-Coefficients for Fe^{q+} (q = 7 − 10, 13 − 22) and Ni^{25+} Ions From Storage-Ring Experiments"*, ArXiv: 1002.3678 (2010).

110. M. F. Gu, *"Dielectronic Recombination Rate Coefficients for H-Like Through Ne-Like Isosequences of Mg, Si, S, Ar, Ca, Fe, and Ni"*, Astrophysical Journal **590**, 1131 (2003).

111. I. Orban, E. Lindroth, P. Glans, and R. Schuch, *"Spectroscopic Study of Doubly Excited states in Mg-Like Si Using Dielectronic Recombination"*, Journal of Physics B: Atomic Molecular and Optical Physics **40**, 1063 (2007).

112. M. J. May, K. B. Fournier, D. Pacella, H. Kroegler, J. E. Rice, B. Gregory, M. Finkenthal, H. W. Moos, G. Mazzitelli, and W. H. Goldstein, *"Observations of the Ultraviolet and X-Ray Brightness Profiles and Cooling Rates of Kr and Ar in Magnetically Confined Fusion Plasmas"*, Physical Review E **61**, 3042 (2000).

113. M. Mattioli, K. B. Fournier, L. Carraro, I. Coffey, C. Giroud, K. Lawson, P. Monier-Garbet, M. O'Mullane, J. Ongena, M. E. Puiatti, F. Sattin, P. Scarin, and M. Valisa, *"Experimental and Simulated Argon Spectra in the 2.3-3.4 nm Region from Tokamak Plasmas"*, Journal of Physics B: Atomic Molecular and Optical Physics **34**, 127 (2001).

114. D. G. Whyte, T. C. Jernigan, D. A. Humphreys, A. W. Hyatt, C. J. Lasnier, P. B. Parks, T. E. Evans, M. N. Rosenbluth, P. L. Taylor, A. G. Kellman, D. S. Gray, E. M. Hollmann, and S. K. Combs, *"Mitigation of Tokamak Disruptions Using High-Pressure Gas Injection"*, Physical Review Letters **89**, 055001 (2002).

115. P. Bryans, N. R. Badnell, T. W. Gorczyca, J. M. Laming, W. Mitthumsiri, and D. W. Savin, *"Collisional Ionization Equilibrium for Optically Thin Plasmas. I. Updated Recombination Rate Coefficients for Bare through Sodium-like Ions"*, Astrophysical Journal Supplement Series **167**, 343 (2006).

116. G. J. Ferland, K. T. Korista, D. A. Verner, J. W. Ferguson, J. B. Kingdon, and E. M. Verner, *"CLOUDY 90: Numerical Simulation of Plasmas and Their Spectra"*, The Astronomical Society of the Pacific **110**, 761 (1998).

117. T. Kallman and M. Bautista, *"Photoionization and High-Density Gas"*, Astrophysical Journal Supplement Series **133**, 221 (2001).

118. M. Arnaud and R. Rothenflug, *"An Updated Evaluation of Recombination and Ionization Rates"*, Astronomy and Astrophysics Supplement Series **60**, 425 (1985).

119. T. R. Kallman and S. Kahn, *"Photoionization Equilibrium Modeling of Iron L Line Emission"*, Astrophysical Journal **465**, 994 (1996).

120. E. Landi, G. Del Zanna, P. R. Young, K. P. Dere, H. E. Mason, and M. Landini, *"CHIANTI - An Atomic Database for Emission Lines. VII. New Data for X-Rays and Other Improvements"*, Astrophysical Journal Supplement Series **162**, 261 (2006).

121. K. P. Dere, E. Landi, P. R. Young, G. Del Zanna, M. Landini, and H. E. Mason, *"CHIANTI - an Atomic Database for Emission Lines IX. Ionization Rates, Recombination Rates, Ionization Equilibria for the Elements Hydrogen Through Zinc and Updated Atomic Data"*, Astronomy and Astrophysics **498**, 915 (2009).

122. N. R. Badnell, *"Dielectronic Recombination of Fe $3p^q$ ions: A Key Ingredient for Describing X-Ray Absorption in Active Galactic Nuclei"*, Astrophysical Journal **651**, L73 (2006).

123. P. Mazzotta, G. Mazzitelli, S. Colafrancesco, and N. Vittorio, *"Ionization Balance for Optically Thin Plasmas: Rate Coefficients for All Atoms and Ions of the Elements H to Ni"*, Astronomy and Astrophysics Supplement Series **133**, 403 (1998).

124. E. Landi, P. J. Storey, and C. J. Zeippen, *"Atomic Data and Spectral Line Intensities for Ca VIII"*, The Astrophysical Journal **607**, 640 (2004).

125. W. Curdt, P. Brekke, U. Feldman, K. Wilhelm, B. N. Dwivedi, U. Schühle, and P. Lemaire, *"The SUMER Spectral Atlas of Solar-Disk Features"*, Astronomy and Astrophysics **375**, 591 (2001).

126. W. Curdt, E. Landi, and U. Feldman, *"The SUMER Spectral Atlas of Solar Coronal Features"*, Astronomy and Astrophysics **427**, 1045 (2004).

127. V. L. Jacobs, J. Davis, J. E. Rogerson, and M. Blaha, *"Dielectronic Recombination Rates, Ionization Equilibrium, and Radiative Energy-Loss Rates for Neon, Magnesium, and Sulfur Ions in Low-Density Plasmas"*, Astrophysical Journal **230**, 627 (1979).

128. N. R. Badnell, *"Dielectronic Recombination Rate Coefficients for S^{q+} ($q = 1 - 5$) Ions"*, Astrophysical Journal **379**, 356 (1991).

129. A. Al-Mulhem and I. Nasser, *"Dielectronic-Recombination Cross-Sections and Rate Coefficients for S^{3+}"*, Physical Review A **46**, 2945 (1992).

130. S. N. Nahar, *"Electron-Ion Recombination Rate Coefficients and Photoionization Cross Sections for Astrophysically Abundant Elements. III. Si-Sequence Ions: Si I, S III, Ar V, Ca VII, and Fe XIII"*, Astrophysical Journal Supplement Series **126**, 537 (2000).

131. R. F. Reilman and S. T. Manson, *"Photoabsorption Cross Sections for Positive Atomic Ions With $Z \leq 30$"*, The Astrophysical Journal Supplement Series **40**, 815 (1979).

132. A. M. Juett, N. S. Schulz, D. Chakrabarty, and T. W. Gorczyca, *"High-Resolution X-Ray Spectroscopy of the Interstellar Medium. II. Neon and Iron Absorption Edges"*, The Astrophysical Journal **648**, 1066 (2006).

133. T. W. Gorczyca, *"Auger Decay of the Photoexcited $1s^{-1} \to np$ Rydberg Series in Neon"*, Physical Review A **61**, 024702 (2000).

134. J. Garcia, C. Mendoza, M. A. Bautista, T. W. Gorczyca, T. R. Kallman, and P. Palmeri, *"K-Shell Photoabsorption of Oxygen Ions"*, The Astrophysical Journal Supplement Series **158**, 68 (2005).

135. T. W. Gorczyca and B. M. McLaughlin, *"Inner-Shell Photoexcited Resonances in Atomic Oxygen"*, Journal of Physics B: Atomic, Molecular and Optical Physics **33**, L859 (2000).

136. A. M. Juett, N. S. Schulz, and D. Chakrabarty, *"High-Resolution X-Ray Spectroscopy of the Interstellar Medium: Structure at the Oxygen Absorption Edge"*, The Astrophysical Journal **612**, 308 (2004).

137. M. F. Hasoglu, S. A. Abdel-Naby, T. W. Gorczyca, J. J. Drake, and B. M. McLaughlin, *"K-Shell Photoabsorption Studies of the Carbon Isonuclear Sequence"*, ArXiv 1003.3639 (2010).

138. T. W. Gorczyca and F. Robicheaux, *"Auger Decay of the Photoexcited $2p^{-1}n\ell$ Rydberg Series in Argon"*, Physical Review A **60**, 1216 (1999).

139. S. E. Canton-Rogan, A. A. Wills, T. W. Gorczyca, M. Wiedenhoeft, O. Nayandin, C.-N. Liu, and N. Berrah, *"Mirroring Doubly Excited Resonances in Argon"*, Physical Review Letters **85**, 3113 (2000).

140. M. C. Witthoeft, M. A. Bautista, C. Mendoza, T. R. Kallman, P. Palmeri, and P. Quinet, *"K-Shell Photoionization and Photoabsorption of Ne, Mg, Si, S, Ar, and Ca"*, The Astrophysical Journal Supplement Series **182**, 127 (2009).

141. W. Eissner, M. Jones, and H. Nussbaumer, *"Techniques for the Calculation of Atomic Structures and Radiative Data Including Relativistic Corrections"*, Computer Physics Communications **8**, 270 (1974).

142. E. P. Wigner, *"Resonance Reactions and Anomalous Scattering"*, Physical Review **70**, 15 (1946).

143. E. P. Wigner and L. Eisenbud, *"Higher Angular Momenta and Long Range Interaction in Resonance Reactions"*, Physical Review **72**, 29 (1947).

144. A. M. Lane and R. G. Thomas, *"R-Matrix Theory of Nuclear Reactions"*, Reviews of Modern Physics **30**, 257 (1958).

145. P. G. Burke and W. D. Robb, *"The R-Matrix Theory of Atomic Processes"*, in *Advances in Atomic and Molecular Physics*, edited by D. R. Bates and I. Estermann, volume 11, p. 143, Academic Press, New York, 1975.

146. P. G. Burke and K. A. Berrington, *Atomic and Molecular Processes: an R-Matrix Approach* (Institute of Physics, Bristol, 1993).

147. K. A. Berrington, W. B. Eissner, and P. H. Norrington, *"RMATRX1: Belfast Atomic R-Matrix Codes"*, Computer Physics Communications **92**, 290 (1995).

148. T. W. Gorczyca, F. Robicheaux, M. S. Pindzola, D. C. Griffin, and N. R. Badnell, *"Elimination of Electron-Ion Pseudoresonances Associated with Approximate Target Wave Functions"*, Physical Review A **52**, 3877 (1995).

149. E. Merzbacher, *Quantum Mechanics*, 3rd ed. (Wiley, New York, 1998).

150. W. R. Johnson, *Atomic Structure Theory: Lectures on Atomic Physics* (Springer, Berlin ; London, 2007).

151. A. Messiah, *Quantum Mechanics* (John Wiley, Amsterdam: North-Holland, 1965).

152. B. H. Bransden and C. J. Joachain, *The Physics of Atoms and Molecules*, 2nd ed. (Prentice Hall, New York, 2002).

153. G. B. Arfken and H.-J. Weber, *Mathematical Methods for Physicists*, 5th ed. (Academic Press, San Diego, 1995).

154. R. D. Cowan, *The Theory of Atomic Structure and Spectra* (Berkeley: University of California Press, 1981).

155. E. U. Condon and G. H. Shortley, *The Theory of Atomic Spectra* (Cambridge Univ. Press, Cambridge, 1959).

156. C. Froese Fischer, T. Brage, and P. Jönsson, *Computational Atomic Structure: an MCHF Approach* (Institute of Physics Publ., Bristol, UK, 1997).

157. R. Fletcher, *Practical Methods of Optimization*, 2nd ed. (Wiley, New York, 1987).

158. M. J. Seaton, *"The Hartree-Fock Equations for Continuous States with Applications to Electron Excitation of the Ground Configuration Terms of O I"*, Philosophical Transactions of the Royal Society of London **245**, 469 (1953).

159. C. Froese Fischer, *"General Hartree-Fock Program"*, Computer Physics Communications **43**, 355 (1987).

160. C. Froese Fischer, *"The MCHF Atomic-Structure Package"*, Computer Physics Communications **64**, 369 (1991).

161. D. R. Hartree, *"The Wave Mechanics of an Atom with a Non-Coulomb Central Field. Part I. Theory and Methods"*, Mathematical Proceedings of the Cambridge Philosophical Society **24**, 89 (1928).

162. V. Fock, *"Näherungsmethode zur Lösung des Quantenmechanischen Mehrkörperproblems"*, Zeitschrift für Physik A Hadrons and Nuclei **61**, 126 (1930).

163. V. Fock, *"Selfconsistent Field mit Austausch für Natrium"*, Zeitschrift für Physik A Hadrons and Nuclei **62**, 795 (1930).

164. J. C. Slater, *"Atomic Shielding Constants"*, Physical Review **36**, 57 (1930).

165. C. Zener, *"Analytic Atomic Wave Functions"*, Physical Review **36**, 51 (1930).

166. A. Burgess, H. E. Mason, and J. A. Tully, *"Coronal Mg^{+9}: Collisional Excitation of the $2s - 2p$ Multiplet"*, Astronomy and Astrophysics **217**, 319 (1989).

167. W. Eissner and M. J. Seaton, *"Computer Programs for the Calculation of Electron-Atom Collision Cross Sections. I. General Formulation"*, Journal of Physics B: Atomic Molecular Physics **5**, 2187 (1972).

168. A. Burgess and V. B. Sheorey, *"Electron Impact Excitation of the Resonance Lines of Alkali-Like Positive Ions"*, Journal of Physics B Atomic Molecular Physics **7**, 2403 (1974).

169. I. P. Grant, *Relativistic Quantum Theory of Atoms and Molecules: Theory and Computation* (Springer, New York, 2007).

170. I. I. Sobelman, *Atomic Spectra and Radiative Transitions*, 2nd ed. (Springer-Verlag, Berlin, 1992).

171. H. A. Bethe and E. E. Salpeter, *Quantum Mechanics of One- and Two-Electron Atoms* (Academic Press, New York, 1957).

172. M. S. Pindzola, N. R. Badnell, and D. C. Griffin, *"Validity of the Independent-Processes and Isolated-Resonance Approximations for Electron-Ion Recombination"*, Physical Review A **46**, 5725 (1992).

173. P. F. Dittner, S. Datz, P. D. Miller, P. L. Pepmiller, and C. M. Fou, *"Dielectronic Recombination Measurements of P^{4+}, S^{5+}, and Cl^{6+}"*, Physical Review A **33**, 124 (1986).

174. W. Zong, R. Schuch, H. Gao, D. R. DeWitt, and N. R. Badnell, *"Low-Energy Recombination of Ne^{7+}"*, Journal of Physics B: Atomic Molecular Physics **31**, 3729 (1998).

175. S. Schippers, A. Müller, G. Gwinner, J. Linkemann, A. A. Saghiri, and A. Wolf, *"Storage Ring Measurement of the C IV Recombination Rate Coefficient"*, The Astrophysical Journal **555**, 1027 (2001).

176. K. A. Berrington, P. G. Burke, J. J. Chang, A. T. Chivers, W. D. Robb, and K. T. Taylor, *"A General Program to Calculate Atomic Continuum Processes Using the R-Matrix Method"*, Computer Physics Communications **8**, 149 (1974).

177. P. G. Burke and K. Smith, *"The Low-Energy Scattering of Electrons and Positrons by Hydrogen Atoms"*, Reviews of Modern Physics **34**, 458 (1962).

178. P. G. Burke, *"The R-Matrix Method in Atomic Physics"*, Computer Physics Communications **6**, 288 (1973).

179. C. Bloch, *"Une formulation unifiée de la théorie des réactions nucléaires"*, Nuclear Physics **4**, 503 (1957).

180. A. F. Starace, *"Theory of Atomic Photoionization"*, in *Encyclopedia of Physics*, edited by W. Mehlhorn, volume 31, p. 1, Springer-Verlag, New York, 1982.

181. F. T. Smith, *"Lifetime Matrix in Collision Theory"*, Physical Review **118**, 349 (1960).

182. F. P. Keenan and S. M. Mccann, *"Ar-XVII Line Ratios in Tokamak Plasmas"*, Journal of Physics B: Atomic Molecular and Optical Physics **23**, L423 (1990).

183. J. Abdallah and R. E. H. Clark, *"Comparison of Explicit and Effective Models for Calculating Ionic Populations in Argon Plasmas"*, Journal of Physics B: Atomic Molecular and Optical Physics **27**, 3589 (1994).

184. M. S. Pindzola, D. C. Griffin, and C. Bottcher, in *Atomic Processes in Electron-Ion and Ion-Ion Collisions*, edited by F. Brouillard, p. 75, (Plenum; New York), 1986.

185. S. D. Loch, S. A. Abdel-Naby, C. P. Ballance, and M. S. Pindzola, *"Electron-Impact Ionization and Recombination of M-Shell Atomic Ions in the Argon Isonuclear Sequence"*, Physical Review A **76**, 022706 (2007).

186. N. R. Badnell, *"On the Effects of the Two-Body Non-Fine-Structure Operators of the Breit-Pauli Hamiltonian"*, Journal of Physics B: Atomic Molecular and Optical Physics **30**, 1 (1997).

187. M. J. Seaton, *"Radiative Recombination of Hydrogenic Ions"*, Monthly Notices of the Royal Astronomical Society **119**, 81 (1959).

188. D. T. Woods, J. M. Shull, and C. L. Sarazin, *"Recombination Coefficients for Iron Ions"*, Astrophysical Journal **249**, 399 (1981).

189. V. L. Jacobs, J. Davis, P. C. Kepple, and M. Blaha, *"Influence of Autoionization Accompanied by Excitation on Dielectronic Recombination and Ionization Equilibrium of Silicon Ions"*, Astrophysical Journal **215**, 690 (1977).

190. V. L. Jacobs, J. Davis, J. E. Rogerson, M. Blaha, J. Cain, and M. Davis, *"Dielectronic Recombination Rates, Ionization Equilibrium, and Radiative Emission Rates for Calcium and Nickel Ions in Low-Density High-Temperature Plasmas"*, Astrophysical Journal **239**, 1119 (1980).

191. V. L. Jacobs, J. Davis, P. C. Kepple, and M. Blaha, *"Influence of Autoionization Accompanied by Excitation on Dielectronic Recombination and Ionization Equilibrium"*, Astrophysical Journal **211**, 605 (1977).

192. G. Mazzitelli and M. Mattioli, *"Ionization Balance for Optically Thin Plasmas: Rate Coefficients for Cu, Zn, Ga, and Ge Ions"*, Atomic Data and Nuclear Data Tables **82**, 313 (2002).

193. D. A. Verner and G. J. Ferland, *"Atomic Data for Astrophysics. I. Radiative Recombination Rates for H-like, He-like, Li-like, and Na-like Ions over a Broad Range of Temperature"*, The Astrophysical Journal Supplement Series **103**, 467 (1996).

194. S. N. Nahar, *"Electron-Ion Recombination Rate Coefficients for Si I, Si II, S II, S III, C II, and C-Like Ions C I, N II, O III, F IV, Ne V, Na VI, Mg VII, Al VIII, Si IX, and S XI"*, Astrophysical Journal Supplement Series **101**, 423 (1995).

195. S. N. Nahar, *"Electron-Ion Recombination Rate Coefficients for Si I, Si II, S II, S III, C II, and C-Like Ions C I, N II, O III, F IV, Ne V, Na VI, Mg VII, Al VIII, Si IX, and S XI (Astrophysical Journal Supplement Series 101, 423, 1995)"*, Astrophysical Journal Supplement Series **106**, 213 (1996).

196. I. Joelsson, L. Engstrom, K. E. Magnusson, and P. O. Zetterberg, unpublished (1989).

197. W. C. Martin, R. Zalubas, and A. Musgrove, *"Energy Levels of Sulfur, S I Through S XVI"*, Journal of Physical and Chemical Reference Data **19**, 821 (1990).

149

198. C. Froese Fischer, G. Tachiev, and A. Irimia, *"Relativistic Energy Levels, Lifetimes, and Transition Probabilities for the Sodium-Like to Argon-Like Sequences"*, Atomic Data and Nuclear Data Tables **92**, 607 (2006).

199. A. K. Bhatia, G. A. Doschek, and U. Feldman, *"Atomic Data for S IV and Solar Observations of the $3s^2 3p\ ^2P - 3s3p^2\ ^4P$ Multiplet"*, Astronomy and Astrophysics **86**, 32 (1980).

200. S. S. Tayal, *"Oscillator Strengths of Electric Dipole Transitions in S^{3+}"*, Journal of Physics B: Atomic Molecular Physics **32**, 5311 (1999).

201. G. P. Gupta and A. Z. Msezane, *"Fine-Structure Calculation of Energy Levels, Oscillator Strengths, and Lifetimes in Al-Like Sulfur"*, Astrophysical Journal Supplement Series **130**, 227 (2000).

202. A. Hibbert, T. Brage, and J. Fleming, *"$3s^2 3p - 3s3p^2$ Transitions in SIV"*, Monthly Notices of the Royal Astronomical Society **333**, 885 (2002).

203. A. Hibbert, *"CIV3 - A General Program to Calculate Configuration Interaction Wave Functions and Electric-Dipole Oscillator Strengths"*, Computer Physics Communications **9**, 141 (1975).

204. P. Bryans, E. Landi, and D. W. Savin, *"A New Approach to Analyzing Solar Coronal Spectra and Updated Collisional Ionization Equilibrium Calculations. II. Updated Ionization Rate Coefficients"*, Astrophysical Journal **691**, 1540 (2009).

205. K. T. Korista, Private Communication, (2010).

206. D. E. Inglis and E. Teller, *"Ionic Depression of Series Limits in One-Electron Spectra"*, Astrophysical Journal **90**, 439 (1939).

207. S. A. Abdel-Naby, D. Nikolić, T. W. Gorczyca, N. R. Badnell, and D. W. Savin, *"M-Shell Dielectronic Recombination: Theoretical Study"*, in *American Institute of Physics Conference Series*, edited by F. D. McDaniel and B. L. Doyle, volume 1099, pp. 111–116, 2009.

208. H. Nussbaumer and P. J. Storey, *"Dielectronic Recombination at Low-Temperatures .3. Recombination Coefficients for Mg, Al, Si"*, Astronomy and Astrophysics Supplement Series **64**, 545 (1986).

209. J. A. Santana, Y. Ishikawa, and E. Trabert, *"Multireference Moller-Plesset Perturbation Theory Results on Levels and Transition Rates in Al-Like Ions of Iron Group Elements"*, Physica Scripta **79**, 065301 (2009).

210. S. A. Abdel-Naby, T. W. Gorczyca, K. T. Korista, and N. R. Badnell, *"Dielectronic Recombination Data for Dynamic Finite-Density Plasmas - XIV. The Aluminum Isoelectronic Sequence"*, Astronomy and Astrophysics , in preparation (2010).

211. F. B. S. Paerels and S. M. Kahn, *"High-Resolution X-Ray Spectroscopy with CHAN-DRA and XMM-NEWTON"*, Annual Review of Astronomy and Astrophysics **41**, 291 (2003).

212. M. A. Bautista, C. Mendoza, T. R. Kallman, and P. Palmeri, *"K-shell Photoionization and Electron Impact Excitation of Fe XVII-Fe XXIII"*, Astronomy and Astrophysics **418**, 1171 (2004).

213. T. R. Kallman, P. Palmeri, M. A. Bautista, C. Mendoza, and J. H. Krolik, *"Photoionization Modeling and the K Lines of Iron"*, The Astrophysical Journal Supplement Series **155**, 675 (2004).

214. D. A. Verner, D. G. Yakovlev, I. M. Band, and M. B. Trzhaskovskaya, *"Subshell Photoionization Cross Sections and Ionization Energies of Atoms and Ions from He to Zn"*, Atomic Data and Nuclear Data Tables **55**, 233 (1993).

215. P. Palmeri, P. Quinet, C. Mendoza, M. A. Bautista, J. Garcia, and T. R. Kallman, *"Radiative and Auger Decay of K-Vacancy Levels in the Ne, Mg, Si, S, Ar, and Ca Isonuclear Sequences"*, The Astrophysical Journal Supplement Series **177**, 408 (2008).

216. P. J. Mohr, B. N. Taylor, and D. B. Newell, *"CODATA Recommended Values of the Fundamental Physical Constants: 2006"*, Reviews of Modern Physics **80**, 633 (2008).

217. P. J. Mohr, B. N. Taylor, and D. B. Neweo, *"CODATA Recommended Values of the Fundamental Physical Constants: 2006"*, Journal of Physical and Chemical Reference Data **37**, 1187 (2008).